The impact of histone H4 lysine 16 acylations on chromatin dynamics and their links to acyl-CoA metabolism

Dissertation

zum Erwerb des Doktorgrades der Naturwissenschaften

an der Fakultät für Biologie der

Ludwig-Maximilians-Universität München

vorgelegt von

Sandra Nitsch

München, 11.10.2021

Diese Dissertation wurde am Helmholtz Zentrum München,
dem Deutschen Forschungszentrum für Gesundheit und Umwelt,
im Institut der funktionellen Epigenetik verfasst.

1. Gutachter:	Prof. Dr. Robert Schneider
2. Gutachter:	Prof. Dr. Thomas Nägele
Tag der Abgabe:	11.10.2021
Tag der mündlichen Prüfung:	16.02.2023

In order to enter into a state
where there is no desire and no suffering,
one must follow a certain path.
(Buddha)

EIDESSTATTLICHE ERKLÄRUNG

Ich versichere hiermit an Eides statt, dass die vorliegende Dissertation von mir selbstständig und ohne unerlaubte Hilfe angefertigt ist.

München, 07.03.2023

Ort, Datum Sandra Nitsch

ERKLÄRUNG

Hiermit erkläre ich, dass die Dissertation nicht ganz oder in wesentlichen Teilen einer anderen Prüfungskommission vorgelegt worden ist. Ich erkläre weiter, dass ich mich anderweitig einer Doktorprüfung ohne Erfolg nicht unterzogen habe.

München, 07.03.2023

Ort, Datum Sandra Nitsch

PUBLICATIONS

Published

Shahidian, LZ, Haas, M, Mourão, A, Geerlo, A, Le Gras, S, Nitsch, S, Margueron, R, Michaelis, J, Daujat, S and Schneider, R. Succinylation of H3K122 destabilizes the nucleosome and enhances transcription. EMBO Rep. 2021 Mar 3;22(3):e51009. doi: 10.15252/embr.202051009

Nitsch, S, Shahidian, LZ and Schneider, R. Histone acylations and chromatin dynamics: Concepts, challenges and links to metabolism. EMBO Rep 2021 Jun 23;22:e52774. doi: 10.15252/embr.202152774

In preparation

Nitsch, S, Schauer, T, Möritz, N, Funke, J, Nagpal, H, Jansen, P, Fulgencio-Covián, A, Mourão, A, Shahidian, LZ, Geerlo, A, Vermeulen, M, Straub, T, Dietz, H, Fierz, B, Desviat, LR and Schneider, R. Uncovering the role of H4K16 acylations on chromatin dynamics and during metabolic diseases.

SUMMARY

DNA can be wrapped around a histone octamer forming a nucleosome which is the smallest unit of chromatin. Chromatin is the storage form of genomic information in eukaryotic cells and its accessibility and function can be regulated by various post-translational modifications on histones. For example, acetylations on lysine residues in the histone tail or core regions are linked to open and accessible chromatin which allows active gene expression. In the last decade, multiple non-acetyl short-chain acylations on histone lysines deriving from corresponding metabolic intermediates (short-chain acyl-CoAs) were discovered. Histone acylations might therefore be able to integrate the metabolic state of a cell and fine-tune chromatin dynamics and gene expression. A detailed understanding of the interplay between metabolism and the epigenome remains elusive.

In this thesis, we first aimed to understand how histone acylations can regulate chromatin architecture. For our site of interest, we chose H4K16 due to its well-established role in higher-order chromatin formation. Via different *in vitro* studies we revealed how H4K16ac, H4K16pr, and H4K16bu can fine-tune internucleosomal interactions and nucleosomal stacking. Overall, all three acylations show a similar tendency but to a different degree which was further reflected in the stimulation efficiency of transcription *in vitro*. We were also able to identify the main H4K16 acetyltransferase MOF as a propionyl- and butyryltransferase *in cellulo* and further demonstrated acylation-specific binding of SIRT3. In addition, we observed how the nuclear distribution of H4K16 acylations is involved in stem cell fate decisions during hHSCs aging processes. Our studies on the genomic distribution of H4K16 acylations in mESCs revealed a specific enrichment of these modifications which might drive different gene expression programs. Our in *vivo* studies using mouse models for metabolic diseases demonstrated that histone acylations can actually reflect changes of metabolic intermediates. Alterations in the acyl-CoA levels can also influence the acylation/acetylation ratio suggesting that the combination of acylations rather than changes of a single acylation define their role in regulating chromatin dynamics. In addition, we further speculate that histone acylations can serve as a reservoir for short-chain fatty acids during aberrant metabolic fluctuations in order to protect the cell from toxic accumulations of metabolic intermediates.

ZUSAMMENFASSUNG

Bei der kleinsten Einheit von Chromatin handelt es sich um Nukleosome, die sich durch um ein Histon-Oktamer gewickelte DNA bilden. Die Funktion von Chromatin, das die Speicherform von genomischer Information in eukaryotischen Zellen ist, kann durch verschiedene post-translationale Modifikationen an Histonen reguliert werden. Beispielsweise ist die Acetylierung von Histon Lysinen mit offenem Chromatin verbunden, was eine aktive Genexpression ermöglicht. Im letzten Jahrzehnt wurden zusätzliche kurzkettige Acylierungen an Histon Lysinen entdeckt, die von entsprechenden metabolischen Zwischenprodukten (kurzkettigen Acyl-CoAs) stammen. Acylierungen von Histonen könnten daher den Stoffwechselzustand einer Zelle widerspiegeln und dadurch die Dynamik von Chromatin sowie die Genexpression anpassen. Ein detailliertes Verständnis der Interaktionen zwischen dem Stoffwechsel und dem Epigenom ist bisher ungeklärt.

In dieser Dissertation wollten wir zunächst verstehen, wie Acylierungen der Histone die Chromatinarchitektur regulieren können. Als Ausgangspunkt haben wir uns für H4K16 entschieden, da diese Position eine entscheidende Rolle bei der Bildung von Chromatin höherer Ordnung spielt. Durch verschiedene *in vitro* Studien konnten wir zeigen, wie H4K16ac, H4K16pr und H4K16bu internukleosomale Interaktionen und nukleosomale Stapelung mit ähnlicher Tendenz, aber in unterschiedlichem Maße bestimmen können, was sich auch in der Stimulation der *in vitro* Transkription widerspiegelt. Wir konnten die wichtigste H4K16 Acetyltransferase MOF als Propionyl- und Butyryltransferase *in cellulo* identifizieren und konnten SIRT3 als acylierungsspezifischen Bindungspartner nachweisen. Darüber hinaus beobachteten wir, wie die Lokalisierung von H4K16 Acylierungen im Nukleus an der Entscheidung über das Schicksal von Stammzellen während des Alterungsprozesses beteiligt ist. Unsere Untersuchungen zur genomischen Verteilung von H4K16 Acylierungen in mESCs zeigten eine spezifische Anreicherung der einzelnen Modifikationen, die verschiedene Genexpressionsprogramme antreiben könnten. Unsere *in vivo* Studien mit Mausmodellen für Stoffwechselerkrankungen zeigten, dass Histon Acylierungen tatsächlich Veränderungen von metabolischen Zwischenprodukten widerspiegeln können und unterschiedliche Acyl-CoA Konzentrationen auch das Acylierungs-/Acetylierungsverhältnis beeinflussen. Dies deutet daraufhin, dass nicht die Veränderung einer einzelnen Acylierung die Chromatindynamik reguliert, sondern Acylierungen in ihrer Summe agieren. Des Weiteren spekulieren wir, dass Histon Acylierungen bei abnormalen Stoffwechselschwankungen als Reservoir für kurzkettige Fettsäuren dienen können, um die Zelle vor toxischen Akkumulationen metabolischer Zwischenprodukte zu schützen.

TABLE OF CONTENTS

1. Introduction 3
1.1. Epigenetics and chromatin structure 3
1.1.1. The basic building blocks of chromatin 4
1.1.2. The classic: Histone acetylation 6
1.1.3. The newcomers: Histone non-acetyl acylations 8
1.2. Acylations and their effect on chromatin dynamics 10
1.2.1. Influencing transcription and chromatin dynamics 10
1.2.2. The special one: Histone H4 lysine 16 11
1.3. The link between acyl-CoA metabolism and the histone acylome 13
1.3.1. Acyl-CoA metabolism 13
1.3.2. Metabolic compartmentalization 14
1.3.3. Diet and metabolic disorders affect the epigenome 16
2. Aim of study 19
3. Results 20
3.1. H4K16 acylations and their role in chromatin compaction 20
3.1.1. The preparation of the building blocks: Octamers with acylated H4K16 20
3.1.2. H4K16 acylations affect internucleosomal interaction 22
3.1.3. H4K16 acylations affect nucleosomal stacking 24
3.2. Epigenetic players and H4K16 acylations 27
3.2.1. MOF can propionylate and butyrylate H4K16 *in cellulo* 27
3.2.2. Identification of H4K16 acylation-specific interactors 28
3.3. H4K16 acylations and transcriptional activity 30
3.3.1. Purification of assembled chromatin via a sucrose gradient 31
3.3.2. H4K16 acylations stimulate transcription *in vitro* 32
3.4. The nuclear and genomic distribution of H4K16 acylations 33
3.4.1. Purification of site-specific antibodies against acylated H4K16 33
3.4.2. Nuclear distribution of H4K16 acylations 34
3.4.3. Genome-wide mapping of acylated H4K16: Method establishment 37
3.4.4. H4K16 acylations correlate with gene expression in mESCs 40
3.5. Metabolic challenges and their effect on H4K16 acylations 43
3.5.1. Metabolomics: Acyl-CoA quantifications 43
3.5.2. Genomic distribution of histone acylations in livers from HFD mice 44
3.5.3. Metabolic disorders affect H4K16 acylations 48
4. Discussion 58
4.1. Generation of designer chromatin 58
4.2. H4K16 acylations can fine-tune chromatin dynamics 59
4.3. General acyltransferases and acylation-specific interactors 60
4.4. H4K16 acylations stimulate transcription to a different degree 61
4.5. Distinct nuclear localization of H4K16 acylations during aging 62
4.6. The genomic localization of H4K16 acylations 64
4.7. The effect of diet on H4K16 acylations 65
4.8. H4K16 acylations: A reservoir in metabolic disorders 66
4.9. Conclusion 68
5. Materials 69
5.1. Antibodies 69
5.2. Bacterial strains 69
5.3. Buffers, medium and solutions 70
5.4. Chemicals and reagents 77
5.5. Kits 80
5.6. Mammalian cell lines and tissues 81
5.7. Plasmids 81
5.8. Peptides 82
5.9. Primer 82
6. Methods 84
6.1. Molecular biology methods 84

6.1.1. Purification of nucleic acids by phenol-chloroform extraction 84
6.1.2. Agarose gel electrophoresis 84
6.1.3. Heat shock transformation of *E. coli* 84
6.1.4. Plasmid DNA purification from *E. coli* 84
6.1.5. Cesium chloride gradient centrifugation of plasmid DNA 85
6.1.6. RNA purification and reverse transcription from mammalian cells and tissue 85
6.1.8. RNA-seq from liver samples 86
6.1.9. RNA-seq analysis 86
6.2. Biochemical assays 87
6.2.1. SDS-PAGE electrophoresis 87
6.2.2. Western blot transfer 87
6.2.3. Immunoblotting 87
6.2.4. Protein extraction 88
6.2.5. Acidic histone extraction 88
6.2.6. Histone acylation quantification via MS 89
6.2.7. Expression of recombinant unmodified histones and truncated histone H4 89
6.2.8. Purification of recombinant unmodified histones 90
6.2.9. Purification of truncated histone H4 91
6.2.10. Ligation of truncated histone H4 and acylated peptide 92
6.2.11. Refolding of octamers 92
6.2.12. Nucleosome assembly 93
6.2.13. DNA-origami force spectrometer 93
6.2.14. Nucleosomal stacking assay 94
6.2.15. ACF purification 94
6.2.16. NAP1 purification 94
6.2.17. Chromatin assembly with NAP1 and ACF 95
6.2.18. MNase digestion of *in vitro* assembled chromatin 95
6.2.19. Sucrose gradient centrifugation of *in vitro* assembled chromatin 96
6.2.20. GAL4-VP16 purification 96
6.2.21. P300 purification 97
6.2.22. Nuclear extraction for affinity purification and IVT 97
6.2.23. *In vitro* transcription (IVT) assays 98
6.2.24. Coupling of H4 peptides to agarose beads 99
6.2.25. Peptide-based affinity purification 99
6.2.26. Antibody purification 100
6.2.27. Peptide immunoblotting 100
6.2.28. Immunofluorescence of MEFs 101
6.2.29. Immunofluorescence of hHSCs 101
6.2.30. Crosslinked (X-) ChIP 101
6.2.31. Crosslinked MNase (X-MNase) ChIP 102
6.2.32. CUT&RUN 103
6.2.33. Native (N-) ChIP for cells 104
6.2.34. Native (N-) ChIP for tissue 105
6.2.35. Library preparation for ChIP-seq 105
6.2.36. ChIP-seq analysis 106
6.2.37. Acyl-Coa measurements via MS 106
6.3. Animal experiments and cell culture methods 107
6.3.1. Cell culturing 107
6.3.2. Mice 108
7. Abbreviations 109
7.1. General abbreviations 109
7.2. Units abbreviations 112
8. Acknowledgments 113
9. References 114
10. Appendix 126

1. Introduction

1.1. Epigenetics and chromatin structure

The genomic DNA contains all the information for the thorough development and proper maintenance of an intact organism. Stunningly, in a multicellular organism each cell has the same genetic information and yet various cell types and functions exist which can only be achieved by an accurate activation or inhibition of specific gene expression programs (Gurdon, 1962; Monod & Jacob, 1961). Already in 1942, Conrad H. Waddington realized that such a regulation of gene expression might not be encoded in the genetic information and introduced "a new branch of biology" which he called epigenetics. This term starts with the Greek prefix "epi" and means "on top of" or "above" which already indicates Waddington's idea. He described epigenetics as "causal interactions between genes and their products, which bring the phenotype into being" (Waddington, 1942).

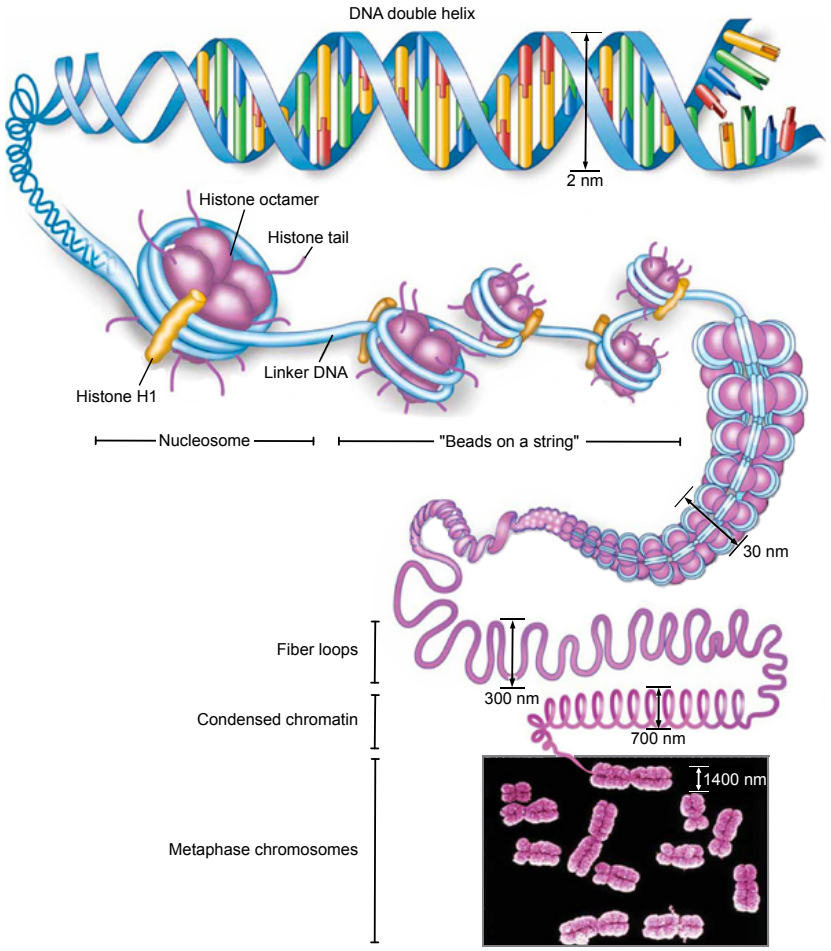

Figure 1.1: Hierarchical chromatin structures. DNA is wrapped around histone octamers to build the nucleosome. Linker histone H1 can bind to linker DNA. The "beads on the string" (also called 10 nm fiber) can be further packed into a 30 nm fiber. Supercoiling of such fibers leads to loop formation (300 nm) that can further result in the condensation of chromatin sections. The maximal compaction occurs during mitosis in metaphase chromosomes (modified from Sadava, 2014).

Although different definitions of epigenetics co-exist nowadays, the following is widely accepted: Epigenetics is ‘‘the study of changes in gene function that are mitotically and/or meiotically heritable and that do not entail a change in DNA sequence” (Wu & Morris, 2001; Deans & Maggert, 2015). Such regulation of gene function can be achieved by epigenetic mechanisms that include post-translational modifications (PTM) on histones, DNA methylation, and non-coding RNAs (ncRNAs) (Gibney & Nolan, 2010). But how can these epigenetic mechanisms affect gene function? This can be largely explained by the way genomic information is stored in the nucleus. In eukaryotic cells, the storage form of genomic information is called chromatin and consists mainly of DNA and proteins (Fig. 1.1). Chromatin structure exists in different organizational compaction levels and the highest level of chromatin compaction occurs during mitosis in the formation of metaphase chromosomes. Such chromosomes are composed of chromosome sections that are 700 nm in diameter and these sections result from the compaction of fiber loops (diameter: 300 nm) (Mikhail, 2019). A structural level below fiber loops is the controversial 30 nm fiber which was observed *in vitro* but its existence *in vivo* still remains uncertain (Xu *et al*, 2021). The fundamental organization level of chromatin is the linear 10 nm fiber that can be also described as “beads on a string” in which the repeating beads are actually the smallest units of chromatin: the nucleosomes (Olins & Olins, 2003; Mikhail, 2019).

1.1.1. The basic building blocks of chromatin

Nucleosomes consist of a histone octamer containing one histone H3/H4 tetramer and two histone H2A/H2B dimers around which 147 base pairs (bp) of DNA are wrapped. Core histones H2A, H2B, H3, and H4 are small (10-15 kDA), evolutionary conserved, and positively charged proteins. Their positive charge results from a high composition of lysine and arginine (basic) residues that naturally attract negatively charged DNA (McGhee & Felsenfeld, 1980). Core histones consist of an N-terminal histone tail (H2A: 16 aa, H2B: 32 aa, H3: 44 aa, H4: 26 aa) and a globular fold domain (~80 aa) except for H2A which has an additional C-terminal tail (15 aa). These flexible tails are protruding from the nucleosomal core as unstructured domains that can interact with neighboring nucleosomes or other chromatin components (Luger et al, 1997). In addition to the core histones, the linker histone variants of H1 (~ 23 kDA) consist of an N-terminal tail (~40 aa), a long C-terminal tail (~100 aa), and a globular domain (~70 aa). As shown in Fig. 1.2, H1 binding can occur close to the DNA entry/ exit site at the surface of nucleosomes where it can interact with the linker DNA between neighboring nucleosomes, potentially stabilizing nucleosomal stacking (Izzo *et al*, 2008). The H4 tail as well as multiple

other nucleosome binding proteins can directly interact with the so-called acidic patch region of neighboring nucleosomes and can affect nucleosomal stacking and therefore higher-order chromatin structures (Kalashnikova *et al*, 2013). This acidic patch is formed by negatively charged amino acids from H2A and H2B on the surface of nucleosomes (Fig. 1.2). What is also an important site in regard of nucleosomal stacking is the so-called H2A/ H2B four-helix bundle that is created within tetranucleosomes. Post-translational modifications of H2A and H2B in these regions are known to interfere with nucleosomal stacking and therefore are linked to open chromatin structures (Fierz & Poirier, 2019).

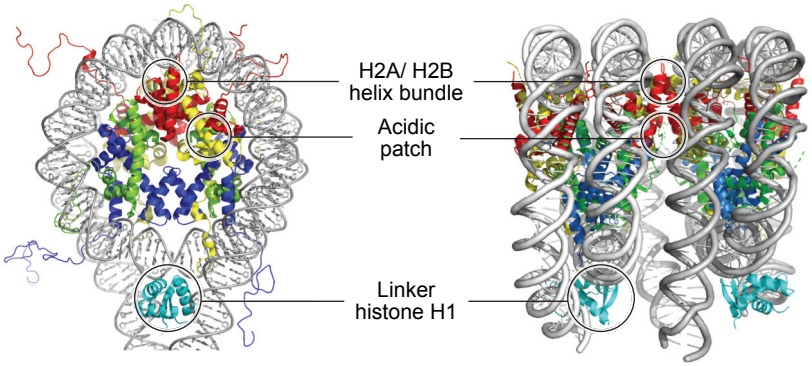

Figure 1.2: Nucleosome structure. Nucleosome crystal structure with histones H2A (yellow), H2B (red), H3 (blue), H4 (green), and the DNA (gray) and an interacting linker histone H1 (light blue). The acidic patch and the H2A/H2B helix bundle are involved in nucleosomal stacking. (Fierz & Poirier, 2019)

In general, PTMs are reversible and occur on linker and core histones in their tail and globular domains. Prominent PTMs are for example acetylation on lysines (Kuo & Allis, 1998), methylation on lysines and arginines (Kouzarides, 2002), phosphorylation on serines and threonines (Oki et al, 2007) or ubiquitinylation on lysines (Zhang, 2003) that can directly affect chromatin function by influencing the DNA-histone, histone-histone and internucleosomal interactions as well as the nucleosome stability itself. The existence of various combinations of histone PTMs evoked the idea of a so-called histone code that could define chromatin fate and function (Strahl & Allis, 2000). The specific recruitment of interactors (so-called readers) could be due to their binding to distinct patterns of PTMs and could modulate chromatin dynamics and function in a highly coordinated manner. Readers can contain multiple recognition domains and can also act in combinations with other readers which supports the histone code idea (Rothbart *et al*, 2013). An overview of reader domains is given in Table 1.1.

Table 1.1: Overview for reader domains

Modification	**Examples**
Lysine acetylation	Bromodomain
Lysine methylation	Chromodomain Tudor domain Plant homeodomain (PHD) PWWP domain Malignant Brain Tumor (MBT) domain
Arginine methylation	Tudor domain
Serine phosphorylation	14-3-3 domain BRCA1 carboxy-terminal (BRCT) domains
Unmodified histone	ATRX-DNMT3-DNMT3L (ADD) domain PHD domain

Translating such a "histone language" was thought to be the breakthrough in order to understand how certain histone PTMs determine for example gene transcription or silencing (Jenuwein & Allis, 2001). However, the combinatorial complexity, a dynamic turnover of certain modifications as well as the identification of novel histone PTMs made it difficult to actually identify or even unravel such a potential code whose existence, therefore, remains controversial (Rando, 2012). Independently of such a potential histone code the described complexity of histone modifications highlights their potential to fine-tune chromatin dynamics and therefore function. Since all of the modifications have their own chemical properties, they can influence the DNA accessibility to different degrees. Depending on the packaging of chromatin, the structure can be rather open and accessible (so-called euchromatin) or closed and compact as in heterochromatic regions. How accessible specific gene regions are e.g. for the recruitment of the transcriptional machinery can also define their gene expression activity. Hallmarks for heterochromatin are for example DNA methylation as well as H3K9me3, H3K27me3, while H4K8ac and H3K9ac can mark euchromatic regions (Allis & Jenuwein, 2016).

1.1.2. The classic: Histone acetylation

Histone acetylations can occur on the ε-amino group of lysines in the globular and tail region of all core histones (in total 54 sites) and neutralize the positive charge of lysines. This charge reduction on histones can weaken the overall interaction between the octamers and the DNA. Upon lysine acetylation (Kac), chromatin tends to open up and since the DNA gets more accessible this allows efficient recruitment for example of the transcription machinery followed

by transcription initiation (Bannister & Kouzarides, 2011). Different studies have already shown that the enrichment of various histone acetylations like H3K9ac, H3K14ac or H4K12ac at transcriptional start sites (TSS) correlates with active gene expression (Karmodiya *et al*, 2012; Paradowska *et al*, 2012). Abnormal histone acetylation was observed for example in cancer and metabolic diseases such as diabetes which emphasizes the essential role of Kac on cellular functions (Timmermann *et al*, 2001; Zhong & Kowluru, 2010).

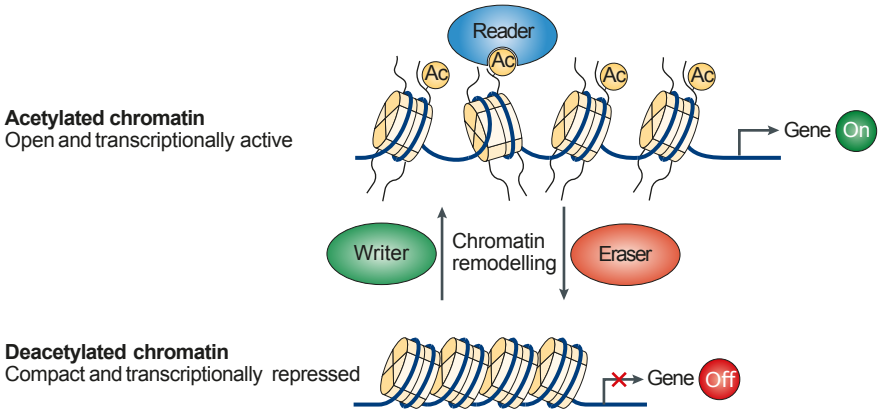

Figure 1.3: Histone acetylation regulates gene expression via chromatin compaction**.** Lysine acetylation (Kac) on the histone tails can be placed via writers (histone acetyltransferases, HATs) and induce an open chromatin state to which various readers like transcription factors can bind and initiate gene expression. Removal of Kac via erasers (histone deacetylases, HDACs) leads to chromatin compaction and further gene silencing (Verdin & Ott, 2014).

Histone PTMs are placed via so-called writers and in the case of Kac these writers are called histone acetyltransferases (HATs) that use acetyl-CoA as their co-factor to modify lysines. Most HATs can acetylate various lysines in histones as well as non-histone proteins and only a few are actually site-specific (Glozak *et al*, 2005). In addition, HAT specificity can be influenced by their incorporation into various complexes consisting of different interactors (Hodawadekar & Marmorstein, 2007). HATs can be classified into type A and type B HATs. Type A HATs are mainly nuclear and can be divided into three main groups due to their sequence homology. The largest family is the MYST (MOZ, YBF2/SAS3, SAS2 and TIP60) family. Prominent HATs like KAT2A (GCN5) and KAT2B (PCAF) belong to the GNAT (GCN5-related N-acetyltransferase) family. The third family is the p300/CBP (KAT3B/KAT3A) family or the so-called orphan family (Roth *et al*, 2001). Type B HATs are predominately cytoplasmic and acetylate-free histones directly after their synthesis. Acetylation of these histones leads to their transport into the nucleus where they can be used for chromatin synthesis (Parthun, 2007).

So-called erasers which can remove Kac and thereby restore the positive lysine charge are histone deacetylases (HDACs). In general, HDACs can deacetylate various acetylated lysines on histones and non-histone proteins. Deacetylation can unblock lysines for alternative lysine PTMs like methylation which can influence chromatin structure differently or recruit distinct interactors (Haberland *et al*, 2009). HDACs can be categorized into four different classes (I, II, III, and IV) based on the sequence homology to their corresponding in *S. cerevisiae*. HDAC class I (HDAC 1-3 and 8) and II (HDAC 4-7, 9, and 10) are evolutionarily related. While HDAC class I members only locate in the nucleus, HDAC class II members can also be found in the cytoplasm. HDAC class IV has only one member namely HDAC11 (Seto & Yoshida, 2014; Park & Kim, 2020). Members of the HDAC classes I, II, and IV are zinc-dependent enzymes, and their activity results in the generation of acetate, while members of HDAC class III (SIRT1-7, sirtuin1-7) are dependent on the co-factor nicotinamide adenine dinucleotide (NAD^+) and generate the metabolite O-acetyl-ADP-ribose (OAADPr) after lysine deacetylation. Sirtuins can also be found in the nucleus as well as in the cytoplasm (Vaquero, 2009; Martinez-Redondo & Vaquero, 2013).

While HATs and HDACs are involved in the direct impact of Kac on chromatin structure by adding or removing the modification, the recruitment of readers adds another way how Kac can shape chromatin function (Yun *et al*, 2011). Acetylation of lysines can influence the recruitment of certain readers. For example, YEATS domain (Yaf9, ENL, AF9, Taf14, and Sas5) containing proteins were shown to bind to Kac (Zhao *et al*, 2017). Both AF9 (human) and Taf14 (yeast) can interact with H3K9ac (Li *et al*, 2014; Shanle *et al*, 2015). In addition, well-known acetylation interactors are bromodomain (BD) containing proteins that can further recruit transcription factors or chromatin remodelers and define chromatin fate (Filippakopoulos & Knapp, 2012). Examples for BD-containing proteins are HATs and chromatin remodelers including SMARC2 (BRM) and SMARC4 (BRG1) (Singh *et al*, 2007; Morrison *et al*; 2017). In addition, transcriptional co-activators like BRD2 and TFIID as a subunit of the transcription initiation complex also contain bromodomains highlighting again the involvement of histone acetylation in the onset of transcription (Filippakopoulos *et al*, 2012).

1.1.3. The newcomers: Histone non-acetyl acylations

In the last decade with the advance of highly sensitive mass spectrometers (MS) novel histone non-acetyl acylations were identified on lysines and an overview of recently identified lysine acylations is provided in Fig. 1.4 (Barnes *et al*, 2019).

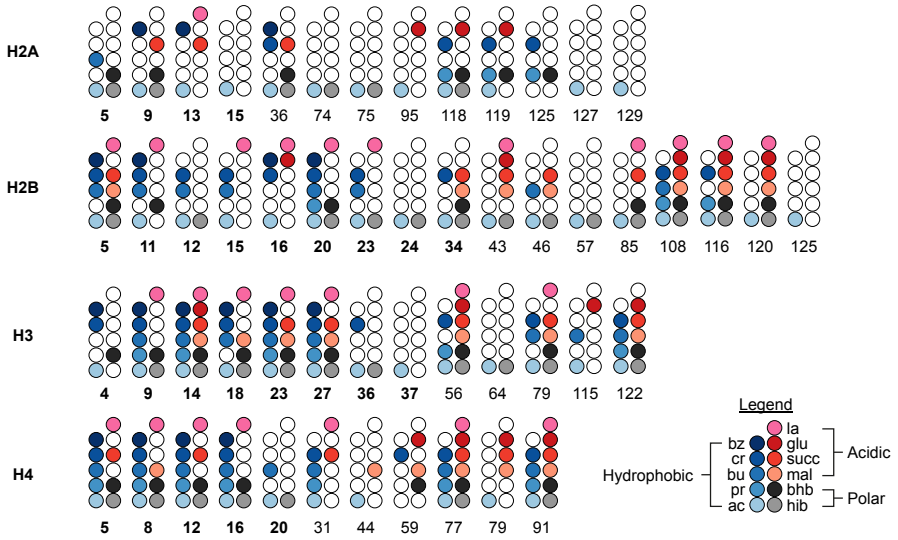

Figure 1.4: Lysine acylations on core histones. Shown are potential lysine acylation on all four core histones. Highlighted in bold are lysines in the N-terminal histone tail. Included acylations: ac: acetylation, pr: propionylation, bu: butyrylation, cr: crotonylation, bz: benzoylation, hib: 2-hydroxyisobutyrylation, bhb: β-hydroxybutyrylation, la: lactylation, mal: malonylation, succ: succinylation, glu: glutarylation. The chemical nature of acylations is shown in the legend (hydrophobic: blue, polar: gray, acidic: red) (Nitsch *et al*, 2021).

Lysine acylations fall into different classes due to their chemical properties. Lysine succinylation (Ksucc, Xie *et al*, 2012), malonylation (Kmal, Xie *et al*, 2012) and glutarylation (Kglu, Bao *et al*, 2019) are acidic modifications that revert the lysine charge from positive to negative. Polar modifications like 2-hydroxyisobutyrylation (Khib, Dai *et al*, 2014) and β-hydroxybutyrylation (Kbhb, Xie *et al*, 2016) contain hydroxyl groups that might recruit different interactors due to the ability to form hydrogen bonds. The group of hydrophobic acylations includes the linear 3-carbon long propionylation (Kpr, Chen *et al*, 2007), the linear 4-carbon long butyrylation (Kbu, Chen *et al*, 2007), the planar 4-carbon long crotonylation (Kcr, Tan *et al*, 2011) and the aromatic acyl group containing benzoylation (Kbz, Huang *et al*, 2018). As already mentioned Kac itself is a hydrophobic modification. In comparison to Kac, the other modifications in this hydrophobic group consist of a longer acyl chain and are therefore more hydrophobic and sterically hindering (Fig. 1.5). Most similar to Kac is Kpr (Sabari *et al*, 2017).

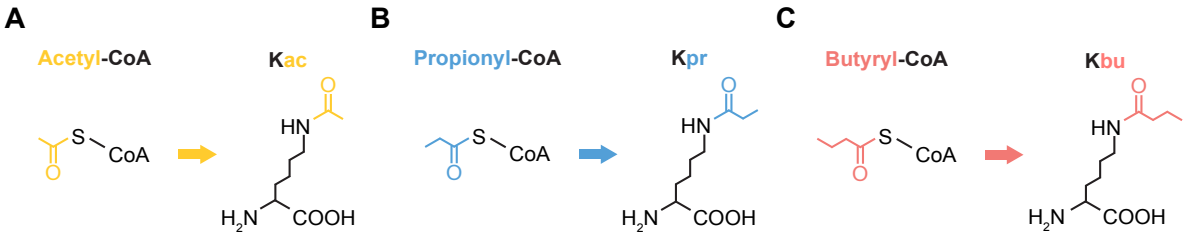

Figure 1.5: Hydrophobic lysine acylations. Chemical structure of acetyl-CoA (**A**), propionyl-CoA (**B**) and butyryl-CoA (**C**) and corresponding acylations on lysines (Kac: acetylation, (**A**); Kpr: propionylation (**B**); Kbu: butyrylation (**C**)) (modified from Trefely *et al*, 2020).

Like Kac, Kpr at H3 has also been correlated to active gene expression and seems to locate around TSSs *in cellulo* (Kebede *et al*, 2017). So far only canonical HATs like p300/CPB (Kaczmarska *et al*, 2017), P/CAF (Leemhuis *et al*, 2008), GCN5 (Ringel & Wolberger, 2016) and MOF (Han *et al*, 2018) have been identified to possess histone propionyltransferase activity. No propionylation-specific deacylase has been identified so far. HDACs like SIRT1-3 have been shown to depropionylate histone lysines *in vitro* (Smith &D Denu, 2007). Further, no interactors binding solely Kpr were identified. Only Kac readers like the (P)BAF chromatin remodeling complex were observed as Kpr binders as well (Vollmuth & Geyer, 2010; Kebede *et al*, 2017). Another hydrophobic acylation is the linear C4 modification: Kbu which is also linked to active gene expression (Goudarzi *et al*, 2016). BRD9 and CECR2 were shown to bind to Kbu *in vitro* (Flynn *et al*, 2015) as well as BPTF (Chen *et al*, 2020). Moreover, histone butyrylation can again be placed by canonical HATs like PCAF, GCN5, CBP, p300, NatA, Tip60, and MOF *in vitro* (Simithy *et al*, 2017). However, HATs seem to prefer acetyl-CoA as well as propionyl-CoA over butyryl-CoA as co-factors since the longer acyl chain potentially limits HAT activity. In line with this, butyryl-CoA seems to inhibit GCN5 and PCAF by blocking the active site (Ringel & Wolberger, 2016; Carrer *et al*, 2017). How acylation might fine-tune the recruitment of interactors is highlighted by canonical HDACs. While SIRT2 and SIRT6 were shown to prefer Kbu over Kac, SIRT1, and SIRT3 preferred Kac over Kbu *in vitro* (Smith & Denu, 2007; Tanabe *et al*, 2018).

1.2. Acylations and their effect on chromatin dynamics

1.2.1. Influencing transcription and chromatin dynamics

How do all the described non-acetyl acylations on histones affect chromatin dynamics and how different are their functions in comparison to acetylation? A possible functional difference may be their ability to stimulate transcription. Via *in vitro* transcription assays the effect of differently acylated nucleosomal arrays was studied. General Khib (Huang *et al*, 2018) and Kla

(Zhang *et al*, 2019) were revealed to impair transcription strength in comparison to Kac, while Kcr seemed to enhance transcription compared to Kac (Sabari *et al*, 2015). General histone Kbu was also shown to stimulate transcription to at least a similar degree to Kac (Goudarzi *et al*, 2016). H3K14pr was also shown to stimulate transcription (Kebede *et al* 2017). H3K122ac as well as H3K122succ were also able to stimulate transcription *in vitro* (Tropberger *et al*, 2013; Zorro Shahidian *et al*, 2021). Also via chromatin immunoprecipitation followed by next-generation sequencing (ChIP-seq), non-acetyl acetylations seemed to co-locate with corresponding acetylations at active genomic loci *in cellulo* and *in vivo* and correlated with gene expression (Xie *et al*, 2016; Smestad *et al*, 2018; Jo *et al*, 2020).

One underlying explanation for the effect of histone acylations on transcription is the way they affect chromatin dynamics. Kac as well as Kpr, Kbu, Kmal, and Ksucc can decrease nucleosome stability and histone-DNA interactions. Interestingly, the modification Ksucc had the strongest effect potentially since it features a long acyl-CoA chain and is an acidic modification (Smestad *et al*, 2020). Recent studies further explored in more detail the influence of acylations on the globular domain of core histones. H4K91glu was shown to initiate H2A/H2B dimer dissociation from nucleosomes and thereby decrease nucleosomal stability (Bao *et al*, 2019). Also, H4K77succ and H3K122succ seem to be involved in nucleosome destabilization (Jing *et al*, 2020; Zorro Shahidian *et al*, 2021). Observations like these highlight how different acylations might be able to fine-tune the chromatin environment.

1.2.2. The special one: Histone H4 lysine 16

Of particular importance for chromatin structure is the H4 tail which has five lysine residues: H4K5, 8, 12, 16, and 20. H4K16 acetylation is the most abundant H4 acetylation that occurs on ~60 % of H4 proteins in mammalian cells (Turner *et al*, 1989) and is linked to active gene expression in mESCs (Taylor *et al*, 2013). The unique role of the H4 tail on chromatin structure is highlighted in Fig. 1.6A: The basic H4 tail is able to reach out and interact with the acidic patch created from an H2A/H2B dimer in a neighboring nucleosome. Positions 14 to 19 of the H4 were first linked to chromatin compaction (Dorigo *et al*, 2003) but the main role was soon attributed to H4K16 alone. The interaction with the acidic patch is disrupted upon acetylation of H4K16 which leads to more spacing between neighboring nucleosomes (Chen *et al*, 2017). *In vitro*, Shogren-Knaak and colleagues (2006) were the first to demonstrate that H4K16ac prevents compaction of nucleosomal arrays and therefore might interfere with higher-order chromatin structure. Further, H4K16ac was shown to decrease internucleosomal interactions and to interfere with nucleosomal stacking *in vitro* (Funke *et al*,2016; Kilic *et al*, 2018).

Remarkably, these phenomena are not purely based on the charge reduction of lysine 16 upon acetylation but also on a changed flexibility of the H4 tail. As indicated in Fig. 1.6B the potential spatial distribution of the H4 tail is drastically reduced upon K16 acetylation due to a decreased tail flexibility which also limits its reach towards neighboring nucleosomes or potential interactors (Collepardo-Guevara *et al*, 2015).

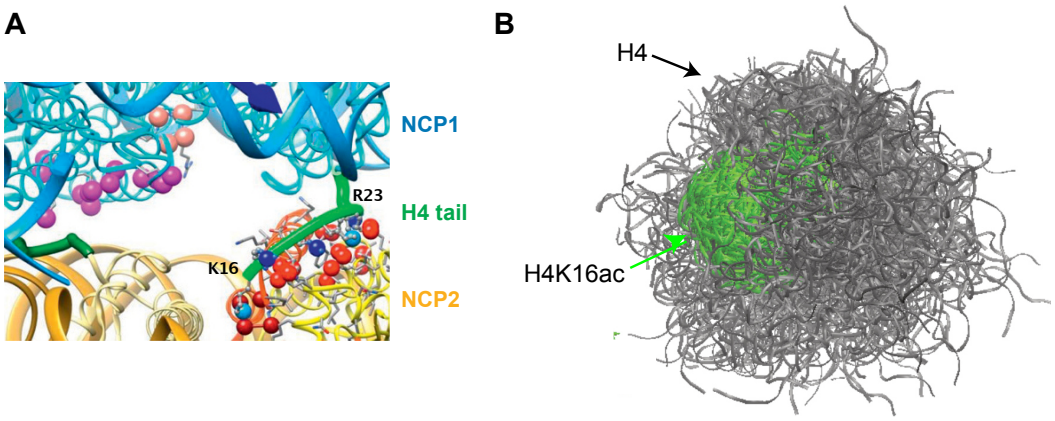

Figure 1.6: The unique role of H4K16ac in chromatin dynamics. A Stacking of nucleosomes reveals that the H4 tail of nucleosome core particle (NCP) 1 (shown in light green) interacts with the acidic patch of NCP2. The acidic patch is generated by Glu and Asp residues of H2A/H2B and corresponding oxygen atoms are shown as red spheres. The H4 tail of NCP2 is shown in darker green. Oxygen atoms from Glu and Asp are shown in purple (modified from Chen *et al*, 2017). **B** Comparison of the spatial distribution of an unmodified H4 tail (grey) and H4K16ac tail (green) during an 1 µs-long molecular dynamics simulation. The last amino acid of all frames were aligned together (Collepardo-Guevara *et al*, 2015).

Enzymes catalyzing H4K16ac are MOZ, Tip60, Hat1, and MOF (males absent on the first). But only in the absence of MOF, H4K16ac levels are majorly reduced, highlighting the fact that MOF (also called KAT8 or MYST1) is the predominant H4K16 acetyltransferase. Recently, it was shown that MOF can also act as a histone propionyltransferase *in cellulo* (Han *et al*, 2018) and a butyryltransferase *in vitro* (Simithy *et al*, 2017). MOF is a member of the HAT MYST family and is involved for example in the maintenance of chromatin structure (Thomas *et al*, 2008), DNA damage response (Sharma *et al*, 2010) and cell cycle progression (Taipale *et al*, 2005). MOF was initially studied during X chromosome dosage compensation in *Drosophila melanogaster* where it was shown to be a member of the MSL (male-specific lethal) complex. The MSL complex ensures doubled gene expression from a single male X chromosome via hyperacetylation and therefore mutations in MOF are lethal for male flies (Hilfiker *et al*, 1997). In addition, MOF can also be part of the NSL (non-specific lethal) complex and disruption of components of the NSL complex are lethal in both Drosophila sexes (Mendjan *et al*, 2006). In mammals, loss of MOF results in early embryonic lethality in female and male mice due to severe chromatin structure alterations (Thomas *et al*, 2008). Recently, Radzisheuskaya and

colleagues revealed that in mammals, MSL associated MOF is responsible for H4K16ac while as part of the NSL complex places H4K5ac and H4K8ac at promoter regions of genes essential for cell proliferation (Radzisheuskaya *et al*, 2021).

Erasers of H4K16ac include members of the HDAC family class III: SIRT1, SIRT2, and SIRT3. SIRT1 highly prefers H4K16ac as a substrate in comparison to its other potential targets like H3K9ac, H3K14ac, or H3K56ac (Vaquero *et al*, 2007). Cytoplasmic SIRT2 seems to translocate to the nucleus during the G2/M transition phase of the cell cycle and then deacetylates H4K16ac (Vaquero *et al*, 2006). The precise role and localization of SIRT3 remain ambiguous (Lombard & Zwaans, 2014). Intriguingly, SIRT3 exists in two different isoforms and it was shown that both isoforms can be found in the mitochondria as well as in the nucleus. In the mitochondria cleavage of the long isoform (removal of N-terminus) leads to the generation of the active SIRT3 isoform (Hirschey *et al*, 2011). In contrast, in the nucleus only the unprocessed SIRT3 was able to repress transcription (Scher *et al*, 2007). It was further shown that SIRT3 can actually bind to genes responsible for the expression of stress-related proteins as well as mitochondrial proteins (Iwahara *et al*, 2012). Nuclear SIRT3 was further able to deacetylate H4K16 as well as H3K9 and H3K56. In addition, SIRT3 can act as a de-β-hydroxybutyrylase and de-butyrylase targeting H4K16 but not H4K5/8/12 *in vitro* and *in cellulo* (Zhang *et al*, 2019). While canonical HATs and HDACs were shown to be active against various acylations, so far no study focused specifically on H4K16 acylations and their role in chromatin dynamics.

1.3. The link between acyl-CoA metabolism and the histone acylome

1.3.1. Acyl-CoA metabolism

Metabolism refers to the complex set of biochemical processes that occur within living organisms to maintain life, including for example the conversion of food into energy and the synthesis of new molecules necessary for cellular function. Metabolic pathways can be impacted by a variety of factors such as environmental conditions, dietary habits, physical exercise, and gut microbiota. Depending on the external stimuli, various metabolites are generated through different metabolic pathways defining the so-called metabolic state of a cell. Furthermore, metabolites can act as precursors for protein modifications which can shape their function and activity and thereby help cells to adjust or define cellular fate decisions (Wellen & Thompson, 2012). One main metabolic intermediate is acetyl-CoA which is involved in various cellular processes (Shi & Tu, 2015). Acetyl-CoA is mainly generated in mitochondria via glycolysis, the catabolism of branched amino acids or β-oxidation, and can be used to fuel

pyruvate into the tricarboxylic acid (TCA) cycle for the production of energy in form of ATP (Pietrocola *et al*, 2015). Acetyl-CoA can be transferred to the cytosol in form of citrate which is generated in the first step of the TCA cycle. Upon transfer via the mitochondrial citrate carrier into the cytosol, citrate can be cleaved by the ATP-citrate lyase (ACLY) regenerating acetyl-CoA (Chypre *et al*, 2012). Acetyl-CoA can also be exported to the cytoplasm in form of acetyl-L-carnitine via the carnitine shuttle. Recovery of acetyl-CoA in the cytoplasm is then achieved by a cytoplasmic carnitine O-acetyltransferase (CRAT) variant. In addition, acetyl-CoA can be produced in the cytosol from acetate via acyl-CoA synthetase short-chain family member 2 (ACSS2). In the cytoplasm, acetyl-CoA is involved in various anabolic reactions e.g. synthesis of fatty acids (Pietrocola *et al*, 2015). Acetyl-CoA is just one of the several acyl-CoAs that all consist of an acyl group that is linked to coenzyme A via a thioester bond. Propionyl-CoA is one acyl-chain longer than acetyl-CoA and can be generated by the oxidation of methionine, threonine, isoleucine, and valine (branched-chain amino acids) in peroxisomes and can get further processed to propionylcarnitine or propionate (Crown *et al*, 2015; Wanders *et al*, 2016). Propionyl-CoA can be also generated from the oxidation of the side chain of cholesterol or of odd-chain fatty acids in mitochondria and enters the TCA cycle after its conversion into succinyl-CoA. Propionyl-CoA might get transported into the cytosol via the carnitine shuttle similar to acetyl-CoA (Reszko *et al*, 2003; Violante *et al*, 2013). Propionate derived from the gut microbiota can also lead to propionyl-CoA generation via the acyl-CoA synthetase short-chain family member 3 (ACSS3) (Reichardt *et al*, 2014; Yoshimura *et al*, 2016). Another example from the acyl-CoA family is butyryl-CoA, a linear C4 molecule, that can also be generated in the mitochondria via fatty acid β-oxidation. Again the transport to the cytoplasm might be facilitated by the carnitine shuttle (Violante *et al*, 2013). Butyryl-CoA can be converted into butyrate which can act as an HDAC inhibitor. Butyrate itself also derives from the gut microbiota and can get imported into the mitochondria. Once in the mitochondria butyrate is oxidized and can then enter the TCA cycle (Venegas *et al*, 2019). Alternatively, butyrate also contributes to the cytosolic butyryl-CoA pool (Han *et al*, 2016).

1.3.2. Metabolic compartmentalization

The existence of an intimate link between metabolism and epigenetics is unquestionable since metabolites like the different acyl-CoAs are required as co-factors for histone modifiers (Sabari *et al*, 2017; Barnes *et al*, 2019; Boon *et al*, 2020; Dai *et al,* 2020; Haws *et al*, 2020; Trefely *et al*, 2020). Also, metabolites like NAD^+, propionate, or butyrate are known to inhibit the activity of erasers, again directly influencing for example the epigenetic control of gene expression.

Acetyl-CoA fluctuations can be directly reflected on histone Kac levels since the dissociation constant (Kd) of HATs is in a low micromolar or high nanomolar range while the actual cellular acetyl-CoA concentration is much higher (3–30 µM). The enzymatic activity of HATs is therefore highly sensitive towards nuclear acetyl-CoA fluctuations and that is why histone Kac levels are prone to reflect these changes (Gao *et al*, 2018; Nieborak & Schneider, 2018).

Even though metabolites like acetyl-, propionyl- or butyryl-CoA can freely diffuse from the cytoplasm into the nucleus (Sivanand *et al*, 2018), the composition of the cytosolic and nuclear acyl-CoA pools apparently seem to be different, and specifically, propionyl-CoA appeared to be enriched in the nucleus (Trefely *et al*, 2020).

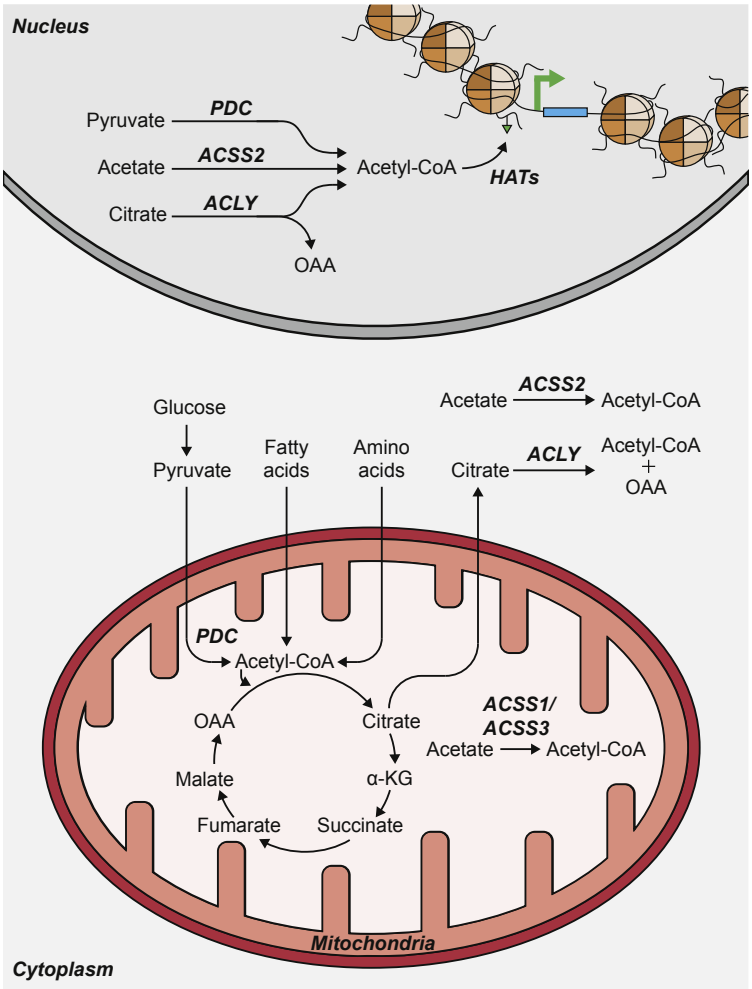

Figure 1.7: Compartmentalized acetyl-CoA metabolism. Acetyl-CoA pools occur in the mitochondria, the cytoplasm, and the nucleus. Nuclear acetyl-CoA can be generated by metabolic enzymes like PDC (pyruvate dehydrogenase complex), ACSS2 (acyl-CoA synthetase short-chain family member 2), and ACLY (ATP-citrate synthase) which normally reside in the mitochondria or cytoplasm. Produced Acetyl-CoA in the nucleus can be used by HATs (histone acetyltransferases) for the acetylation of histones which can lead to gene activation. Additional abbreviations: OAA (oxaloacetic acid), αKG (α-ketoglutarate) (Haws *et al*, 2020).

That the nucleus is a separated metabolic compartment was further highlighted by studies reporting the nuclear localization of metabolic enzymes, which normally locate in the mitochondria or the cytoplasm (Fig. 1.7). These metabolic enzymes were further shown to maintain their metabolic activity in the nucleus (Boukouris *et al*, 2016). Metabolic enzymes like PDC (pyruvate dehydrogenase complex) (Sutendra *et al*, 2014), ACLY (Wellen *et al*, 2009), ACSS2 (Wellen *et al*, 2009), and CRAT (Madiraju *et al*, 2009) were shown to be able to produce acetyl-CoA in the nucleus which can actually increase histone acetylation levels and influence gene expression. Intriguingly, even complete branches of the TCA cycle, such as citrate to succinate processing, can be performed in the nucleus (Kafkia *et al*, 2020). The recruitment of such enzymes into the nucleus might be involved in the generation of so-called subnuclear chromatin niches or microdomains in which site-specific acyl-CoA production for histone acyltransferases could be ensured. Such a metabolic niche within the nucleus could be generated for example by polymer–polymer or liquid-liquid phase separation (Erdel & Rippe, 2018; Sabari et al, 2020). A liquid-liquid phase separation (LLPS) can be induced by macromolecules concentrating into a liquid-like droplet which separates from a less concentrated phase. Macromolecules that are prone to condensation consist of multiple interaction domains, repeated structural domains, or intrinsically disordered regions (IDR) (Sabari *et al*, 2020). How also small metabolites might be involved in LLPS was studied by Houston *et al* (2020) and indeed acetyl-CoA removal induced nucleolus (an organelle formed upon LLPS) remodeling (Houston et al, 2020).

1.3.3. Diet and metabolic disorders affect the epigenome

Usually, metabolic networks can react and adapt towards different external inputs. Metabolic pathways can compensate for various changes, regulating for example the ratio between anabolic and catabolic reactions in order to maintain cellular function. Severe metabolic changes due to dietary changes can lead to an increased risk of diseases such as obesity, type 2 diabetes, cancer, or heart disease (Pitsavos *et al*, 2006). Due to the previously described link between metabolism and epigenetics, metabolic malfunctions can also disturb epigenetic mechanisms. Changes in the acyl-CoA concentration might for example affect the histone acylome and thereby initiate abnormal gene expression. In line with this, a reduction of acetyl-CoA levels was observed upon high-fat diet (HFD) in murine tissues like the liver, white adipose tissue (WAT), and pancreas. Interestingly, the acetyl-CoA reduction was reflected in decreased levels of H3K23ac in WAT and of H3K18ac and H3K23ac in the pancreas whereas no changes in histone Kac levels in the liver were observed (Carrer *et al*, 2017). Carrer and

colleagues also observed a significant loss of propionyl-CoA as well as a modest loss in butyryl-CoA levels in livers from HFD mice which was supported by decreased levels of H3K23pr and H3K18bu upon HFD (Nie *et al*, 2017). Controversially in another study on HFD mice, a significant increase in propionyl-CoA but hardly any changes for acetyl-CoA nor butyryl-CoA were observed (Liu *et al*, 2015) emphasizing how challenging studies on dietary changes can be.

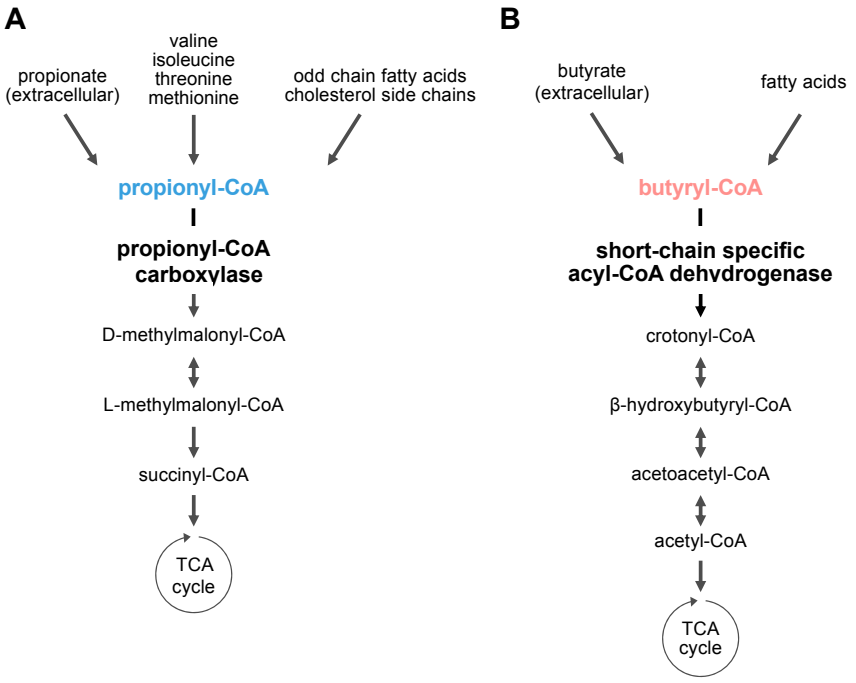

Figure 1.8: Metabolic pathways affected in metabolic disorders. Main sources which lead to the generation of propionyl-CoA (**A**) and butyryl-CoA (**B**) are indicated on top. **A** Propionic acidemia (PA) is caused by a malfunctional propionyl-CoA carboxylase (PA) that usually carboxylates propionyl-CoA to D-methylmalonyl-CoA which can further be converted to succinyl-CoA and fueled into the TCA cycle. **B** Short-chain specific acyl-CoA dehydrogenase (SCAD) deficiency affects the corresponding enzyme which converts butyryl-CoA to crotonyl-CoA in a first-step reaction during β-oxidation resulting in the generation of acetyl-CoA which can enter the TCA cycle. In both metabolic disorders C3 or C4 molecules accumulate (not shown) which can have toxic side effects (Wongkittichote et al, 2017; Goetzmann, 2011).

Drastic metabolic perturbations can also derive from genomic mutations. Examples for this are autosomal recessive metabolic disorders like propionic acidemia (PA) and short-chain acyl-CoA dehydrogenase (SCAD) deficiency (Pougovkina *et al*, 2014). PA results from mutations in the PCCA or PCCB genes encoding the α subunits respectively the β subunits of the propionyl-CoA carboxylase (PCC) (Ugarte *et al*, 1999). Usually, PCC is responsible for the carboxylation of propionyl-CoA to D-methylmalonyl-CoA in mitochondria which can further be converted to succinyl-CoA and fueled into the TCA cycle (Fig. 1.8A). Deficient PCC leads

to a toxic accumulation of propionyl-CoA and side products like propionylcarnitine, 2-methylcitrate, or 3-hydroxypropionate. PCC deficiency can cause tissue specific defects depending on the corresponding PCC expression level and sensitivity toward the accumulation of metabolites (Wongkittichote *et al*, 2017). The accumulation of propionyl-CoA was also reflected by an increase of propionylated proteins extracted from livers of propionyl-CoA carboxylase alpha subunit-deficient (*Pcca*$^{-/-}$) mice and from fibroblasts from PA patients (Kebede *et al*., 2017; Lagerwaard *et al*, 2021). Excitingly, the increase of propionyl-CoA can also lead to an increase of histone propionylation. Kebede *et al* (2017) observed an 1.3-fold increase of H3K14pr in liver samples from *Pcca*$^{-/-}$ mice in comparison to WT samples.

SCAD deficiency can be caused by point mutations in the ACAD (acyl-CoA dehydrogenase) gene region that encodes the short-chain acyl-CoA dehydrogenase (SCAD) which prefers butyryl-CoA as a substrate (Fig. 1.8B). SCAD and four additional ACADs are playing an important role in the β-oxidation of fatty acids in the mitochondria (Goetzmann, 2011). SCAD deficiency leads to an abnormal accumulation of butyryl-CoA, butyric acid and butyrylcarnitine among others. In symptomatic SCAD-deficient patients, one of the major symptoms is developmental delays due to the neurotoxic effects of described side products. In addition, since butyric acid is a known HDAC inhibitor, disrupted epigenetic mechanisms might also be involved during the progression of the disease (Jethva *et al*, 2008). Intriguingly, general protein butyrylation levels seemed elevated but H3K14bu levels remained unchanged in livers from *Acads*$^{-/-}$ mice, while H3K9bu seemed increased in heart samples from similar mice (Kebede *et al*, 2017; Yang *et al*, 2021). All in all, metabolic disorders like PA or SCAD deficiency might offer a more direct insight into the link between metabolism and epigenetics since their onset and progression is more defined than in a diet.

2. Aim of study

Even though the insights on the roles of different histone short-chain acylations started to increase recently, major open questions remain unanswered: Do non-acetyl acylations have a specific function that is different from the most abundant acetylation? Do histone acylations control transcriptional processes differently? Can histone acylations integrate metabolic fluctuations induced e.g. during development, by diet, or by disease, and help a cell to adapt towards it (Fig. 2.1)?

In need for answers, my first aim was to study the impact of short-chain lysine acylations on chromatin dynamics and I chose to focus specifically on H4K16 due to its unique and well-studied role on higher-order chromatin formation. I aimed to unravel the impact of H4K16ac, H4K16pr, and H4K16bu on the nucleosome-nucleosome interaction and nucleosomal stacking. I planned to use the insights from *in vitro* studies as a basis to address a possible biological role of H4K16 acylations *in vivo*. In addition, I aimed to study *in vivo* how dietary changes or metabolic diseases can influence short-chain lysine acylations and lock or unlock a specific cellular state potentially due to their effect on chromatin dynamics (Fig. 2.1). For this, I decided to focus on high-fat diet treated mice as well as on mice models for propionic acidemia (PA) and short-chain specific acyl-CoA dehydrogenase (SCAD) deficiency.

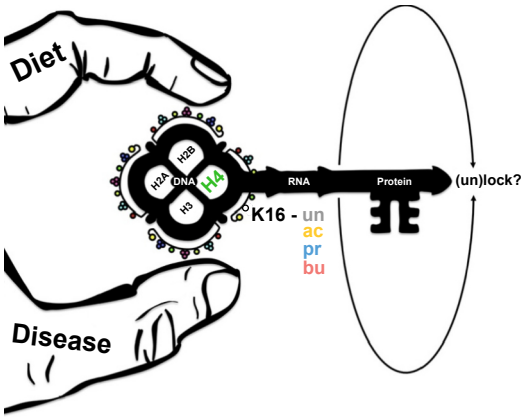

Figure 2.1: Interplay between metabolism and epigenetics. The fingers of a hand are representing external factors like diet or disease that are influencing the central dogma of molecular biology: A flow of genetic information from DNA to RNA to protein is represented as a key. Epigenetic modifications of core histones (H2A, H2B, H3, H4) allow the integration of external information to lock or unlock a specific cell state. Highlighted are H4K16 modifications (un: unmodified, ac: acetylated, pr: propionylated, bu: butyrylated) (modified from Yung & Elsässer, 2017).

3. Results

3.1. H4K16 acylations and their role in chromatin compaction

3.1.1. The preparation of the building blocks: Octamers with acylated H4K16

How various H4K16 acylations affect chromatin dynamics can be best studied in highly controllable and well-defined *in vitro* assays. We incorporated different *in vitro* studies in this thesis to get a deeper insight into the potential control of chromatin de-compaction upon H4K16 acylations. One essential component for such assays are site-specifically and fully acylated histones that can be used for the refolding of histone octamers and subsequent assembly of "designer" chromatin. For the generation of such histones, we chose the native chemical ligation approach (Fig. 3.1). Chemically synthesized peptides of histone H4 with or without acylations on lysine 16 were ligated to recombinant truncated H4 (human). In total, four different full-length H4 were generated: unmodified (un), acetylated (ac), propionylated (pr), and butyrylated (bu) H4K16.

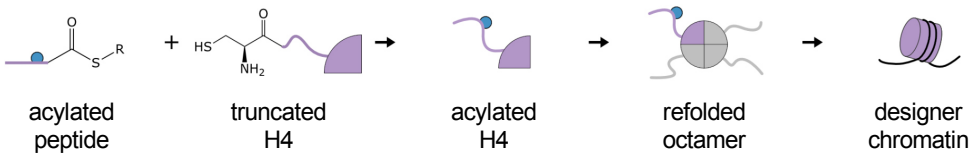

Figure 3.1: Site-specifically acylated "designer" chromatin. During the native chemical ligation, the thioester of an acylated H4 peptide is linked to the cysteine of truncated H4. Acylated histones and remaining core histones can be used to refold octamers and assemble designer chromatin on favored DNA templates.

We purified expressed truncated H4 by gel filtration chromatography (Fig. 3.2A) and combined only positive fractions (14-19). We further purified combined peak fractions by reversed-phase chromatography (Fig. 3.2B). We again combined only positive fractions (29 to 36) containing truncated H4 and lyophilized them for the native chemical ligation. After the ligation of H4 peptides to purified truncated H4, full-length H4 was purified via reversed-phase chromatography (Fig. 3.3A). We observed full-length H4 on an SDS-PAGE stained with coomassie (Fig. 3.3B-E). For the refolding of octamers, we used unmodified core histones H2A, H2B, and H3.1 and purified the obtained octamers by gel filtration chromatography. The elution profile of refolded octamers containing H4K16un is shown in Fig. 3.4. Only fractions with stoichiometric amounts of all four core histones were pooled and were used for the assembly of different designer chromatin (Fig. 3.4B-E).

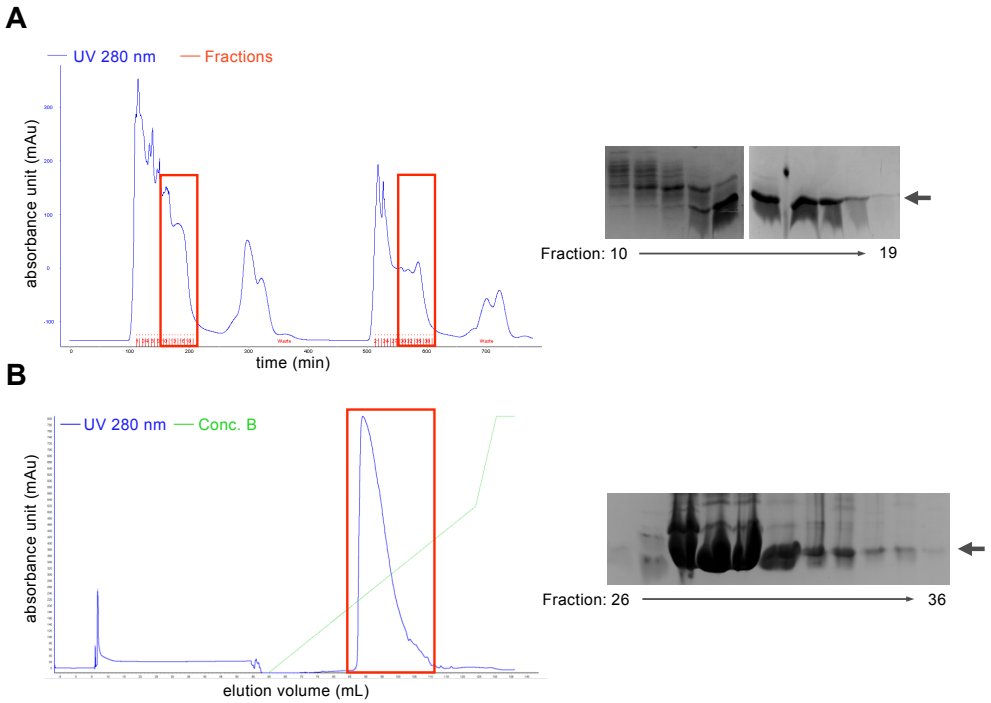

Figure 3.2: Purification of truncated H4. A Recombinant truncated H4 was purified first by gel filtration chromatography using a HiPrep 26/60 Sephacryl S-200 HR column. Shown is the Äkta™ elution profile (left) in which the absorbance at 280 nm is indicated by the blue line while collected fractions are marked in red. Highlighted peak regions (red squares) were checked by SDS-PAGE and coomassie staining (right). Only fractions with pure truncated H4 (indicated by arrow) were combined (fractions 14-19). **B** Pooled fractions from A were further purified via reversed-phase chromatography using a Resource RPC column over a 0 – 65 % buffer $B_{trunc.}$ gradient which is indicated in the chromatogram in a green line (left). Indicated by the blue line is the absorbance at 280 nm. Peak fractions (red square) were analyzed by SDS-PAGE and coomassie staining (right). Positive fractions of truncated H4 (indicated by arrow) were combined (fractions 29-36) and used for the native chemical ligation. In both chromatograms, the absorbance units (mAu) are plotted on the y-axis while the x-axis is the elution time (min) respectively volume (mL).

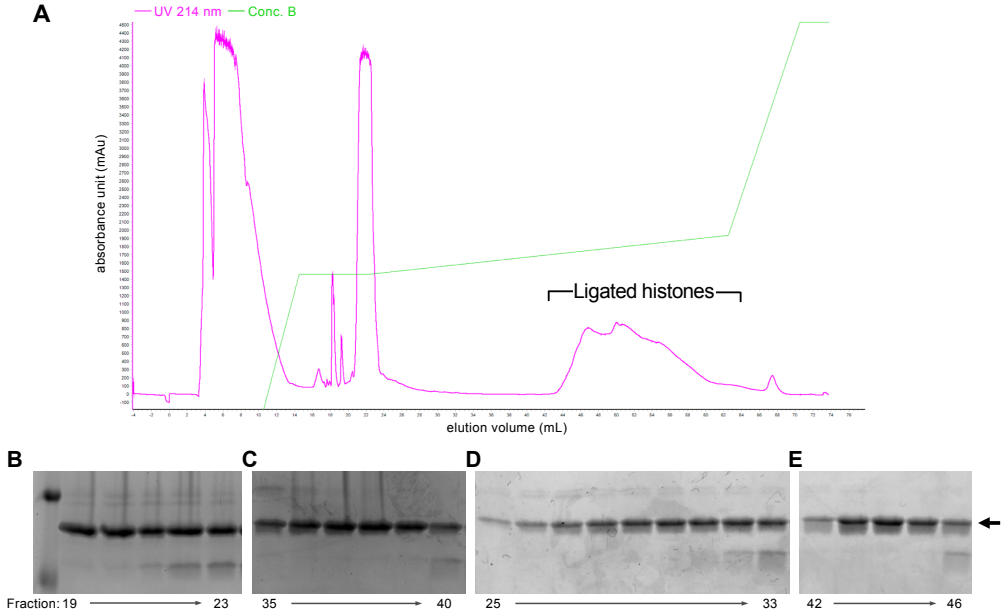

Figure 3.3: Native chemical ligation of acylated H4K16. A Example for an Äkta™ elution profile of the purification of ligated H4 (here shown H4K16ac) via a reversed-phase chromatography using a C-8 Perkin Elmer Aquapore RP-300 250x4.6 column. In the chromatogram, the absorbance units (mAu) are plotted on the y-axis while the x-axis is the elution volume (mL). Ligated H4 was eluted via a prolonged gradient of buffer $B_{ligation}$ (green line). Indicated by the pink line is the absorbance at 214 nm. Peak fractions containing ligated histones were analyzed by SDS-PAGE and coomassie staining (**B-E**). Only fractions with full-length H4 were combined (arrow). Peak fractions of H4K16un (**B**), H4K16ac (**C**), H4K16pr (**D**) and H4K16bu (**E**) are shown.

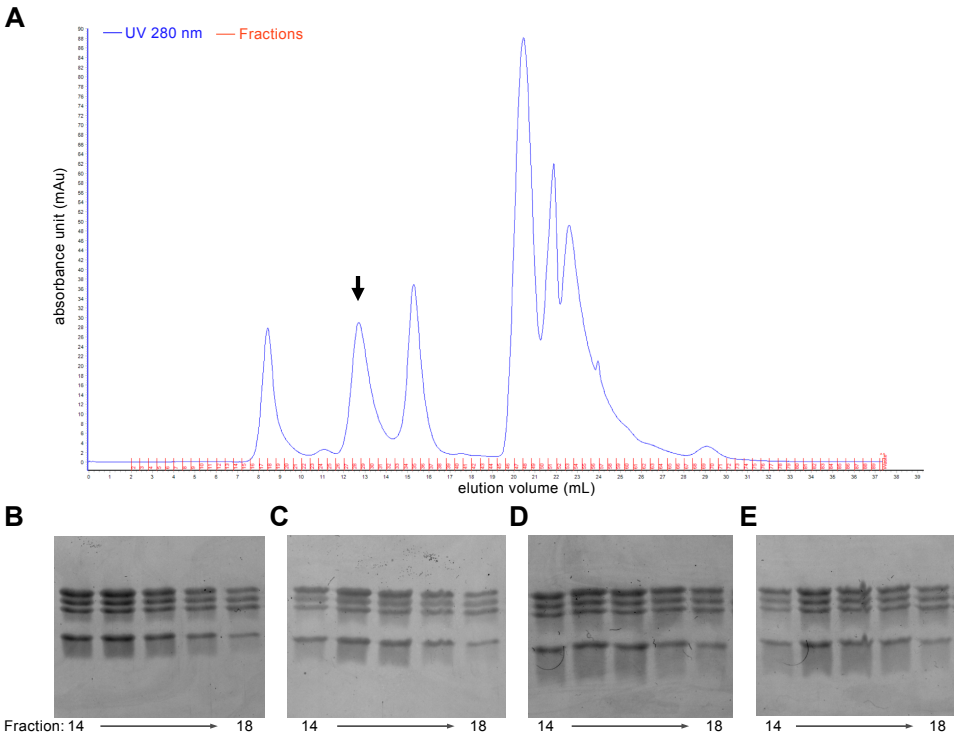

Figure 3.4: Purification of refolded histone octamers. A Octamers were purified over a Superdex-200 16/60 Prep Grade gel filtration column. Shown is an example of an Äkta™ elution profile of refolded histone octamers. In the chromatogram, the absorbance units (mAu) are plotted on the y-axis while the x-axis is the elution volume (mL). Indicated by the blue line is the absorbance at 280 nm while collected fractions are marked in red. Peak fractions (indicated by arrow) were analyzed by SDS-PAGE and coomassie staining. (**B-E**). Only fractions with stoichiometric amounts of all four core histones were pooled. Peak fractions of octamers containing H4K16un (**B**), H4K16ac (**C**), H4K16pr (**D**), and H4K16bu (**E**) are shown.

To sum up, we successfully generated the essential components for the various *in vitro* assays that are described in the next sections.

3.1.2. H4K16 acylations affect internucleosomal interaction

Direct interaction between neighboring nucleosomes is central for chromatin compaction. This interaction can be repulsive or attractive depending for example on the histone modifications. The team of Prof. Hendrik Dietz (TUM, München, DE) established a DNA origami-based force spectrometer which is a DNA-based nanoscale folding that resembles the shape of a stapler (Fig. 3.5A). Such a force spectrometer can be used to measure the interaction strength between neighboring mono-nucleosomes due to its flexible hinge region (Funke et al, 2016). We teamed up with the Dietz lab (direct help: Dr. Jonas Funke and Natalie Möritz) in order to study the effect of H4K16 acylations on internucleosomal interactions. We assembled mono-nucleosomes by using a modified nucleosomal 1xwidom-601 positioning sequence which allows site-specific integration into the force spectrometer (Fig. 3.5A). Successfully assembled

mono-nucleosomes (Fig. 3.5B) were then incubated with DNA origami structures at 5 mM $MgCl_2$ and the open angles of at least 300 structures were measured. Examples of loaded force spectrometers with different opening angles are shown in Fig. 3.5C.

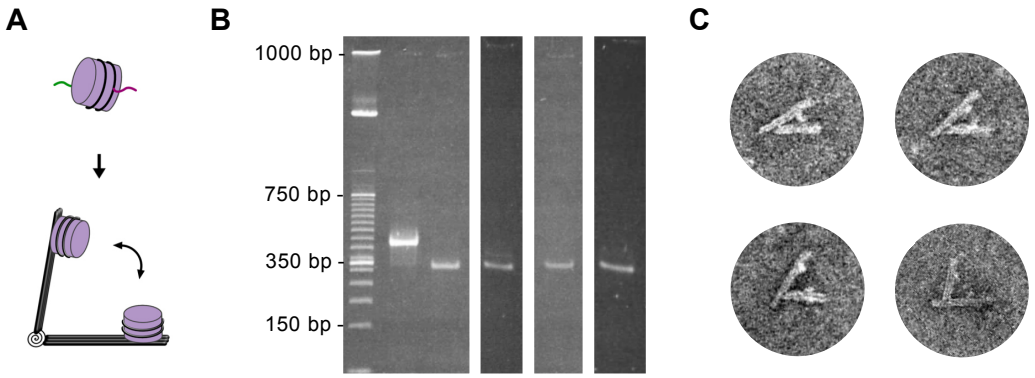

Figure 3.5: Preparations for DNA origami-based force spectrometer measurements. A Assembled mono-nucleosomes with single-stranded DNA handles (green and purple) can be specifically placed into the DNA origami-based force spectrometer. The flexible hinge regions allows nucleosomes to interact if forces are attractive. **B** Assembly of mono-nucleosomes by salt gradient dialysis was controlled on a native 5% PAGE. On ethidium bromide-stained gels no free DNA (lane 1) was observed in assembled H4K16un (lane 2), H4K16ac (lane 3), H4K16pr (lane 4) and H4K16bu (lane 5) containing mono-nucleosome. **C** Exemplary electron micrographs show differently opened DNA origami structures loaded with mono-nucleosomes.

The distribution of angles for the acylated nucleosomes in comparison to unmodified nucleosomes is shown in Fig. 3.6A. For most of the structures loaded with unmodified nucleosomes smaller angles were measured (< 40°), whereas upon the incorporation of acylated nucleosomes, fewer structures were detected in this rather closed formation. Spectrometers containing acylated nucleosomes were more likely to be open (> 40°). In comparison, structures loaded with unmodified nucleosomes were less likely to have angles above 40°. These angle distributions already suggested that H4K16 acylations might decrease internucleosmal interactions in a similar way.

We first calculated the free energies assuming Boltzmann statistics by using the probability densities (Fig. 3.6B) and then we computed the free-energy landscapes (Fig. 3.6C). The free energy minimum was the lowest for H4K16un (-1,86 kcal/mol) and the highest for H4K16ac (-1,33 kcal/mol). The minima for H4K16pr and H4K16bu were in between (H4K16pr: -1,73 kcal/mol, H4K16bu: -1,53 kcal/mol). In general, these minima were located around 6 nm and only for H4K16pr it shifted towards 4 nm. For the quantification of the pure internucleosomal interaction strength, we calculated the area above the free-energy landscapes (Fig. 3.6D). After the normalization towards H4K16un, H4K16ac appeared to have the weakest interaction strength. Interestingly, non-acetyl acylations also were able to reduce the internucleosomal interaction strength. H4K16pr seemed to reduce the interaction slightly more than H4K16bu.

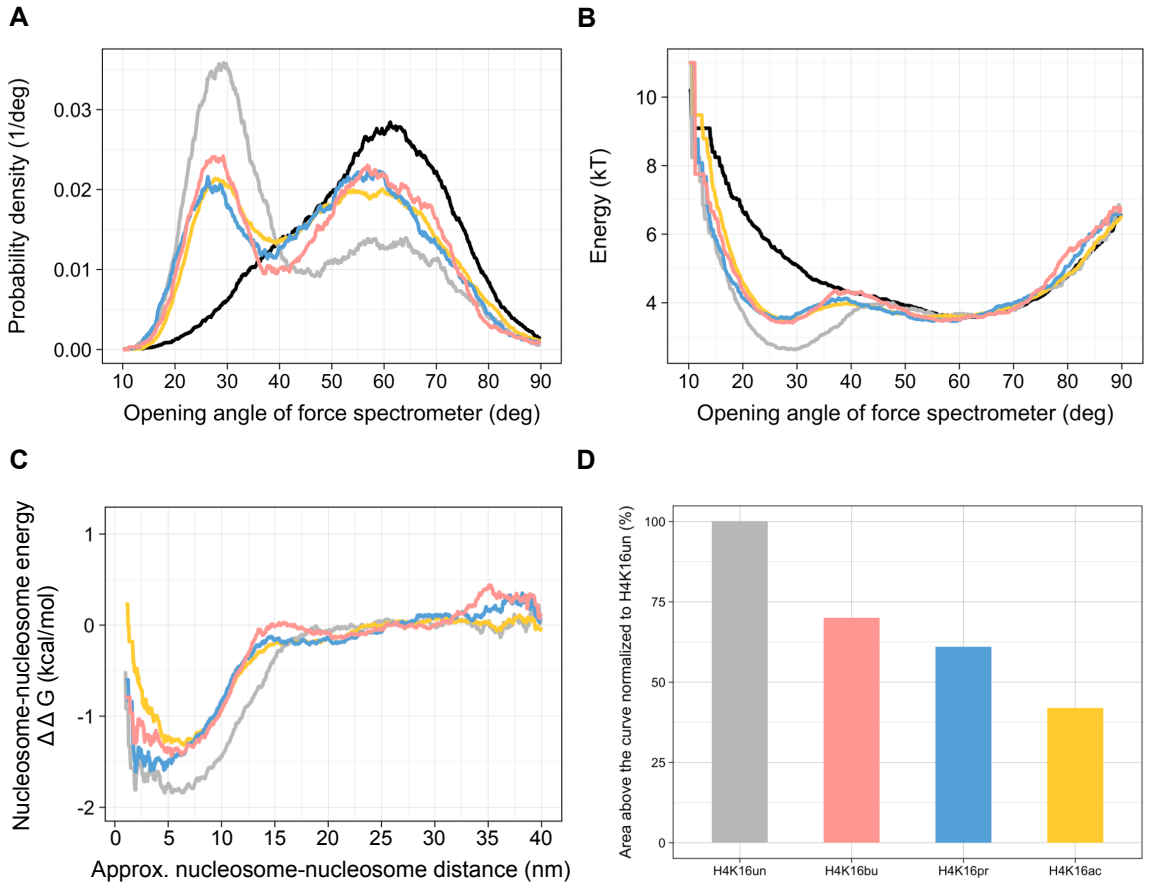

Figure 3.6: Nucleosome-nucleosome interaction analysis. A Angle distribution of DNA origamis loaded with unmodified (grey) or acylated nucleosomes (coral pink: H4K16bu, blue: H4K16pr, yellow: H4K16ac). Plotted is the probability density (1/deg) against the opening angle of the force spectrometer (deg). At least 300 particles for each modification were measured. The black line indicates the angle distribution of empty DNA origamis. **B** Free energy was computed by considering Boltzmann statistics. The used angle distribution from A was normalized between 50 and 90°. Plotted is the energy (kT) against the opening angle of the force spectrometer (deg). Black line: free energy of empty DNA origamis. **C** The uniform kernel density estimates the nucleosome-nucleosome interaction energy landscapes which are plotted as a function of the distance between the nucleosomes. Plotted is the nucleosome-nucleosome energy ΔΔG (kcal/mol) against the approximately nucleosome-nucleosome distance (nm). **D** The interaction strength for acylated nucleosomes (x-axis) was calculated by the area above the free energy landscapes and normalized to H4K16un (y-axis).

3.1.3. H4K16 acylations affect nucleosomal stacking

To further investigate the influence of H4K16 acylations on internucleosomal interactions, we collaborated with the lab of Prof. Beat Fierz (direct help: Dr. Harsh Nagpal, EPFL, Lausanne, CH) who established a nucleosome stacking assay based on single-molecule Förster resonance energy transfer (FRET). For this versatile tool, we used our refolded octamers with a 12x repeat of a nucleosome positioning sequence (12xwidom-601) that has a similar length as a small gene (~2000 bp long). This positioning sequence was decorated with one FRET donor and one FRET acceptor dye. These fluorescent labels were specifically added at two positions: At nucleosome position 5 with the donor (Alexa568, yellow) and at position 7 with the acceptor (Alexa647, red). As shown in Fig. 3.7A. the assembled "designer" chromatin contained 12 nucleosomes

and only the central neighboring nucleosomes were labeled, allowing to study nucleosomal stacking. The arrays were first assembled by titration of different ratios between octamers and DNA (Fig. 3.7B). Since Sca1 sites were located in between the nucleosome positioning sequences, Sca1 digestion was performed to check the assembly efficiency. As indicated in Fig. 3.7C, mono-nucleosomes can be observed for all titrations but only in the last set-up, no MMTV nucleosomes were detected.

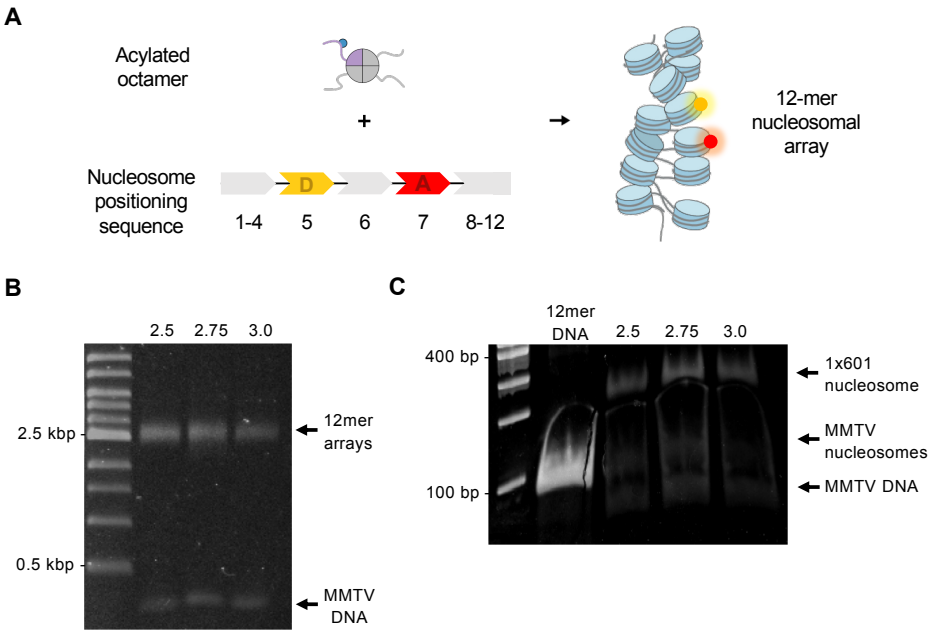

Figure 3.7: Preparations for nucleosomal stacking assays. A This illustration shows the assembly of 12-mer nucleosomal arrays (right) using acylated octamers and a specific nucleosome positioning sequence that carries fluorescent labels at nucleosome 5 (yellow, D: FRET donor) and 7 (red, A: FRET acceptor). The nucleosomal array (right) was adapted from Kilic *et al* (2018). **B** This SYBR green stained agarose gel shows 12-mer nucleosomal arrays resulting from titrating the octamer:DNA ratio (2.5-3.0) as well as free competitor DNA (MMTV DNA). **C** Shown is an SYBR green stained agarose gel onto which Sca1 digested arrays from B were loaded. Mono-nucleosomes were detected on all reactions (1x601) on this SYBR green-stained agarose gel. Only with a ratio of 3.0 almost no MMTV nucleosomes and free MMTV DNA were detected.

Nucleosomal stacking assays were performed at 0 mM and 4 mM $MgCl_2$ and measured FRET efficiencies (E_{FRET}) were compared. The E_{FRET} traces for unmodified 12-mer nucleosomal arrays are shown in Fig. 3.8. Upon the addition of salt, a second population with higher FRET efficiency values (0.4 - 0.8) appeared indicating the compaction of unmodified arrays. We then compared how acylated 12-mer nucleosomal arrays behaved upon the addition of 4 mM $MgCl_2$ in comparison to unmodified arrays (Fig. 3.9).

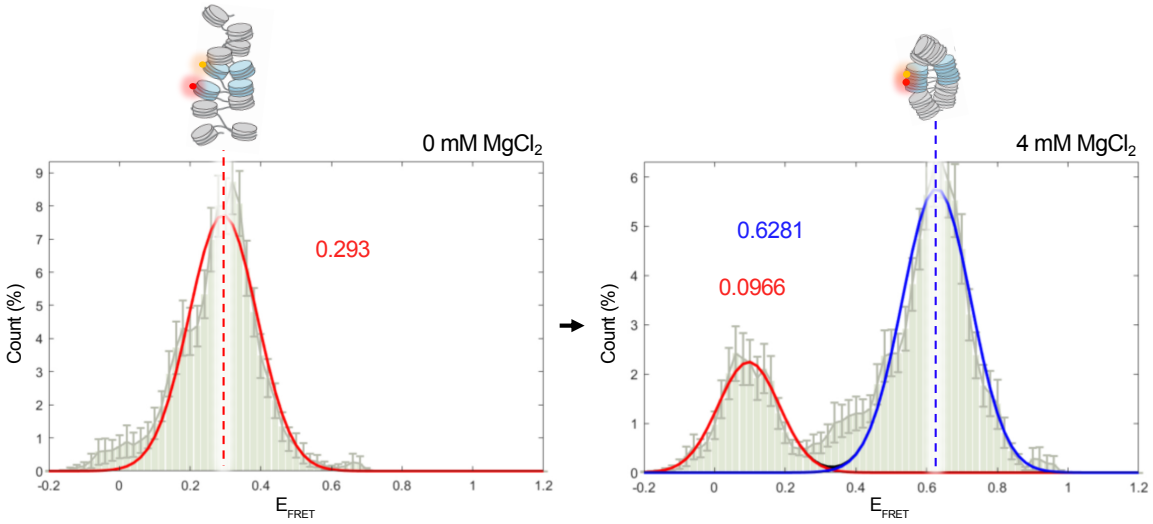

Figure 3.8: Nucleosomal stacking of unmodified 12-mer nucleosomal arrays. Shown are FRET traces for unmodified arrays at 0 mM (left) and at 4 mM $MgCl_2$ (right). Plotted are the FRET counts (%) against the FRET efficiency (E_{FRET}). At 0 mM $MgCl_2$, the mean of the first FRET population (red) is located at 0.293 and reflects mainly open arrays (illustration on top). The addition of 4 mM $MgCl_2$ caused a second FRET population (blue) with an increased E_{FRET} (mean: 0.6281) indicating nucleosomal stacking and compaction of the arrays. The illustrations of 12-mer nucleosomal arrays (on top) were adapted from Kilic *et al* (2018).

For all acylated arrays, we observed a major FRET population with mean E_{FRET} values between 0.05 to 0.1, and no second FRET population with E_{FRET} values comparable to the ones from unmodified arrays (E_{FRET} mean: 0.6) was obvious. We further detected an increased count for FRET signals for arrays with increasing acyl chain length (bu>pr>ac, Fig. 3.9A)) and decided to calculate the area under the curve of the first FRET population (-0.2 to 0.3 E_{FRET} values). After normalization to unmodified arrays, we observed a 2-fold increase for H4K16bu and H4K16pr while for H4K16ac the increase was 1.6 fold (Fig. 3.9B).

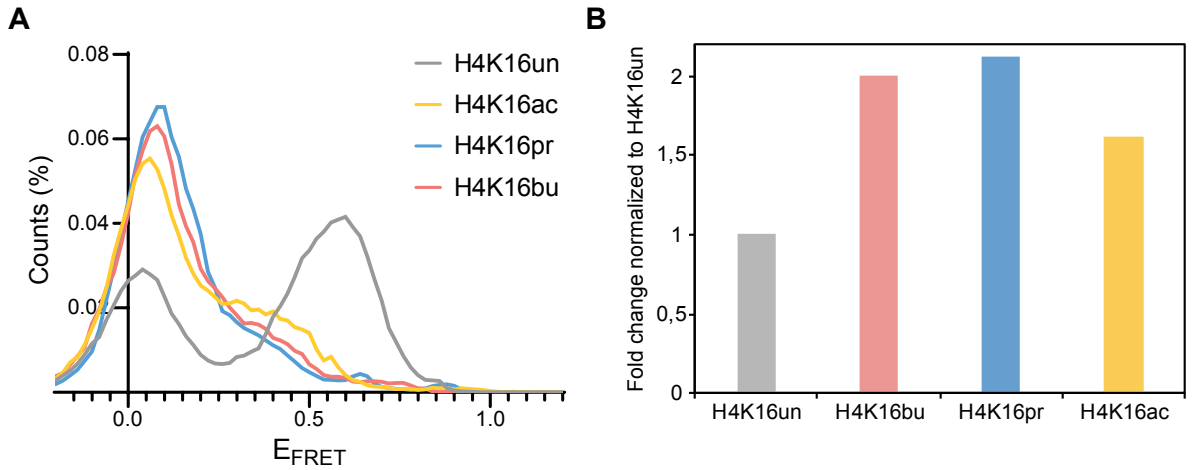

Figure 3.9: Nucleosomal stacking of acylated arrays. A Shown are FRET traces for H4K16un (grey), H4K16ac (yellow), H4K16pr (blue), and H4K16bu (coral pink) 12-mer nucleosomal arrays at 4 mM Mg^{2+}. Plotted are the counts (%) against the FRET efficiencies (E_{FRET}). For acylated arrays, E_{FRET} remained low (<0.3) while for unmodified arrays higher E_{FRET} values were observed (>0.3). **B** Areas under the curve for the detected FRET populations with E_{FRET} values below 0.3 were computed. In this bar plot, the fold change of calculated areas normalized to unmodified arrays is plotted. A 2-fold increase for H4K16bu (coral pink) and H4K16pr (blue) was detected while for H4K16ac (yellow) the increase was 1.6-fold.

Via these measurements, we demonstrated that H4K16 acylations can interfere with nucleosome stacking. H4K16bu and H4K16pr appeared to inhibit nucleosomal stacking more than H4K16ac.

3.2. Epigenetic players and H4K16 acylations

We wondered if non-acetyl acylations can recruit specific interactors like writers, erasers, or readers that are different from interactors recognizing acetylations. Since previous studies showed that traditional HATs can also use other acyl-CoAs as their co-factor (Simithy *et al*, 2017), we first investigated the activity of the main HAT responsible for H4K16 acetylation: MOF (KAT8).

3.2.1. MOF can propionylate and butyrylate H4K16 *in cellulo*

We decided to directly check the potential activity of MOF towards H4K16pr and H4K16bu *in cellulo*. For this reason, we received mouse embryonic fibroblasts (MEFs) derived from a conditional knockout *Mof* $^{flox/flox}$ *Cre*$^{+}$ mouse model that was established in the lab of Prof. Yali Dou (USC, Los Angeles, USA). We deleted *Mof* via 4-hydroxytamoxifen (4-OHT)-induced expression of the Cre recombinase. More precisely, these MEFs had to be treated at least for four days with 4-OHT for an efficient *Mof* KO (Fig. 3.10A).

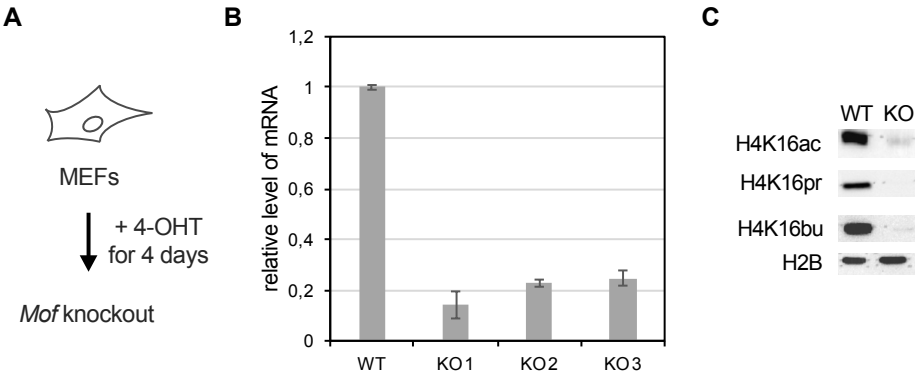

Figure 3.10: MOF acts as a histone acyltransferase *in cellulo*. A An illustration of *Mof* KO induction via 4-hydroxytamoxifen (4-OHT) treatment of *Mof* knockout mouse embryonic fibroblasts (MEFs) for at least four days. **B** After four days of 4-OHT treatment, *Mof* expression was observed via qPCR in comparison to untreated cells (WT). Plotted is the relative level of mRNA for WT and KO cells (KO1-3: 3 different inductions). The average of two technical replicates and STD is shown. **C** Histones were extracted from induced *Mof* KO cells and uninduced MEFs (WT). Shown is an immunoblot using antibodies against H4K16ac, H4K16pr, and H4K16bu that revealed a reduction of H4K16 acylations upon *Mof* KO. H2B was used as a loading control.

After the 4-OHT-induced expression of Cre recombinase for four days, we observed a strong reduction in *Mof* expression (Fig. 3.10B). This successful *Mof* KO resulted in a severe loss of

H4K16ac, H4K16pr, and H4K16bu (Fig. 3.10C). These results confirm that MOF can act as a histone propionyltransferase *in cellulo* (Han *et al*, 2018) and also defines MOF as a novel histone butyryltransferase.

3.2.2. Identification of H4K16 acylation-specific interactors

For the identification of acylation-specific binders towards H4K16pr and H4K16bu, we performed affinity purifications with modified H4 peptides. We decided on such a peptide-based affinity purification since it allowed us to study direct and pure interactions between histone acylations and proteins. H4 peptides were immobilized on agarose beads and incubated with nuclear extract from HeLa cells. Interacting proteins were identified via MS with the help of the lab of Prof. Michiel Vermeulen (direct help: Pascal Jansen, Radboud Institute for Molecular Life Sciences, Nijmegen, NL) (Fig. 3.11).

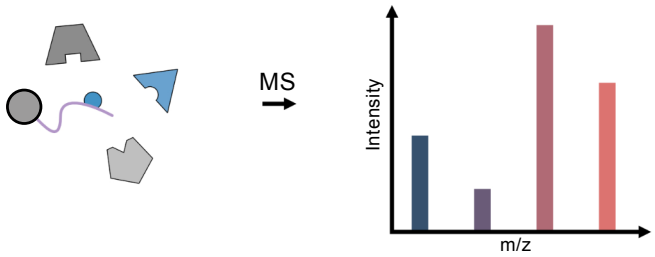

Figure 3.11: Peptide-based affinity purification. Schematic of a peptide (purple line, left) based affinity purification in which interactors (grey and blue, angular shapes) from HeLA nuclear extract can bind and be identified via MS. On the left a modified (blue circle) H4 peptide is immobilized on an agarose bead (grey circle). Different potential interactors are shown. Specific interactors (blue, angular shape) can be identified via MS and peptide mass fingerprinting. Shown on the right is a schematic peptide mass fingerprinting spectrum in which detected intensities are plotted against the mass (m/z).

As the heatmap of identified interactors in Fig. 3.12 shows, most proteins were binding to unmodified H4K16. Only few interactors for H4K16 acylations were identified as further highlighted by the volcano plots in Fig. 3.13A-C. A Sirtuin family member namely SIRT3 was identified as an interactor of H4K16ac and H4K16pr but not of H4K16bu. We aligned the detected peptides from the MS to identify the interacting SIRT3 isoform but since the peptides overlapped with a shared region we further validated the interaction by immunoblotting (Fig. 3.13D) and revealed that apparently, only the short isoform can bind to H4K16ac and H4K16pr.

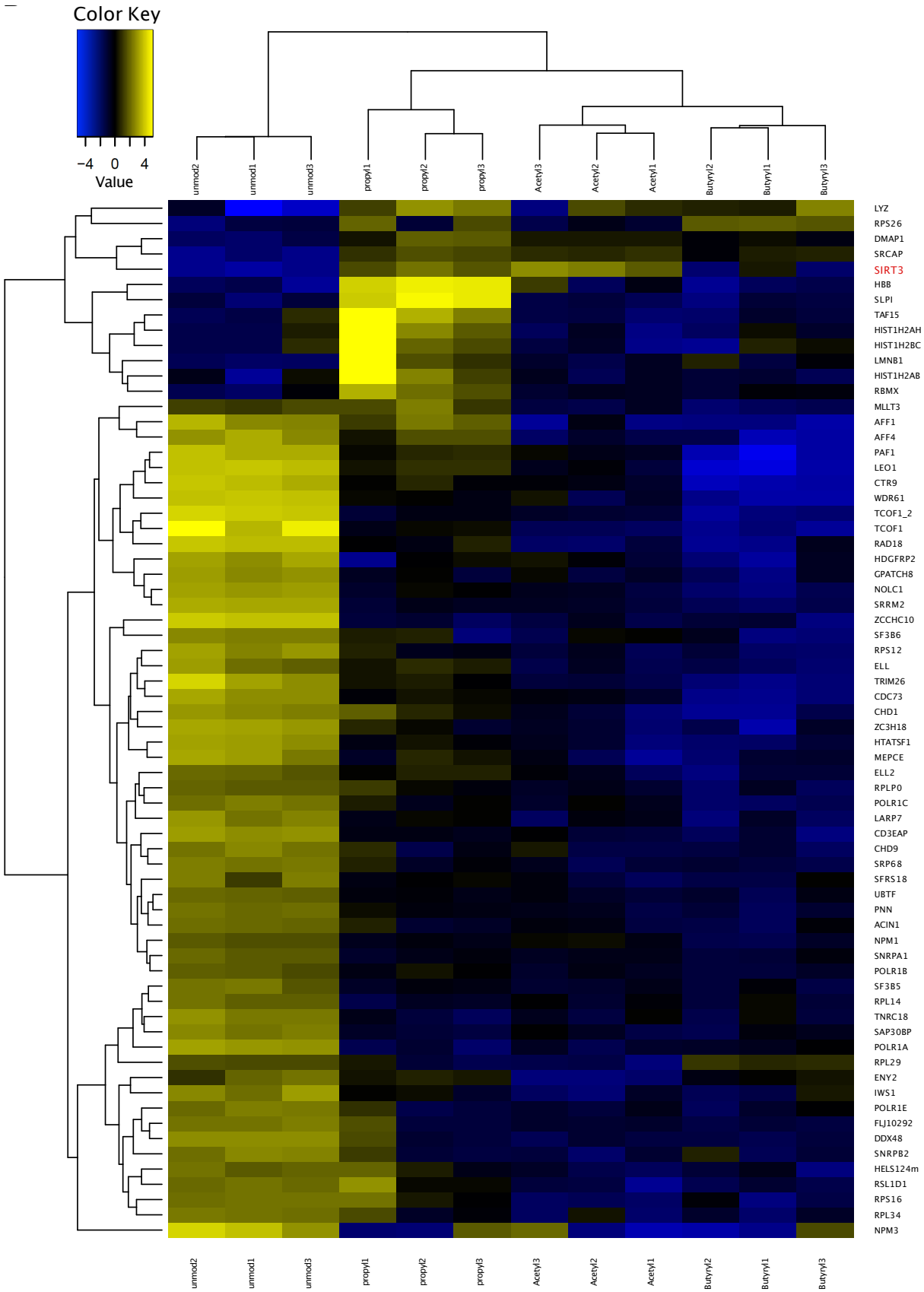

Figure 3.12: H4K16 acylation interactors. Euclidean clustering heatmap of proteins identified by mass spectrometry. Preferred binding of interactors towards different H4K16 peptides is shown. Unmodified (unmod 1-3), acetylated (acetyl 1-3), propionylated (propyl 1-3) and butyrylated (butyryl 1-3) H4K16 peptides were used. Peptide-based affinity purification were prepared in triplicate and were done using HeLa nuclear extracts and H4 tail peptides.

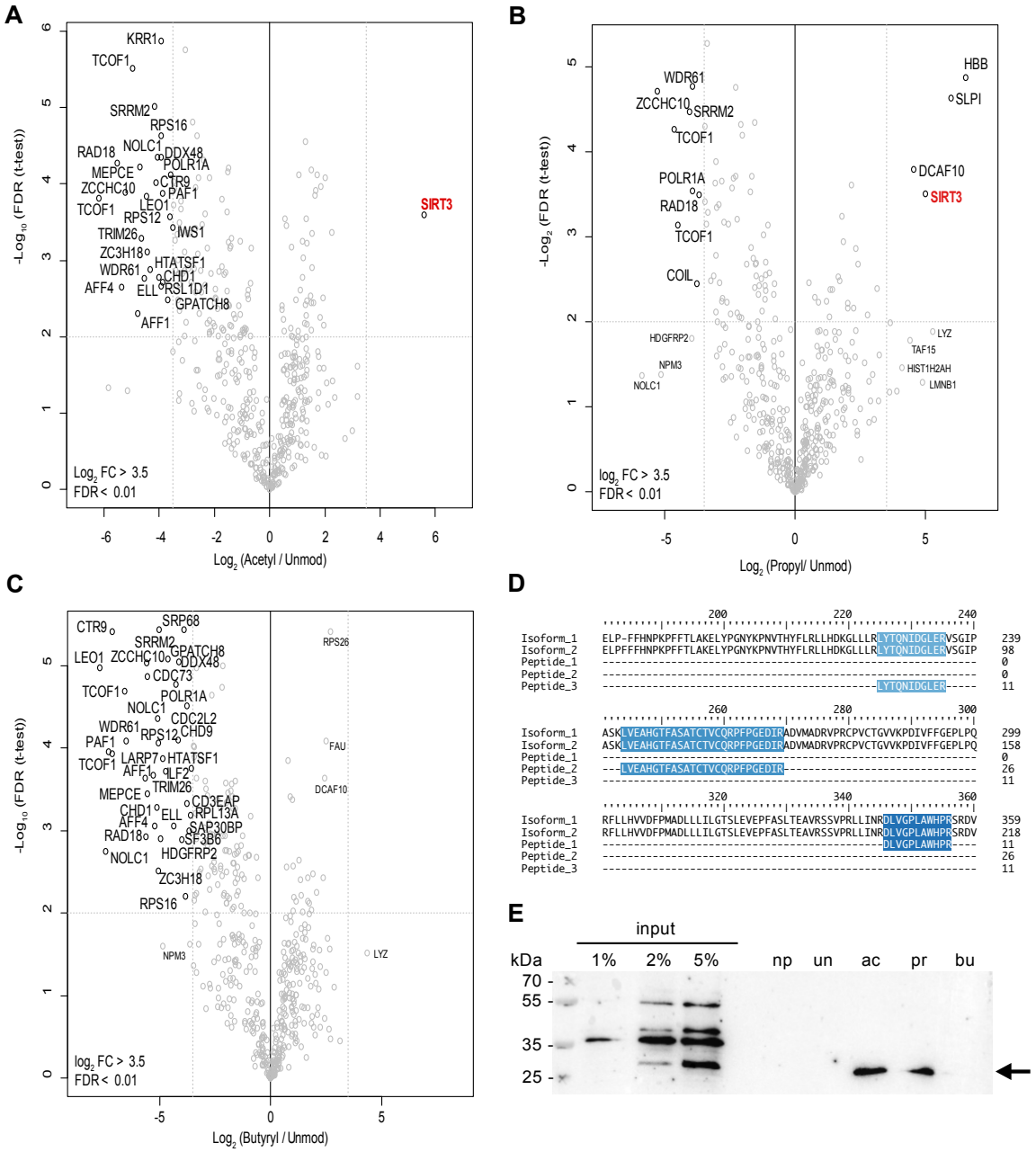

Figure 3.13: Acylation-specific binding of SIRT3. Volcano plots show interactors that are depleted or enriched for H4K16ac (**A**), H4K16pr (**B**), and H4K16bu (**C**) over H4K16un. Shown interactors passed a cut-off of log_2Foldchange > 3.5 and log_2FDR < 0.01. The -log_{10} (FDR(t-test)) is plotted on the y-axis while the x-axis is the log_2 change between H4K16 acylations and H4K16un **D** Alignment of identified SIRT3 peptides (Peptide_1-3) interacting with H4K16ac and H4K16pr with the different isoforms of SIRT3 (Isoform_1/2). Overlapping regions are highlighted in blue. **E** Binding of the shorter SIRT3 isoform (indicated by arrow) to H4K16ac (ac) and H4K16pr (pr) but not H4K16bu (bu) was validated via immunoblot using SIRT3 specific antibody. As a negative control beads with no H4 peptides were used (np). Indicated amounts of input were loaded as control.

3.3. H4K16 acylations and transcriptional activity

The results from the DNA origami-based force spectrometer (3.1.2), as well as the nucleosomal stacking assays (3.1.3), suggested that H4K16 acylations might fine-tune internucleosomal interactions to a different degree and therefore potentially also general chromatin dynamics. Reduced internucleosomal interactions upon histone acetylations are mainly linked to open and

accessible chromatin and active genomic regions (Verdin & Ott, 2014). Thus, we decided to study the direct effect of histone acylations on transcription via a well-established *in vitro* transcription (IVT) assay.

3.3.1. Purification of assembled chromatin via a sucrose gradient

Designer chromatin for the IVT was assembled via the ATP-dependent histone chaperone NAP1 (nucleosome assembly protein 1) and the chromatin remodeling complex ACF (ATP-utilizing chromatin assembly and remodeling factor). As a DNA template, the previously established pG5-MLP plasmid was used (Dignam *et al*, 1983). This plasmid contains five GAL4-binding domains upstream of a viral promoter MLP (major late promoter). Downstream of the promoter is a 380 bp G-less transcription cassette that will remain the only transcript after an RNase T1 digestion which allows quantitative comparisons between different IVT reactions (Fig. 3.14A). For the assembly of IVT chromatin we only used supercoiled pG5-MLP plasmids (Fig. 3.14B) and the efficiency of the chromatin assembly was controlled via MNase digestion.

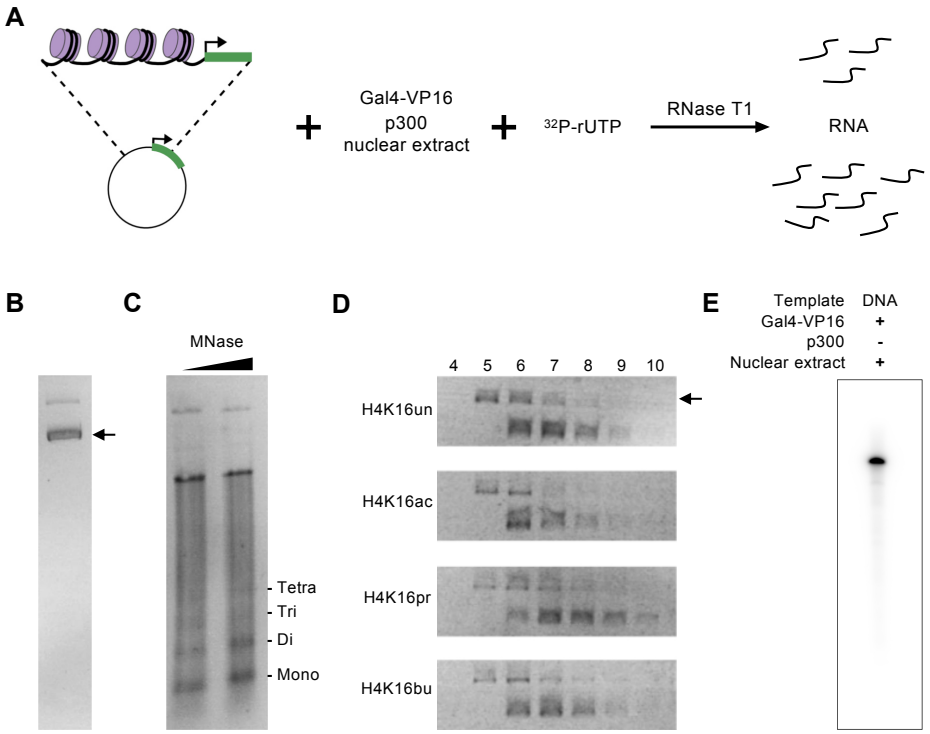

Figure 3.14: Set-up for the IVT approach. A Schematic overview of ATP-dependent circular chromatin assembly using supercoiled pG5-MLP plasmid. Transcription of 380 bp G-less cassette (green) is stimulated by activators (Gal4-VP16, p300) and the transcriptional machinery (provided in the nuclear extract). The incorporation of ^{32}P-rUTP allows quantification of produced transcripts that after RNase T1 cleavage only derived from the G-less cassette. **B** Purification via a CsCl gradient results in the enrichment of supercoiled pG5-MLP plasmid (arrow). Shown is a 1.3 % agarose gel stained with 10 µg/mL ethidium bromide after electrophoresis. Same conditions were used in C and D. **C** Chromatin assembly efficiency was checked by MNase digestion (3 U and 6 U of MNase). Chromatin for which a ladder of at least four nucleosomes was detected was used for the IVT. **D** Assembled chromatin was purified via a linear sucrose gradient. For all acylations fractions, 5 to 7 were combined and used for the IVT. **E** As a positive control for the IVT, the pG5-MLP plasmid was used with Gal4-VP16 and nuclear extract. In the shown autoradiogram, transcripts resulting from the G-less cassette were detected.

For the actual IVT reaction, we used fully reconstituted chromatin with a nucleosomal ladder of at least four nucleosomes upon MNase digestion (Fig. 3.14C) and we further purified this chromatin by a linear sucrose gradient. The same fractions were combined for all types of chromatin and were used for the IVT (Fig. 3.14D). The pG5-MLP plasmid was used as a positive control during the IVT to confirm that all the components e.g. the nuclear extract and Gal4-VP16 were active and properly prepared (Fig. 3.14E).

3.3.2. H4K16 acylations stimulate transcription *in vitro*

We prepared IVT reactions for H4K16un, H4K16ac, H4K16pr, and H4K16bu chromatin. Since after the sucrose gradient some free plasmid DNA was detected (Fig. 3.14D), IVT reactions were set up with and without p300 to detect transcription resulting from the remaining free DNA and from actual chromatin (Fig. 3.15A). The signal detected of the IVT resulting from free DNA was subtracted from the chromatin-based IVT reactions and the remaining signal was normalized to H4K16un (Fig. 3.15B).

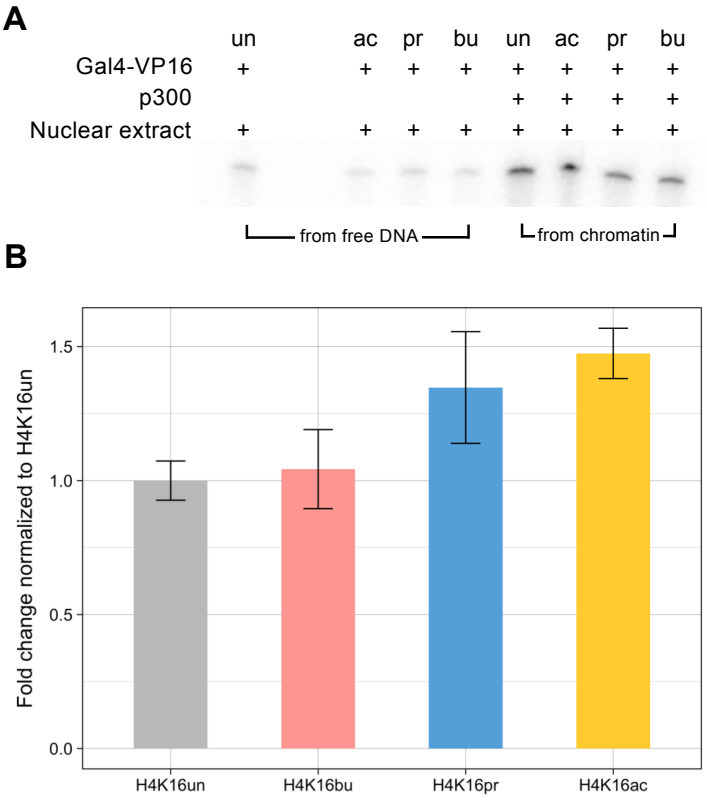

Figure 3.15: H4K16 acylations stimulate transcription *in vitro*. A Two IVT reactions were prepared for the assembled chromatin: One without p300 (left) to detect transcription of free DNA and the other one with p300 (right) to detect transcription of actually assembled chromatin. **B** Transcript signals detected from free DNA were subtracted from the transcription signal of assembled chromatin signal. Remaining transcription intensities were normalized to H4K16un. N=2, error bars = STD.

Via the IVT, we were able to demonstrate that H4K16ac stimulated transcription the most. H4K16pr stimulated transcription almost as much as H4K16ac whereas H4K16bu did not seem to stimulate transcription in comparison to H4K16un.

3.4. The nuclear and genomic distribution of H4K16 acylations

3.4.1. Purification of site-specific antibodies against acylated H4K16

In addition to the so far presented biochemical approaches focusing on chromatin dynamics, we also wondered about the roles of these H4K16 acylations *in vivo*.

To be able to address such questions, acyl-specific and site-specific antibodies against H4K16ac, H4K16pr, and H4K16bu are indispensable and at the beginning of this PhD project only antibodies against H4K16ac were commercially available. Therefore, for the generation of antibodies against H4K16pr or H4K16bu, 10 rabbits were immunized with the corresponding peptides. From the received sera samples, we purified specific antibodies. We managed to purify three antibodies against H4K16pr and one antibody against H4K16bu. During the preparation of this thesis, antibodies against H4K16pr and H4K16bu became commercially available and were included in experiments performed at later stages. We tested antibodies on peptide immunoblots onto which differently modified H4K16 peptides were titrated (Fig. 2.16A). Antibodies against H4K16ac, that were commercially available, are shown in Fig. 3.16B/C. We decided to work further with H4K16 #285 since it showed less cross-specificity against other acylations. In contrast, H4K16 #332 also recognized H4K16pr. In total, four different antibodies against H4K16pr were used during the thesis (Fig. 3.16D-G). Antibodies H4K16pr #1, #4, and #69 were purified from sera while the H4K16pr #Thermo antibody was purchased. Our purified antibodies seemed to preferentially recognize H4K16pr while the H4K16pr #Thermo antibody showed high cross-reactivity towards H4K16bu and slightly towards H4K16ac. For the detection of H4K16pr, antibody #69 was used if not mentioned otherwise. The H4K16bu #104 antibody was purified from serum and preferentially recognized H4K16bu (Fig. 3.16H).

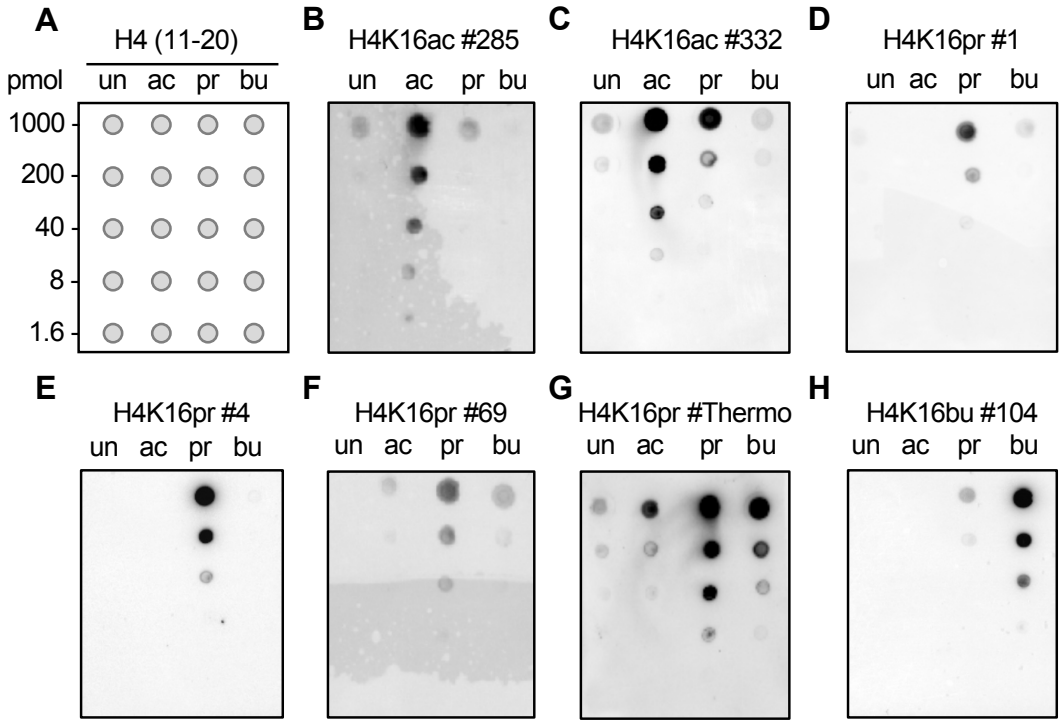

Figure 3.16: H4K16 acylation-specific antibody. A Illustration of a dot blot with serial dilution of H4 peptides (aa 11- 20) with lysine 16 being unmodified (un), acetylated (ac), propionylated (pr), or butyrylated (bu). Decreasing amount of indicated peptides was spotted on a nitrocellulose membrane. Antibodies against H4K16ac (**B**, **C**), H4K16pr (**D**-**G**), and H4K16bu (**H**) were used for immuno-dot blots and cross-specificity towards other H4K16 acylations was observed.

3.4.2. Nuclear distribution of H4K16 acylations

With our set of antibodies, we wanted to check the distributions for the different acylations in the nucleus. We first imaged mouse embryonic fibroblasts (MEFs) and observed a similar distribution of all H4K16 acylations (Fig. 3.17). Only H4K16bu seemed to localize in brighter spots. The additional DAPI staining revealed an exclusion of H4K16 acylations from percicentric heterochromatin.

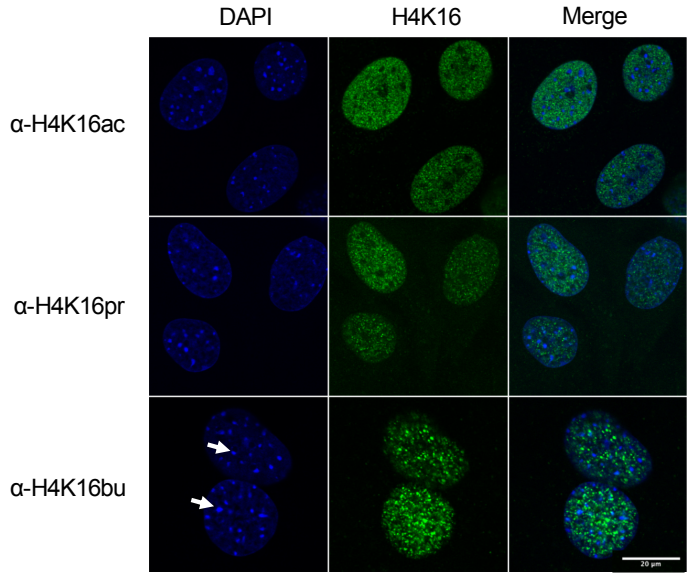

Figure 3.17: Nuclear distribution of H4K16 acylations. MEF cells were stained with acylation-specific antibodies and DAPI. Pericentric heterochromatin regions are highlighted with arrows. Scale bar: 20 µm.

In addition, we teamed up with the lab of Prof. Geiger (direct help: Dr. Amanda Amoah, Universität Ulm, DE) to study the potential polar distributions of H4K16 acylations and their changes in human hematopoietic stem cells (HSC) received from young and old donors (Florian *et al*, 2012). We considered H4K16 acylations as polarized when an asymmetric distribution was obvious and we further highlighted the asymmetry by adding a white line across the nucleus (Fig. 3.18). In comparison to H4K16ac, H4K16bu did not distribute asymmetrically and no apparent changes upon aging were observed. HK16pr, on the other hand, seemed to resemble the localization and polarity of H4K16ac in young and old HSCs but unfortunately, the H4K16pr antibody did not perform consistently during this imaging approach and no further replicates could be included.

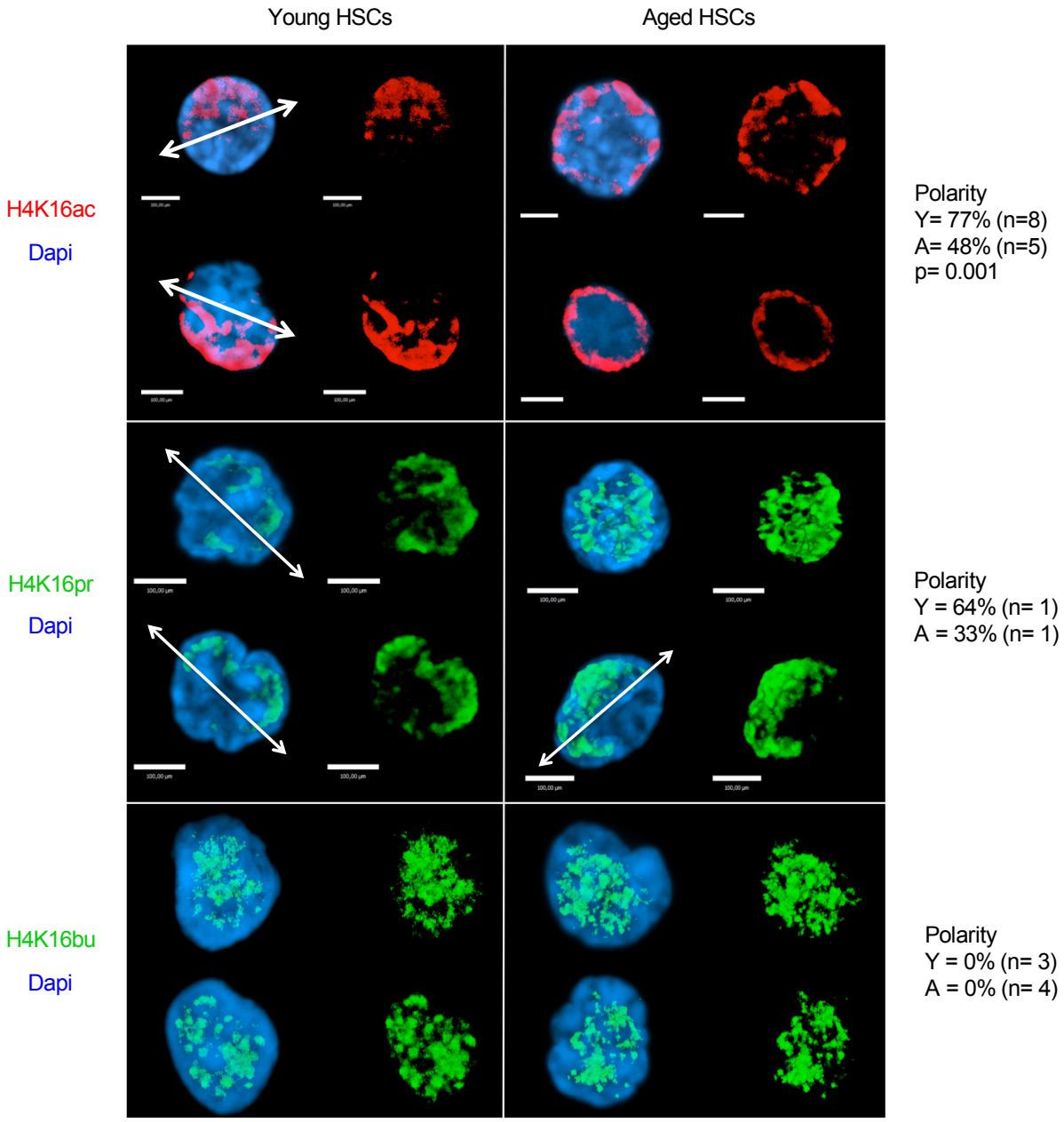

Figure 3.18: H4K16 acylation-specific polarity in HSCs. Representative distribution of H4K16ac (red, upper panel), H4K16pr (green, middle panel) and H4K16bu (green, lower panel) in young (left) and aged (right) human hematopoietic stem cells (HSCs). Nuclei are stained with DAPI (blue). On the right, polarity percentages for different acylations in young and aged HSCs are listed. White arrows indicate polarity axis. Bar = 100 µm.

3.4.3. Genome-wide mapping of acylated H4K16: Method establishment

Next, we studied the genomic distribution of the different histone acylations. We first wanted to establish a working ChIP protocol for the H4K16ac antibody #285 alongside a control antibody against H3K9ac. During this establishment phase, we used HEK293 (human embryonic kidney) cells as well as MEFs (mouse embryonic fibroblasts) and tried different ChIP approaches (Fig. 3.19).

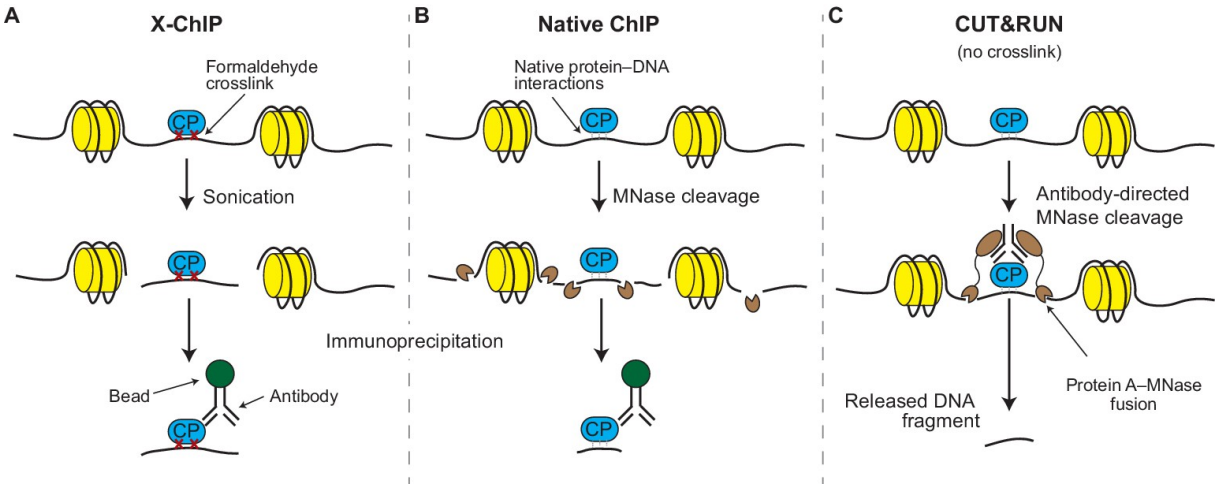

Figure 3.19: Overview of different ChIP approaches. A Crosslinked (X-) ChIP starts with crosslinking cells or tissues with formaldehyde to preserve interactions between DNA and interacting chromatin-binding protein of interest (CP in blue). Chromatin is mainly sheared into smaller fragments by sonication but can also be fragmented by MNase digestion (X-MNase ChIP). **B** Native (N-) ChIP depends on a high affinity between DNA and interacting proteins. Chromatin is released by fragmentation via MNase (brown). **C** In the recently established CUT&RUN (Cleavage Under Targets and Release Using Nuclease) approach, antibodies targeting CPs can recruit the Protein A-MNase (brown structure) which will cut the DNA in close proximity. During CUT&RUN targeted DNA fragments are directly released. In X- and N-ChIP approaches, antibodies recognizing the CP are only added after chromatin fragmentation (He & Bonasio, 2017).

We started with a standard cross-linking ChIP (X-ChIP) setup during which chromatin is sheared by sonication. Via qPCR we checked two active gene regions (*ACTB*, *RPL10*) as well as two inactive gene regions (*MYOD1*, gene desert; Fig. 3.20A). As expected, H3K9ac was enriched over input only in the active regions. H4K16ac was barely enriched over input and did not seem to be enriched in active or inactive gene regions. In general, the enrichment over input seemed too low and that is why we decided to try another ChIP protocol during which we fragmented the chromatin extracted from crosslinked HEK293 cells via MNase digestion (Fig. 3.20B). The overall detected signal was higher than for the previous X-ChIP approach but H3K9ac was only enriched at the *ACTB* promoter. H4K16ac signals seemed to be increased in *ACTB*, *RPL10,* and also at the promoter region of the inactive gene *MYOD1*. Neither H3K9ac nor H4K16ac were enriched in the gene desert region. Keeping in mind the low abundance of non-acetyl H4K16 acylations (Simithy *et al*, 2017), we continued testing other protocols to

observe a higher enrichment for H4K16ac. Next, we tried a native ChIP (N-ChIP) approach and detected the highest signals for H3K9ac and H4K16ac in comparison to the other ChIP approaches. But also the "background" level detected in inactive gene regions was higher (Fig. 3.20C). We next tried the CUT&RUN (Cleavage Under Targets and Release Using Nuclease) protocol on MEF cells and were able to detect mono-nucleosomes after library preparation for H3K9ac and H4K16ac (Fig. 3.21). We included our purified antibodies against H4K16pr and H4K16bu and were also able to detect a peak for mono-nucleosomes. After next-generation sequencing (NGS), we could not detect an enrichment of H4K16ac and H4K16pr around TSSs (Fig. 3.22A) and we were only able to detect an enrichment for H3K9ac and H4K16bu at TSSs (Fig. 3.22B).

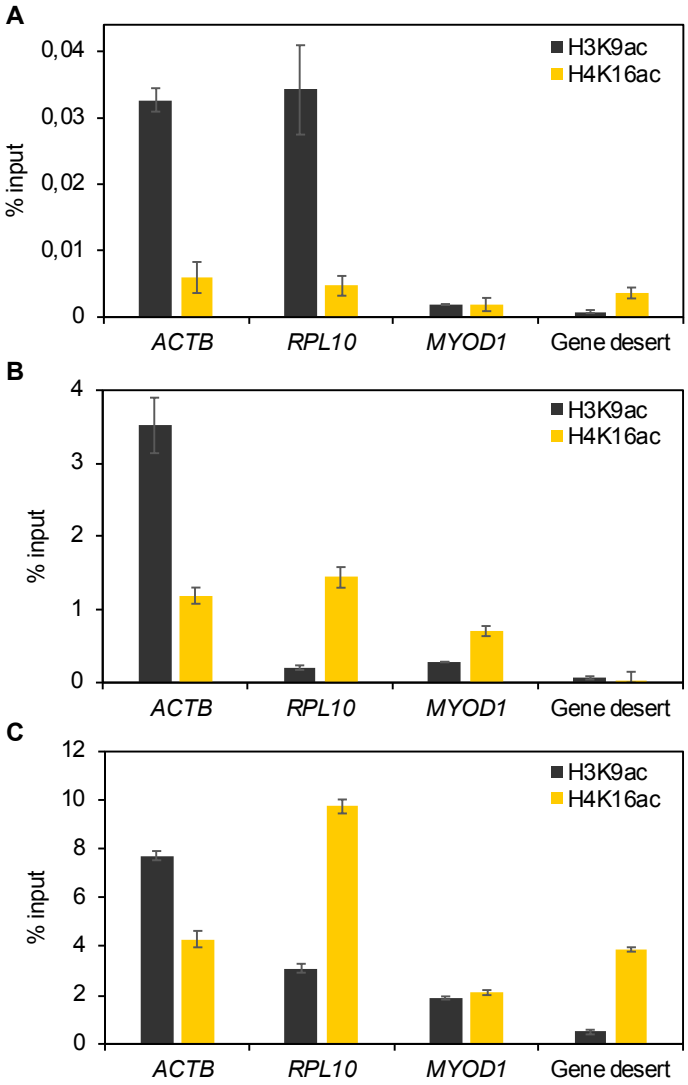

Figure 3.20: ChIP approach establishment. Crosslinked (X-) ChIP (**A**), X-MNase ChIP (**B**) and native (N-) ChIP (**C**) approaches were tested on HEK293 cells. The H3K9ac antibody (black) was used as a positive control to compare the ChIP efficiency of the H4K16ac (yellow) antibody. The enrichment was calculated as the percentage of input (y-axis). Two promoter regions of active genes (*ACTB*, *RPL10*) and two inactive regions (*MYOD1*, Gene desert) analyzed. Average of two technical replicates and STD is shown.

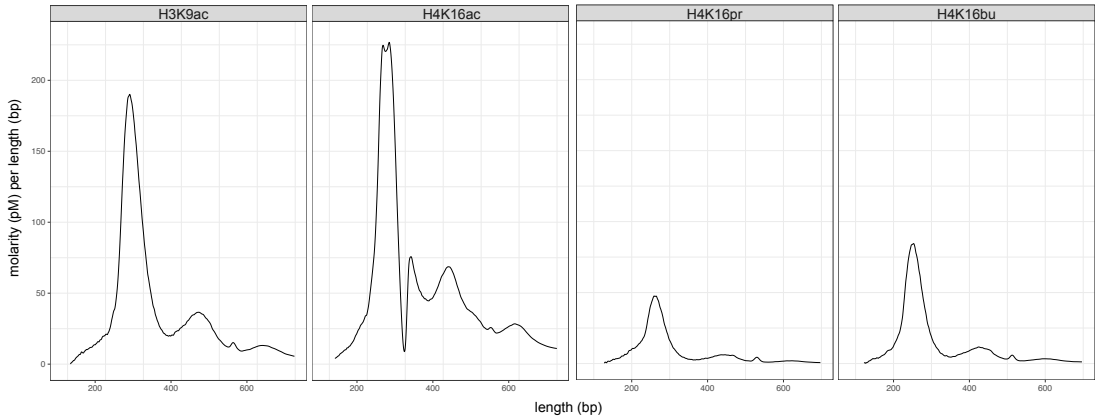

Figure 3.21: CUT&RUN nucleosomal ladder. The released nucleosomal ladder DNA after CUT&RUN and library preparation for NGS is shown. Libraries for H3K9ac, H4K16ac, H4K16pr and H4K16bu CUT&RUN samples were analyzed on a Bioanalyzer high sensitivity DNA chip. Shown are Bioanalyzer plots for each CUT&RUN using different antibodies. The molarity (in pM) per length (in basepairs; bp) is plotted on the y-axis while the x-axis is the fragment length in bp.

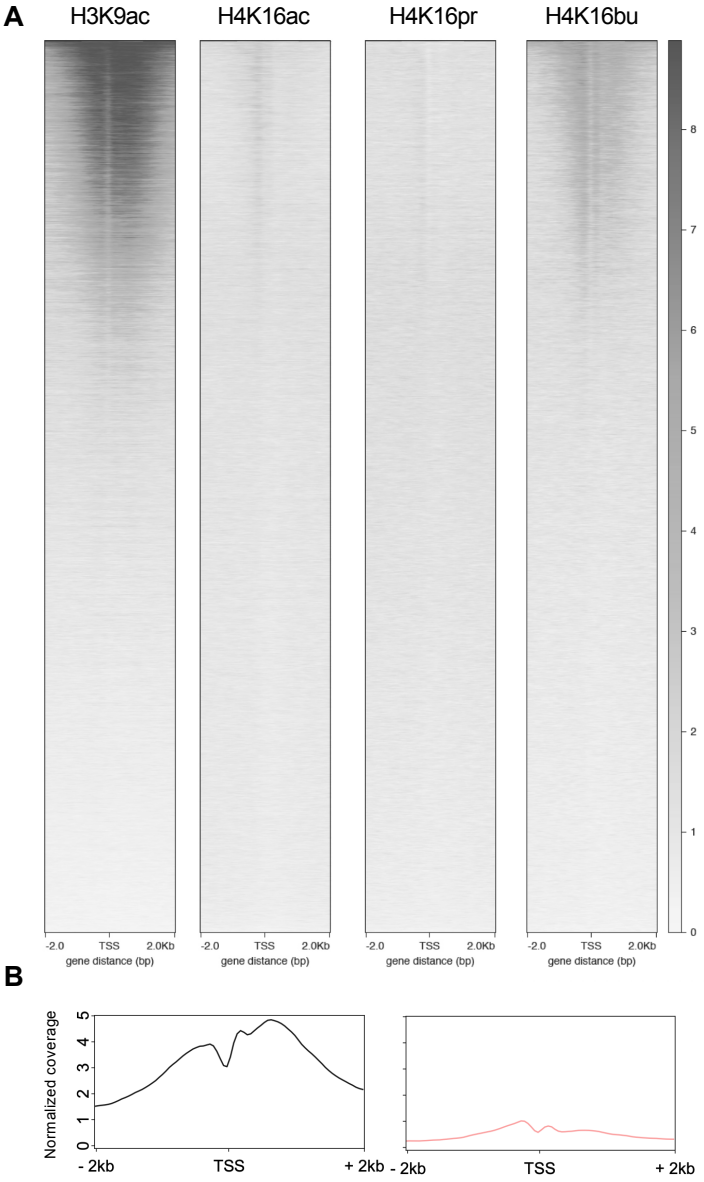

Figure 3.22: CUT&RUN sequencing results. A Profile heatmaps of sequences CUT&RUN samples using H3K9ac, H4K16ac, H4K16pr and H4K16bu antibodies. Peaks were aligned to the TSS (± 2 kb). **B** TSS profiles for H3K9ac (black, left) and H4K16bu (coral pink, right). The normalized coverage is plotted on the y-axis for ± 2 kb around TSSs (x-axis).

3.4.4. H4K16 acylations correlate with gene expression in mESCs

At this point, we wondered if the detection of the H4K16 acylations would be more efficient in cells with more open chromatin. Thus, we decided to use mESCs (mouse embryonic stem cells) in combination with the N-ChIP approach which previously resulted in the highest enrichment over input (Fig. 3.20C).

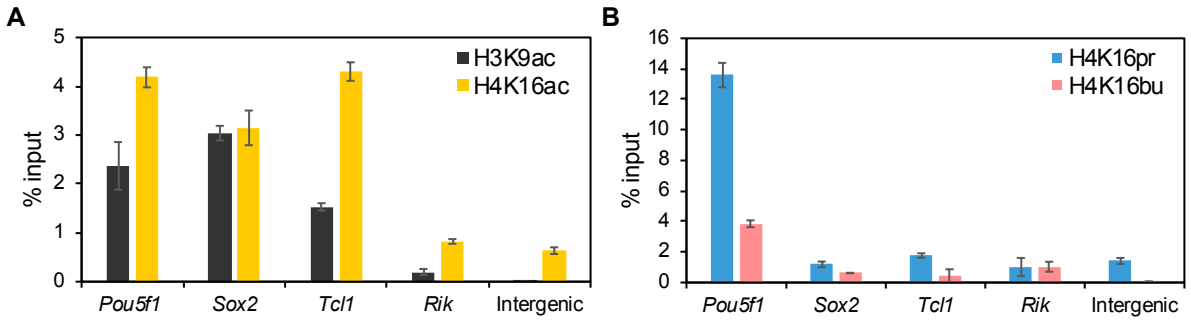

Figure 3.23: Native ChIP was performed on mESCs. The H3K9ac antibody (black) was used as a positive control. Antibodies against H4K16ac (yellow, **A**), H4K16pr (blue), and H4K16bu (coral pink) were also used (**B**). The enrichment was calculated as % input (y-axis). Three promoter regions of active genomic regions (*Pou5f1, Sox2, Tcl1*) and two inactive genomic regions (*Rik*, intergenic) were analyzed. Average of two technical replicates and STD is shown.

As shown in Fig. 3.23A, we detected an enrichment for H3K9ac and H4K16ac in active genomic regions (*Pou5f1, Sox2, Tcl1*) via qPCR. In inactive genomic regions H3K9ac and H4K16ac remained low. High enrichment for H4K16pr and H4K16bu was only detected at *Pou5f1* whereas the signals detected at the remaining regions remained similarly low (Fig. 3.23B). We used this sample set for NGS and from the overview provided in Fig. 3.24, all acylations seemed to localize to active genomic regions. The signal for H4K16 acylations was lower than the one detected for H3K9ac but nevertheless enriched at similar active genomic regions as well as reduced at inactive genomic regions (Fig. 3.25 and 3.26).

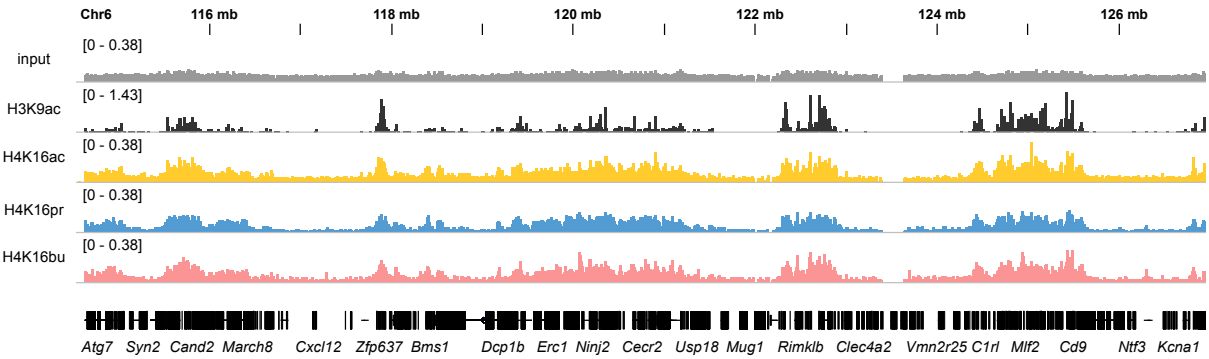

Figure 3.24: Overview of genomic distribution of histone acylations in mESCs. A representative snapshot from the Integrative Genomics Viewer (IGV) browser with ChIP-seq tracks showing the normalized coverage. In comparison to input (grey), H3K9ac (black), H4K16ac (yellow), H4K16pr (blue), and H4K16bu (coral pink) were enriched in the same genomic regions (gene track below).

We then analyzed the distribution of these acylations genome-wide. The distribution at different genomic sites is summarized in Fig. 3.27. Approximately 20 % of H3K9ac peaks were localized

in the TSS and the promoter region. Also, around 20 % of H4K16 acetylations appeared in these regions whereas other H4K16 acylations were less abundant. H4K16pr was mainly detected in intronic regions whereas H4K16bu seemed to localize in intergenic regions.

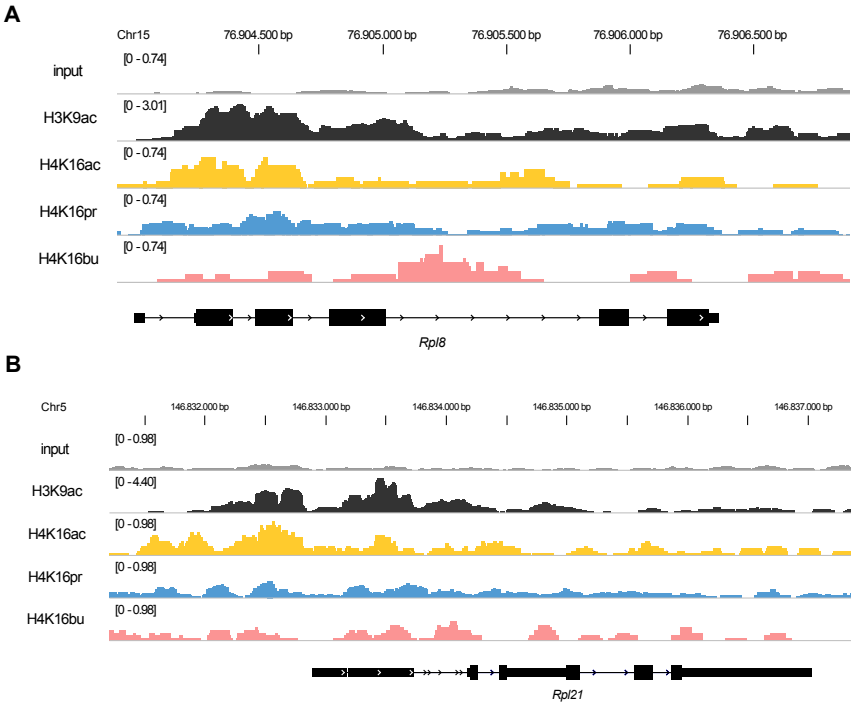

Figure 3.25: Representative active genomic regions in mESCs. Snapshots from IGV browser with ChIP-seq tracks showing the normalized coverage. In representative active genomic regions like *Rpl8* (**A**) or *Rpl21* (**B**) H3K9ac (black), H4K16ac (yellow), H4K16pr (blue), and H4K16bu (coral pink) are enriched over input (grey). H3K9ac had the highest enrichment in comparison to H4K16 acylations.

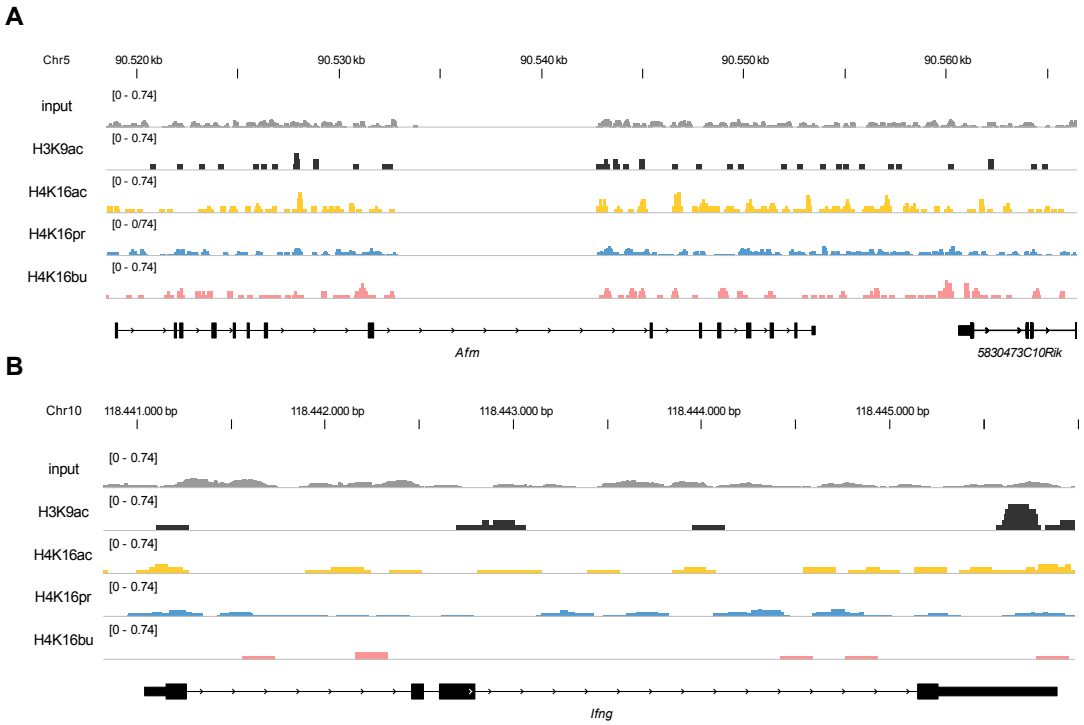

Figure 3.26: Representative inactive genomic regions in mESCs. Snapshots from the IGV browser with ChIP-seq tracks showing the normalized coverage. In representative inactive genomic regions like *Afm* (**A**) or *Ifng* (**B**) H3K9ac (black), H4K16ac (yellow), H4K16pr (blue), and H4K16bu (coral pink) are at the level of the input (grey).

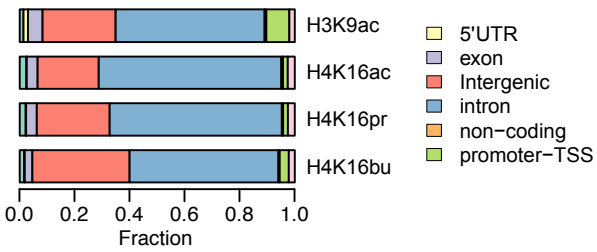

Figure 3.27: H4K16 acylation distribution in mESCs. Shown is the genomic distribution of annotated peaks for different histone acylations. After peak calling, peaks were annotated to different genomic regions. Shown annotations are: TSS (-1kb to +100bp), non-coding, intronic, intergenic, exon (coding), and 5' UTR exon regions.

We further included publicly available RNA-seq data (Shahidian *et al*, 2021) and analyzed if acylation levels increased at TSS (± 5 kb) with increasing gene expression as observed for H3K9ac (Fig. 3.28A). The enrichment for H4K16 acylations around TSSs was lower than for H3K9ac but we were still able to correlate the level of H4K16 acylations to the degree of gene expression (Fig. 2.28B).

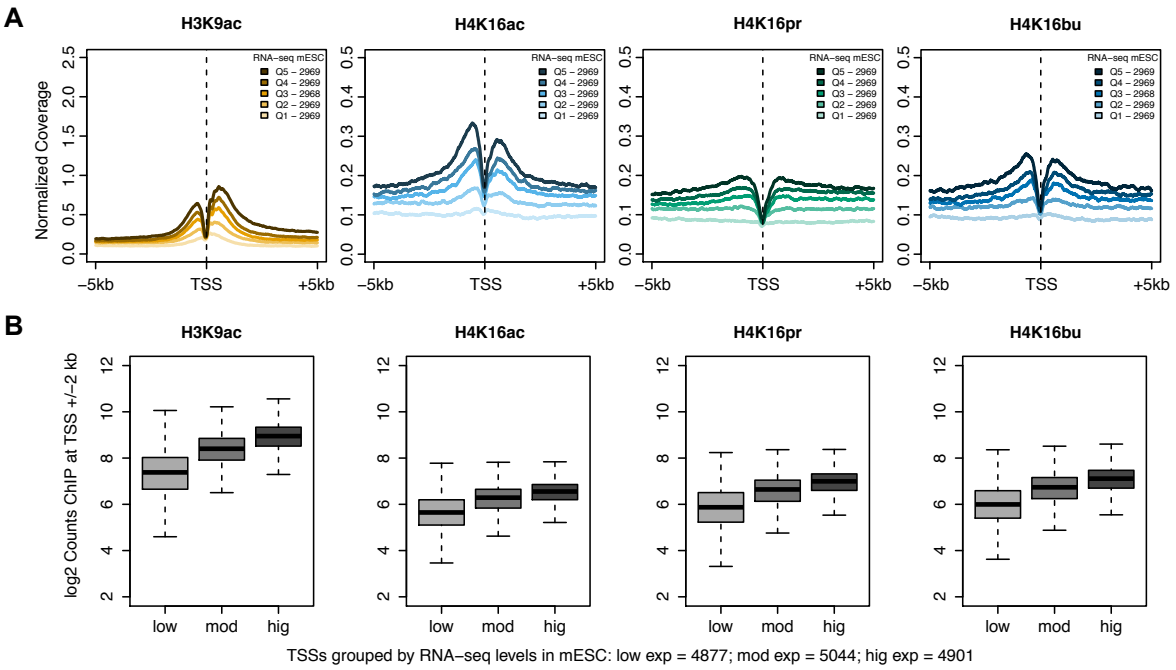

Figure 3.28: H4K16 acylation correlates to gene expression in mESCs. A Mean values for normalized coverage of H3K9ac (yellow), H4K16ac (light blue) and H4K16pr (green), and H4K16bu (dark blue) are plotted around the TSSs (± 5 kb) according to their quantile (Q5-Q1) of expression. **B** In these box plots, median values for log_2 counts of H3K9ac, H4K16ac, H4K16pr, and H4K16bu around the TSS (± 2 kb) are plotted. Gene numbers for lowly expressed (low), moderately (mod), and highly (hig) expressed are indicated below plots.

Since we managed to establish a working ChIP protocol, we decided to further focus on tissue samples derived from high-fat diet mice and metabolic deficient mice. We made this decision based on the following questions: Are metabolic fluctuations due to a specific diet or a disease reflected on the epigenome and does this interconnection have a direct effect on gene expression?

3.5. Metabolic challenges and their effect on H4K16 acylations

To investigate potential links between metabolism and epigenetic modifications and how the metabolic state of a cell could be integrated into the epigenome, we received liver samples from high-fat diet mice and mice models for metabolic disorders. We specifically chose to focus on the liver since it is a metabolically important and homogenous organ consisting of 70 to 80 % of hepatocytes (Sohlenius-Sternbeck, 2006).

3.5.1. Metabolomics: Acyl-CoA quantifications

We teamed up with Dr. Michael Witting (HMGU, München, DE) in order to detect and quantify various acyl-CoAs. For trial measurements, we used mouse embryonic fibroblasts (MEFs). As shown in Fig. 3.29A, we were able to detect acetyl-CoA, propionyl-CoA, and butyryl-CoA from total cell extracts. We then continued with the acyl-CoA quantification using liver samples from HF and chow diet mice. Interestingly, we detected an increase of acetyl-CoA after HFD but a decrease for propionyl-CoA and butyryl-CoA (Fig. 3.29B).

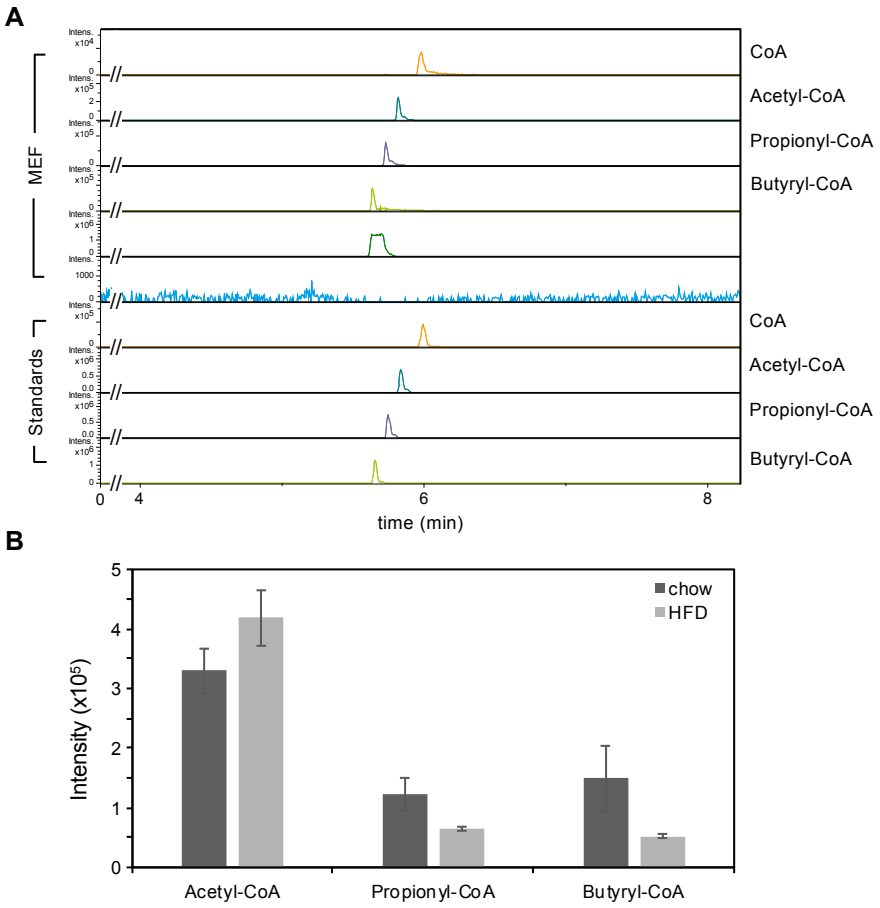

Figure 3.29: Acyl-CoA quantification from cell and tissue samples. A Mass chromatograms of identified peaks during the measurements of MEF samples and standards for different acyl-CoAs (free CoA, acetyl-CoA, propionyl-CoA, butyryl-CoA). Plotted are the measured intensities over time. Metabolites were extracted from whole cell lysates. **B** Acyl-CoAs were also measured in liver samples from HFD and chow-treated mice (n=2). Plotted are the average of the measured signal intensities from two different livers and the STD.

3.5.2. Genomic distribution of histone acylations in livers from HFD mice

We wondered next if these fluctuations of acyl-CoA concentrations upon HFD could be detected on the histone acylation levels. We planned to perform ChIP-seq on these liver samples to study the genomic distribution of histone acylations and potential changes in their levels upon different diets. We first checked via ChIP-qPCR if our N-ChIP protocol could also be used on tissue samples. As shown in Fig. 3.30, we could overall detect an increase for all acylations in active genomic regions (*Gapdh*, *Hprt*, *Pck1*), whereas inactive genomic regions (*Rik*, *Trim63*, Intergenic) did not seem to be acylated. The H4K16pr and H4K16bu were also enriched in the *Gapdh* and *Hprt* promoter although their enrichment was in general lower than H4K16ac (Fig. 3.30B).

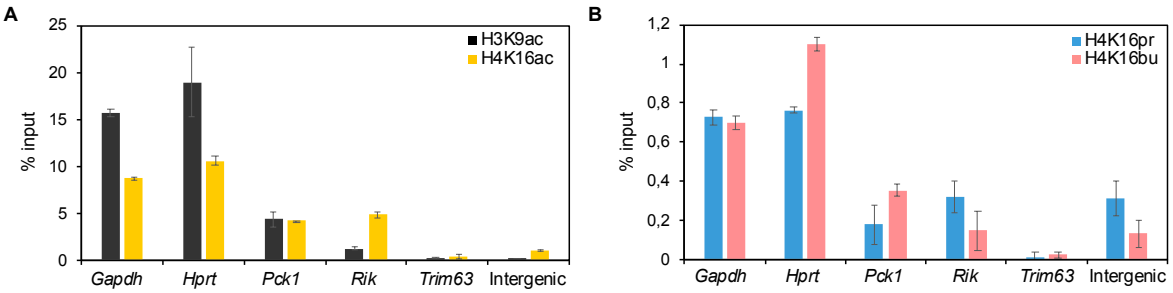

Figure 3.30: N-ChIP-qPCR on WT mouse livers. Antibodies against H3K9ac, H4K16ac (**A**), H4K16pr, and H4K16bu (**B**) were used for the IP of chromatin from mouse livers. The H3K9ac antibody (black) was used as a positive control. The enrichment was calculated as % input (y-axis). Three promoter regions of active genes (*Pou5f1*, *Sox2*, *Tcl1*) and two inactive regions (*Rik*, intergenic) were analyzed. Average of two technical replicates and STD is shown.

After validating that we can detect our marks of interest in tissue samples via ChIP, we prepared liver samples from HF and chow diet mice for a ChIP-seq experiment. Unfortunately, the ChIPs with our H4K16pr antibody did not result in any enrichment over background and thus no data for H4K16pr can be shown in the following results. First, we started by browsing broader genomic loci to get an overview of the enrichment for all the acylations. As highlighted in Fig. 3.31, all acylations were enriched at similar locations. The detected enrichment of H3K9ac was again the highest in comparison to H4K16ac or H4K16bu signals.

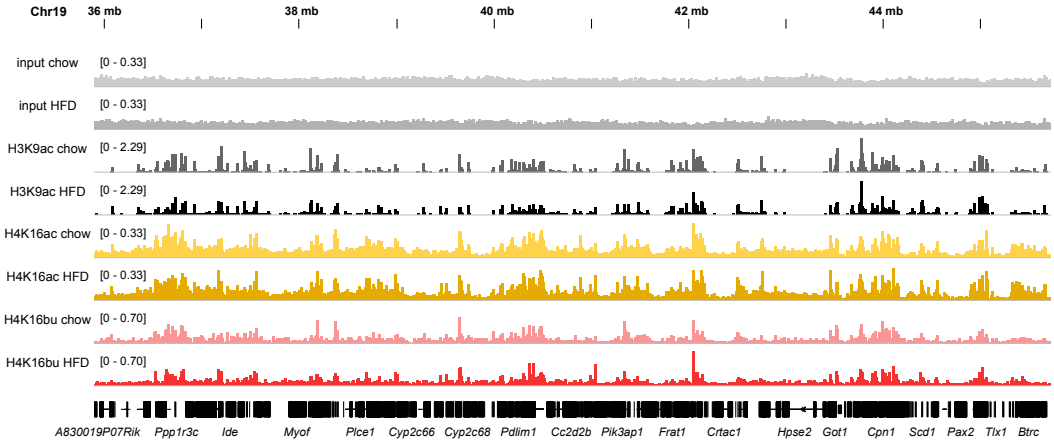

Figure 3.31: Genomic distribution of histone acylations in livers from HFD mice. Shown is a snapshot from the IGV browser. The normalized coverage is indicated for all acylations. In contrast to the inputs (light grey), enriched signals at the same genomic regions are visible for the positive control H3K9ac (dark grey), H4K16ac (yellow), and H4K16bu (red) for livers from HF and chow diet treated mice.

We then took a closer look at this data set to identify regions in which H4K16 acylations behaved differently. In addition, we wondered if diet-induced changes in acyl-CoA levels (Fig. 3.29B) were reflected in H4K16ac and H4K16bu levels. As shown in Fig. 3.32A, we found regions in which H3K9ac and H4K16ac levels seemed to increase upon HFD. But we also observed regions in which H3K9ac and H4K16ac signals decreased upon HFD (Fig. 3.32B).

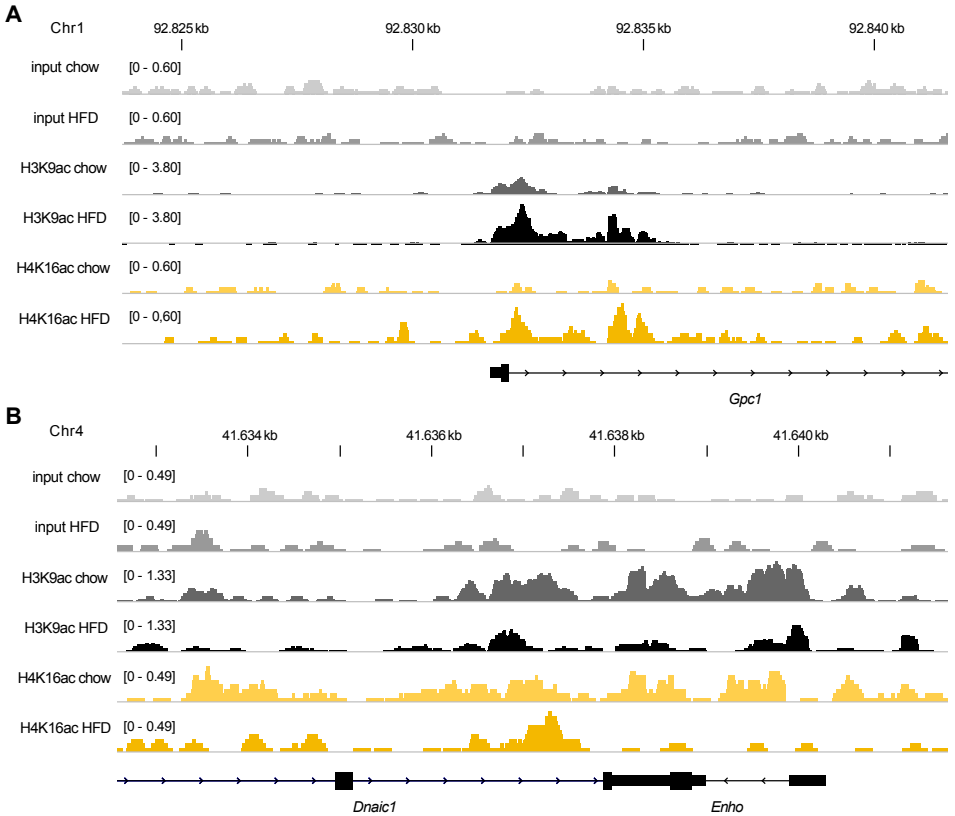

Figure 3.32: Representative gene regions in which Kac changes upon HFD. Shown is a snapshot from the IGV browser in which the normalized coverage is indicated for all acylations. Inputs are shown in light grey. **A** H3K9ac (dark grey) and H4K16ac (yellow) increased upon HFD in the *Gpc1* gene region. **B** H3K9ac and H4K16ac decreased upon HFD in the *Enho* gene region.

We then checked if H4K16bu behaves similarly. And indeed, we were able to identify regions in which H4K16bu increased upon HFD (Fig. 3.33A). Interestingly, we also identified regions, in which H4K16bu decreased upon HFD but H4K16ac seemed to increase (Fig. 3.33B).

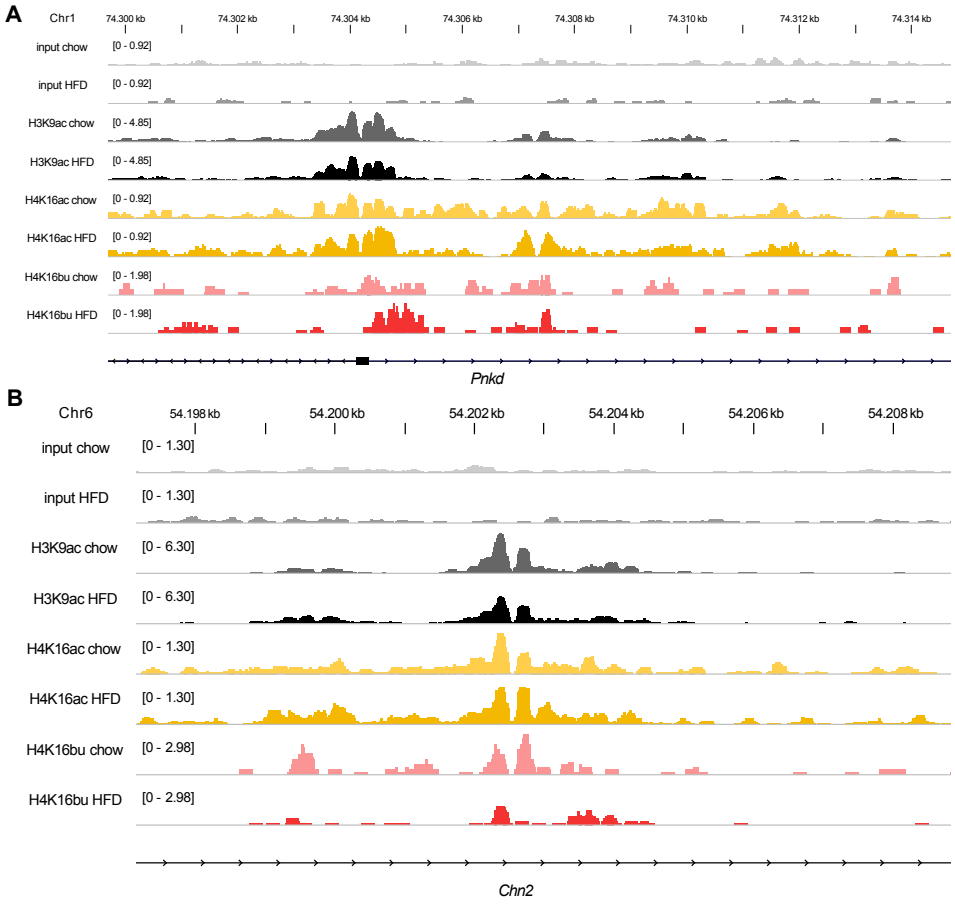

Figure 3.33: Representative gene regions in which Kbu changes upon HFD. Shown is a snapshot from the IGV browser in which the normalized coverage is indicated for all acylations. Inputs are shown in light grey. **A** H4K16ac (yellow), and H4K16bu (red) increased upon HFD in the *Pnkd* gene region while H3K9ac (dark grey) seemed unaltered. **B** H4K16bu decreased upon HFD in the *Chn2* gene region. H3K9ac decreased to a lesser extent while H4K16ac seemed to increase.

We made use of a publicly available RNA-seq data set to check if our histone acylations correlate with gene expression in the different liver samples (Siersbæk *et al*, 2017). As shown in Fig. 3.34A, we observed an enrichment of H4K16ac and H4K16bu around TSSs depending on the expression quantiles (Q1<Q5). H4K16bu seemed to be more enriched downstream of the TSS in comparison to H4K16ac. We analyzed the changes of these marks in non-, moderately, and highly expressed genes and we were again able to observe a correlation between H4K16 acylations and gene expression (Fig. 3.34B). Interestingly, upon chow-diet H4K16bu counts were higher for highly expressed genes than H4K16ac while upon HFD, H4K16ac and H4K16bu levels were more similar.

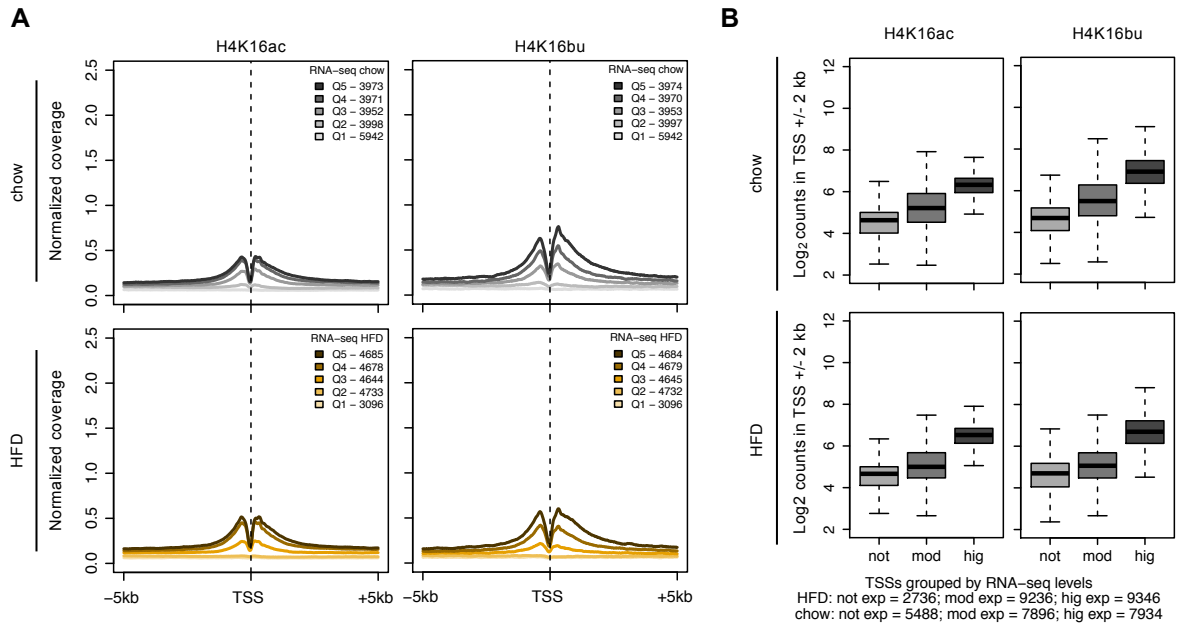

Figure 3.34: Histone acylations correlate with gene expression in HFD livers. A Mean values for normalized coverage of H4K16ac (left) and H4K16bu (right) are plotted around the TSS (± 5 kb) according to their quantile (Q5-Q1) of expression for livers from HF (yellow) and chow-diet (grey) mice. **B** Median values for log_2 counts of H4K16ac and H4K16bu around the TSS (± 2 kb) for livers from HF and chow diet mice are plotted. Gene numbers for not expressed (not), moderately (mod), and highly (hig) expressed are indicated below plots.

At this point, we wanted to check how histone acylations change for the different diets and thus we compared their enrichment in genes that were up- or downregulated upon chow or high-fat diet. Unfortunately, we were not able to detect general trends for H4K16ac or H4K16bu levels upon diet (data not shown). We also checked the top significant genes for which acylation level changes were observed upon HFD but we were not able to make any conclusions based on the gene list (data not shown). We also tried to perform a gene ontology enrichment analysis to again check if different pathways might be affected by diet-induced changes in acylation levels but unfortunately, no significant hits were observed (data not shown).

Nevertheless, we have shown, that we were able to correlate H4K16ac and H4K16bu to gene expression and that we observed higher H4K16bu enrichment in higher expressed genes both in livers from high-fat and chow-diet mice. Our main aim was to prove our hypothesis that dietary changes can affect histone acylations levels. Probably due to the complex effect of HFD on metabolism and potential secondary metabolic effects, we were not able to unravel an obvious link between the previously described acyl-CoA fluctuations upon HFD and the genomic distribution and enrichment of histone acylations.

3.5.3. Metabolic disorders affect H4K16 acylations

We realized due to our experience on working with dietary changes in mice, that diets have a complex effect on metabolism which made it hard for us to conclude how metabolic information is integrated into the epigenome. This is why we then decided to study the following metabolic disorders: propionic acidemia (PA) and short-chain specific acyl-CoA dehydrogenase (SCAD) deficiency. We made this decision based on the fact that metabolic changes for both deficiencies are well studied and propionyl-CoA and butyryl-CoA levels are known to increase (Pougovkina *et al*, 2014). Mouse models for both disorders exist and we were able to receive liver samples from exactly those mice. Prof. Lourdes Ruiz Desviat's team (CSIC-UAM, Madrid, ES) provided us with liver samples from propionyl-CoA carboxylase alpha (Pcca) deficient mice while Dr. Sander Houten (ISMMS, New York, US) sent us livers from *Acads*$^{-/-}$ mice.

To check if this enrichment of the specific acyl-CoAs is reflected in the epigenome, we first extracted histones from these liver samples. As demonstrated in Fig. 3.35, we were able to detect an increase of H4K16pr and H3K14pr upon PCCA deficiency. H4K16bu seemed to increase while H4K16ac and H3K14bu did not increase compared to WT samples (Fig. 3.35). We detected an increase of H4K16ac upon SCAD deficiency whereas the other acylations seemed comparable to WT samples. To get a deeper insight into the general histone acylome, we also quantified histone acylations via MS (direct help: Dr. Andrey Tvardovskiy, HMGU, München, DE). As shown in Fig. 3.36, we were able to detect an increase of propionylation at various histone lysines in liver samples from PCCA-deficient mice compared to WT. Interestingly, we also observed a slight loss of histone acetylations. Unfortunately, due to technical limitations, we were not able to detect histone butyrylation via MS, and therefore no data of samples derived from *Acads*$^{-/-}$ mice can be shown.

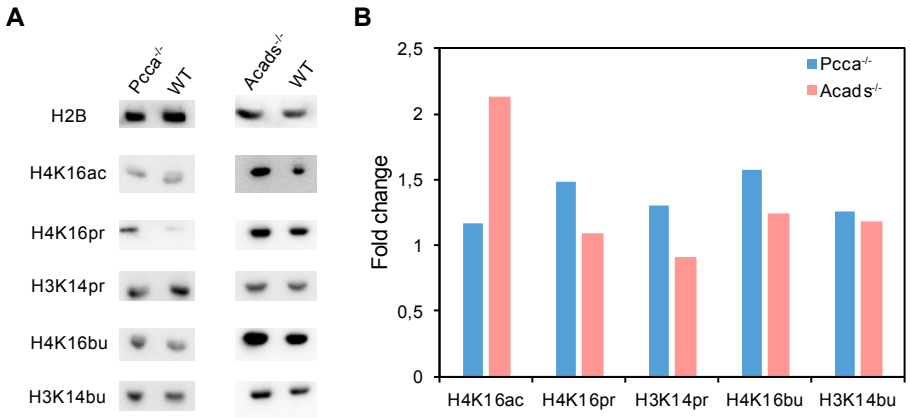

Figure 3.35: Histone acylation changes in metabolic disorders. A Histone acylation changes were observed on extracted histones derived from *Pcca*$^{-/-}$ or *Acads*$^{-/-}$ and compared to WT samples via western blot. H2B was used as a loading control. **B** Fold change of quantified signal from Pcca$^{-/-}$ (blue) or Acads$^{-/-}$ (coral pink) histones over WT samples is plotted for the different histone acylations. Fold change was calculated from 2 biological replicates.

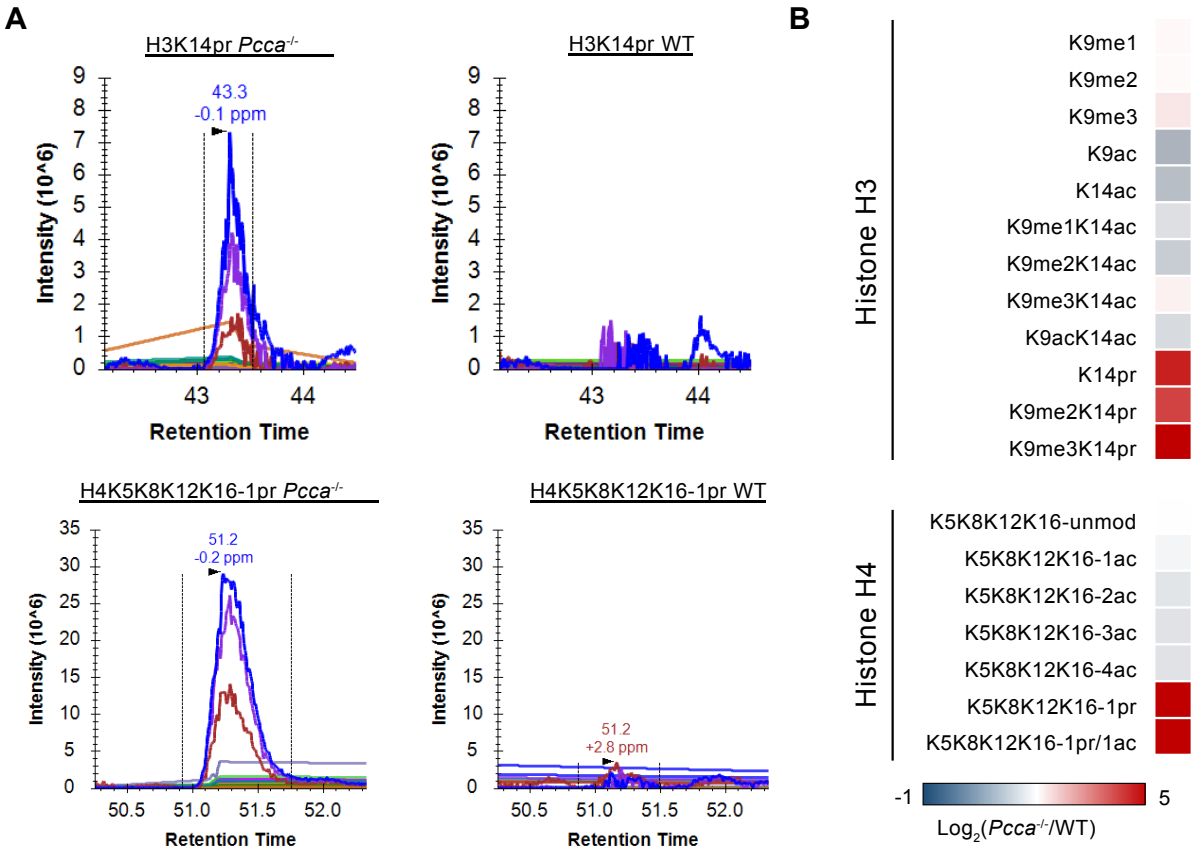

Figure 3.36: Quantification of histone acylation changes upon PA. A Histones were extracted from liver samples and quantified via MS. Shown here are mass chromatograms of identified peaks for H3K14pr and H4K5K8K12K16-1pr during the measurements from *Pcca*$^{-/-}$ and WT livers. Plotted is the signal intensity against the retention time. **B** Quantification of detected histone acylations and methylations (me) at different lysine sites in H3 and H4. The degree of $\log_2$ fold changes is indicated in the color key legend.

Next, we asked if we can detect these changes via ChIP-qPCRs as well. We again used our N-ChIP approach which we established before (Fig. 3.37). Here, we only show one active (*Gapdh*) and one inactive (*MyoD1*) genomic region. We again used H3K9ac as our positive control for which we detected an enrichment in the active genomic region but not in the inactive one with mild changes between livers from deficient mice in comparison to WT. H4K16ac was also enriched in the active genomic region in comparison to the inactive one and a decrease upon the PCCA deficiency was observed. At this point during the project, we were able to include different antibodies against H4K16pr. We included the antibodies that we purified as previously described (H4K16pr #1, #4, and #69) for this ChIP round. We were able to detect a strong increase of H4K16pr upon the deficiency in the *Gapdh* promoter region (Fig. 3.37A) with all the three antibodies. In comparison to the other two H4K16pr antibodies, antibody #4 gave us the lowest enrichment. Surprisingly, we also observed an increased enrichment in H4K16pr in the inactive genomic region (Fig. 3.37B).

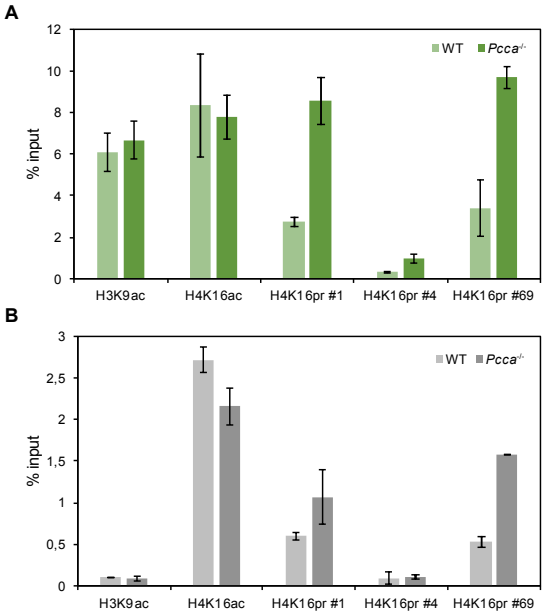

Figure 3.37: H4K16pr enrichment in promoter regions upon PA. In these ChIP-qPCR results, the percentage of input is shown for different histone acylations (H3K9ac, H4K16ac, H4K16pr) in an active genomic region (**A**, *Gapdh*) and an inactive one (**B**, *MyoD1*). Average of two technical replicates and the STD is shown.

After these promising indications, we continued to prepare samples for ChIP-seq and RNA-seq since no data set for gene expression changes in livers upon PCCA deficiency was available. Via the RNA-seq, we did not observe major global changes in the gene expression in livers from deficient mice in comparison to WT livers. As shown in the MA plot in Fig. 3.38, for most of the genes no significant change was detected. Still, some genes were significantly upregulated respectively downregulated in the livers derived from deficient mice.

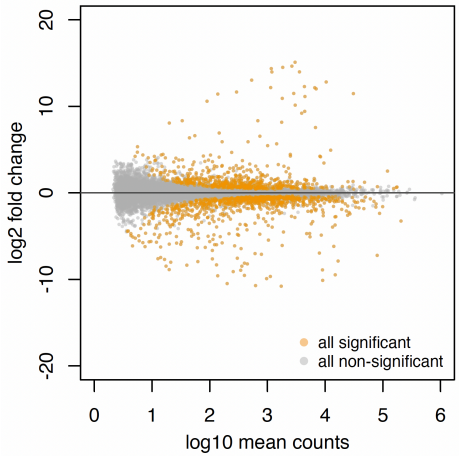

Figure 3.38: Gene expression changes upon PA. In this MA-plot expressed genes are represented by a dot. The $\log_2$ fold change of expression between livers from *Pcca*$^{-/-}$ and WT mice is plotted against the $\log_{10}$ mean counts. Grey dot: non-significantly changed gene. Yellow dot: significantly changed gene.

Next, we used our ChIP-seq data to first broadly "browse" different gene regions to check if in general, our ChIP approach worked. As shown in the overview in Fig. 3.39, we observed a similar signal enrichment for H3K9ac, H4K16ac, H4K16pr, and H4K16bu in active genomic loci. The H4K16ac and the H4K16bu signals were less enriched in comparison to the other marks and in general, a higher signal background was detected for H4K16ac.

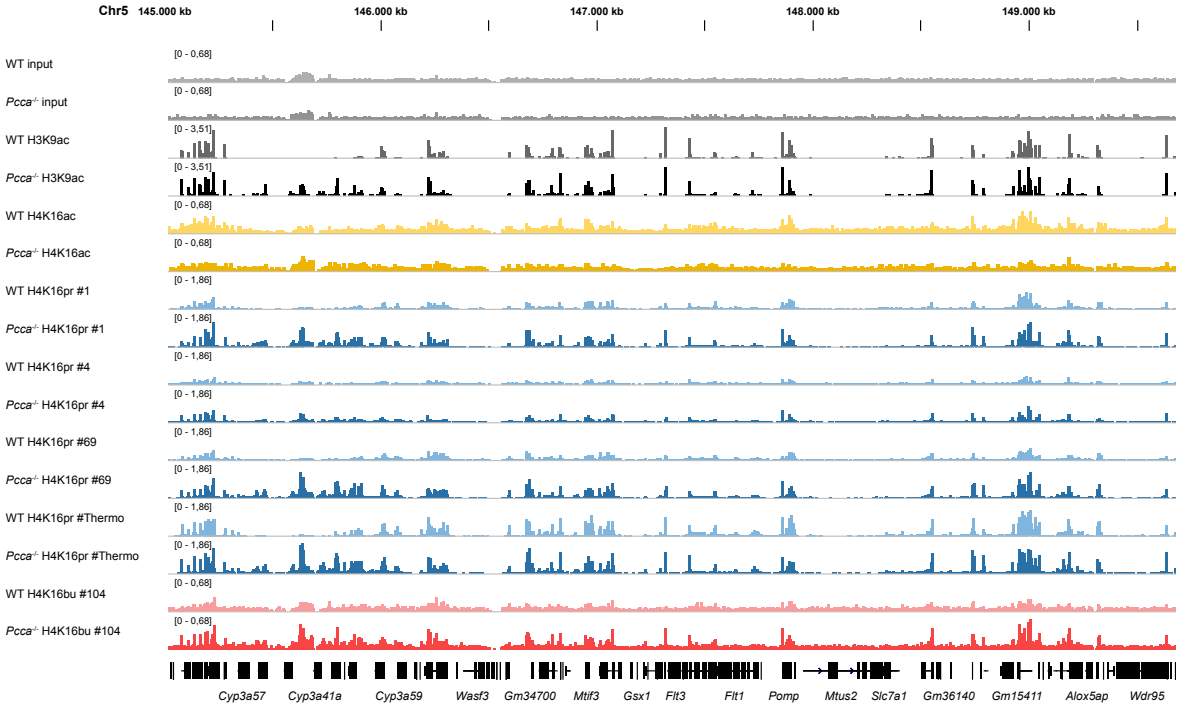

Figure 3.39: Genomic distribution of histone acylations in livers from *Pcca-/-* and WT mice. Shown is a snapshot from the IGV browser in which the normalized coverage for different histone acylations is indicated. In contrast to the inputs (light grey), enriched signals at the same genomic loci are visible for the positive control H3K9ac (dark grey), H4K16ac (yellow), H4K16pr (blue), and H4K16bu (red).

We further focused on active genomic loci and provide one example in Fig. 3.40 in which we took a closer look at the *Smoc1* gene region. We were able to observe an H4K16pr increasement upstream and downstream of *Smoc1*. Intriguingly, the detected H3K9ac signals did not seem to follow this trend but rather stayed the same. For H4K16ac we were able to see a decreased enrichment in the samples from PCCA-deficient mice. Another example is shown in Fig. 3.41 for the *Lama3* and *Ttc39c* gene regions in which we observed a loss of H3K9ac, H4K16pr, and H4K16bu in samples derived from deficient mice. For H4K16ac such a reduction was not as obvious because of the low enrichment and a rather noisy signal.

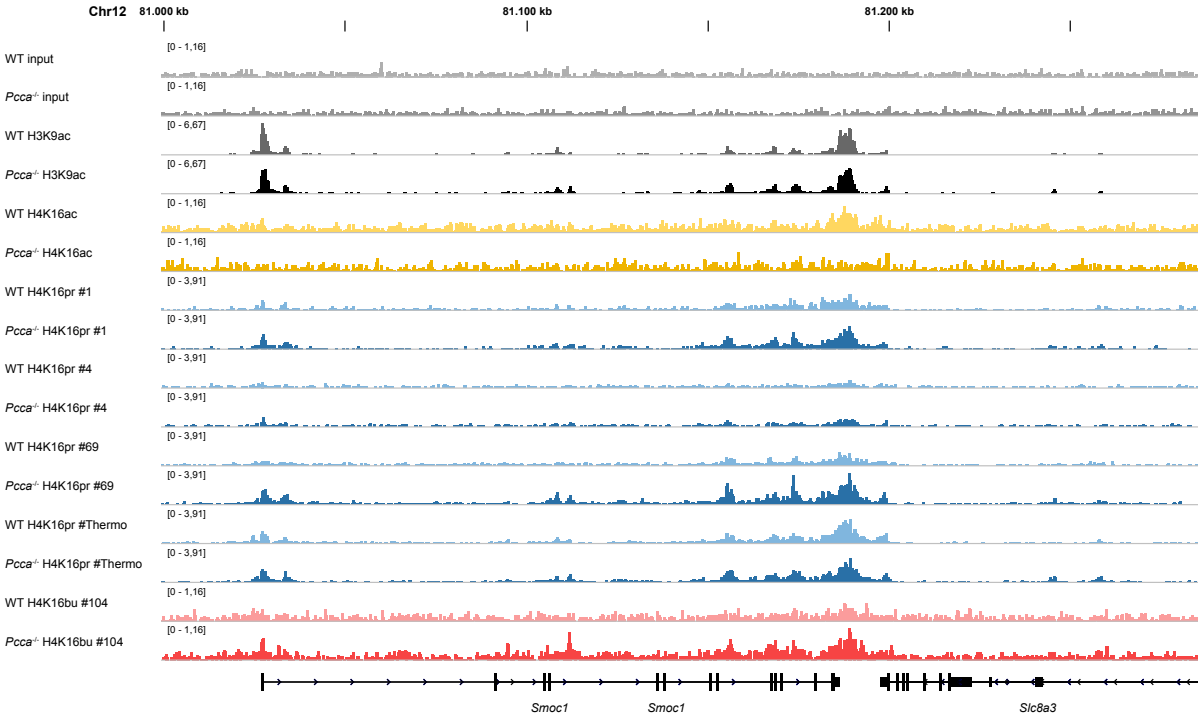

Figure 3.40: Increased H4K16pr enrichment upon PA. Shown is a snapshot from the IGV browser in which the normalized coverage for different histone acylations is indicated. The input tracks are indicated in light grey. H4K16pr (blue tracks) was enriched upon PCCA deficiency while H3K9ac (dark grey) remained unchanged. H4K16ac (yellow) peaks seemed decreased. H4K16bu (red) levels also increased but to a lesser extent than H4K16pr.

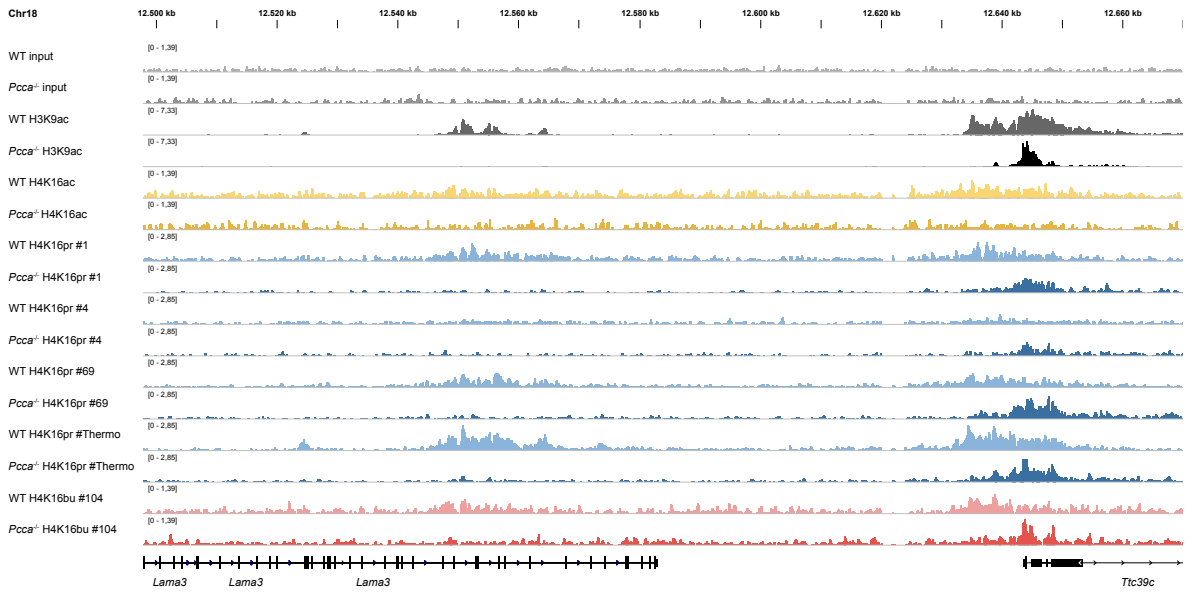

Figure 3.41: Decreased H4K16pr enrichment upon PA. Shown is a snapshot from the IGV browser in which the normalized coverage for different histone acylations is indicated. The input tracks are shown in light grey. H3K9ac (dark grey) and H4K16pr (blue tracks) were decreased upon PCCA deficiency while the effect on H4K16ac (yellow tracks) and H4K16bu (red tracks) was not as obvious.

We generated density plots in order to understand how in general H4K16 acylations levels changed upon PCCA deficiency (Fig. 3.42). In the density plots, the log_2 normalized counts between 4 to 6 correspond to background values while higher counts (above 6) correspond to highly marked TSSs. We observed a shift towards the higher counts only for H4K16pr upon PCCA deficiency (yellow vs grey curve, Fig. 3.46B-D) indicating that H4K16pr levels increased. In contrast, H4K16ac counts decreased upon PCCA deficiency (Fig. 3.46A). We did not include data generated by the antibodies H4K16pr #Thermo and H4K16bu #104 due to the lack of a second replicate.

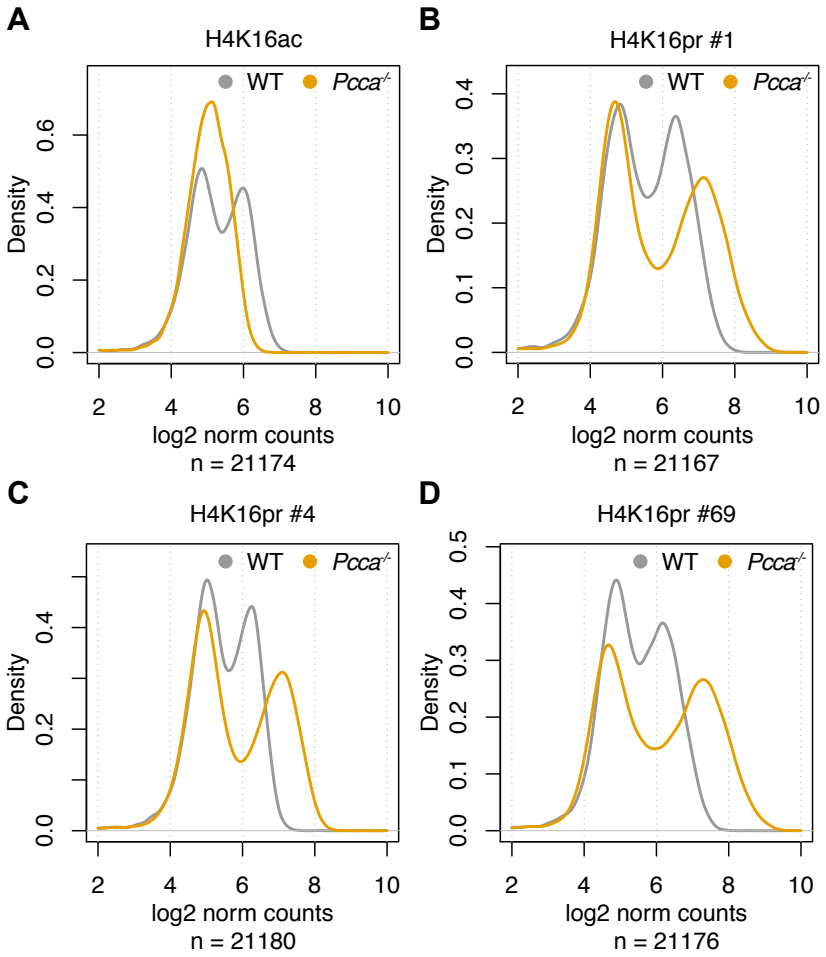

Figure 3.42: General increased H4K16pr enrichment upon PA. Density plots show the distribution of ChIP-seq signals for H4K16ac (**A**) and H4K16pr (**B-D**) in WT (grey) and *Pcca*$^{-/-}$ (yellow) livers. The reads were counted in a 4 kb window surrounding TSSs. The counts were normalized to the genome-wide background and were log_2 transformed. The x-axis indicates these log_2 normalized counts while the y-axis shows the density of TSSs. Counts between 4 to 6 correspond to background values while higher counts (above 6) correspond to highly marked TSSs.

We then wanted to understand how the different acylations correlate with gene expression. We generated enrichment profiles around TSSs for differently expressed genes. In Fig. 3.43, these profiles are shown for H3K9ac, H4K16ac, and H4K16bu. We were able to observe a general increased enrichment for all the three acylations with increasing gene expression. Overall, the enrichment for our positive control H3K9ac was the highest and appeared not to change upon PCCA deficiency. In WT samples, H4K16ac was slightly more enriched with increasing gene expression than H4K16bu. Excitingly, H4K16ac signals decreased in livers from deficient mice. In contrast, H4K16bu signals increased. In both cases, the detected signal still correlated with gene expression.

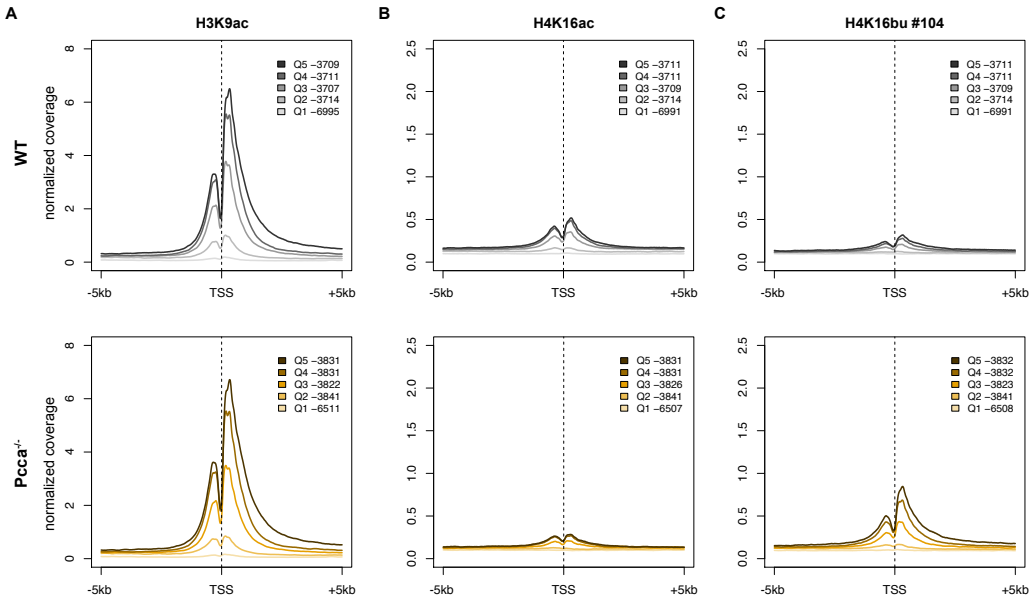

Figure 3.43: Histone acylations correlate with gene expression. Mean values for normalized coverage (y-axis) of H3K9ac (**A**), H4K16ac (**B**), and H4K16bu (**C**) are plotted around the TSS (± 5 kb, x-axis) according to its quantile of expression (Q5-Q1) for livers from WT (grey) and deficient (yellow) mice.

The TSS profiles for H4K16pr are summarized in Fig. 3.44 and we were able to detect a correlation between these acylations and gene expression. Remarkably, we observed an increased H4K16pr enrichment upon PCCA deficiency. The signals detected from H4K16pr antibodies #1, #4, and #69 were comparable while signals from H4K16pr #Thermo were in general higher.

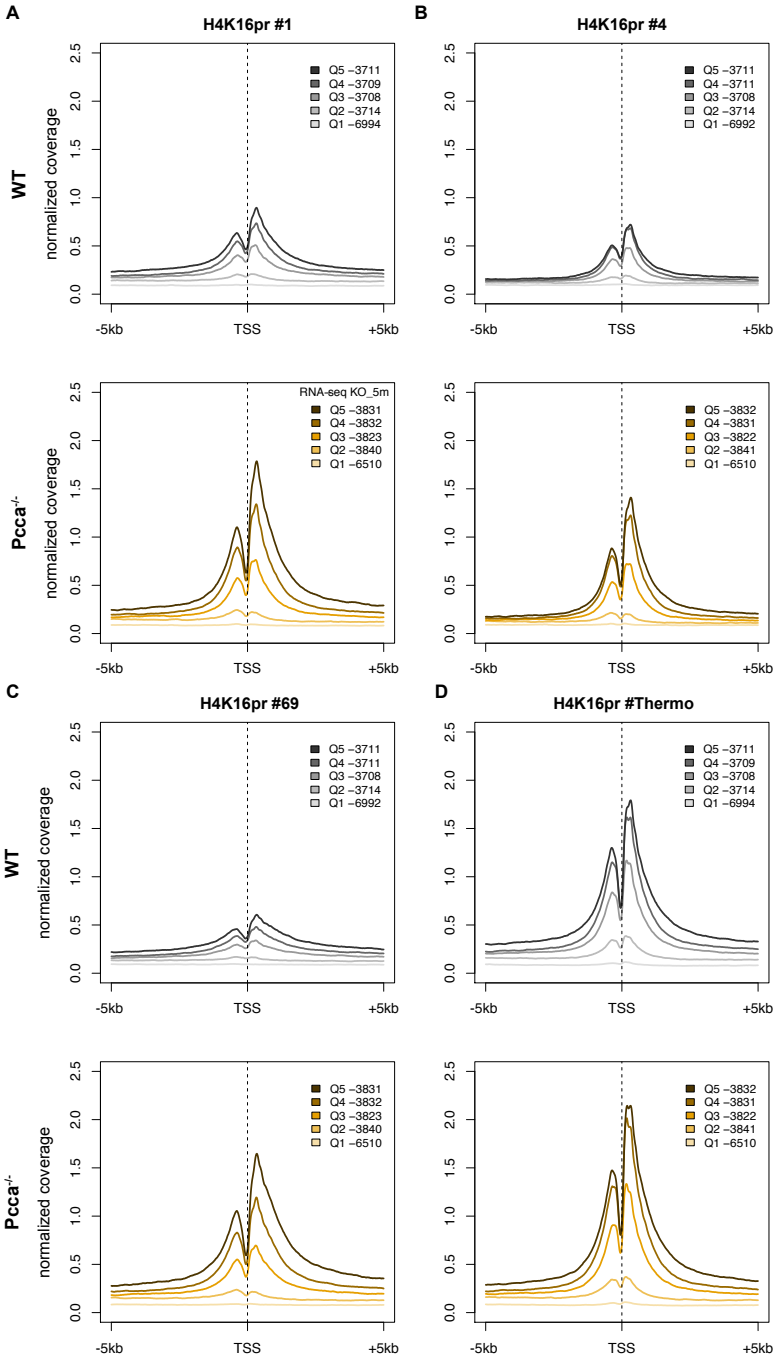

Figure 3.44: Histone propionylation correlates with gene expression. Mean values for normalized coverage (y-axis) of H4K16pr as detected by different antibodies: #1 (**A**), #4 (**B**), #69 (**C**), and #Thermo (**D**) are plotted around the TSS (± 5 kb, x-axis) according to its quantile of expression (Q5-Q1) for livers from WT (grey) and deficient (yellow) mice.

We analyzed the distribution of these acylations genome-wide. The distribution at different genomic sites for H3K9ac, H4K16ac, and H4K16bu is summarized in Fig. 3.45. We observed a clear enrichment for H3K9ac at 5'UTR exon, exon, non-coding and promoter-TSS region and this distribution pattern seemed similar for WT and *Pcca*$^{-/-}$ samples. The enrichment pattern for H4K16ac was not as obvious (Fig. 3.44A). We detected a slight enrichment at the 5'UTR exon

and exon region for H4K16ac in livers from PCCA-deficient mice (Fig. 3.45B). In comparison, the enrichment of H4K16bu at non-coding regions was higher in livers from PCCA-deficient mice than from WT samples while for other genomic sites (5'UTR exon, exon) only modest changes were observed (Fig. 3.45C).

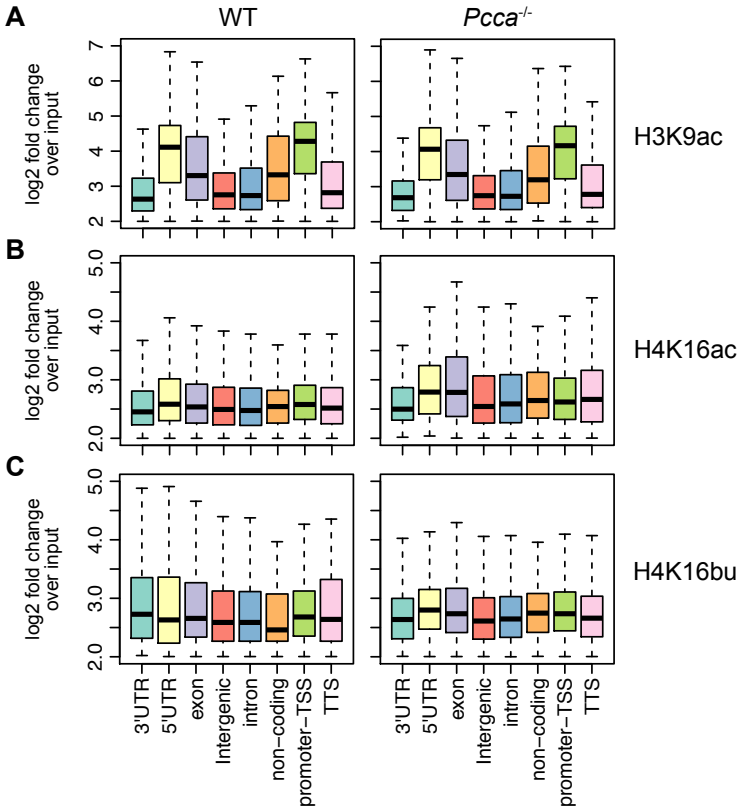

Figure 3.45: Peak intensities at genomic features for WT and *Pcca*$^{-/-}$ samples. After peak calling, H3K9ac (**A**), H4K16ac (**B**), and H4K16bu (**C**) peaks from WT (left) and *Pcca*$^{-/-}$ (right) samples were annotated to different genomic regions. Shown are the peak intensities (enrichment over input, y-axis) for each annotation category (x-axis). Shown annotations are: 3' UTR exon, 5' UTR exon, exon (coding), intergenic, intron, non-coding, promoter-TSS (-1kb to +100bp), and TTS (transcription termination site, -100 bp to +1kb) regions.

The distribution of H4K16pr in WT livers showed no clear enrichment but upon PCCA deficiency, we detected an enrichment of H4K16pr at the 5'UTR exon, exon, non-coding, and promoter-TSS regions (Fig. 3.46A-C). In contrast, a distinct distribution pattern at the same genomic sites was observed for H4K16pr signals detected by the H4K16pr #Thermo in WT as well as PCCA-deficient livers with no obvious changes upon the deficiency (Fig. 3.46D).

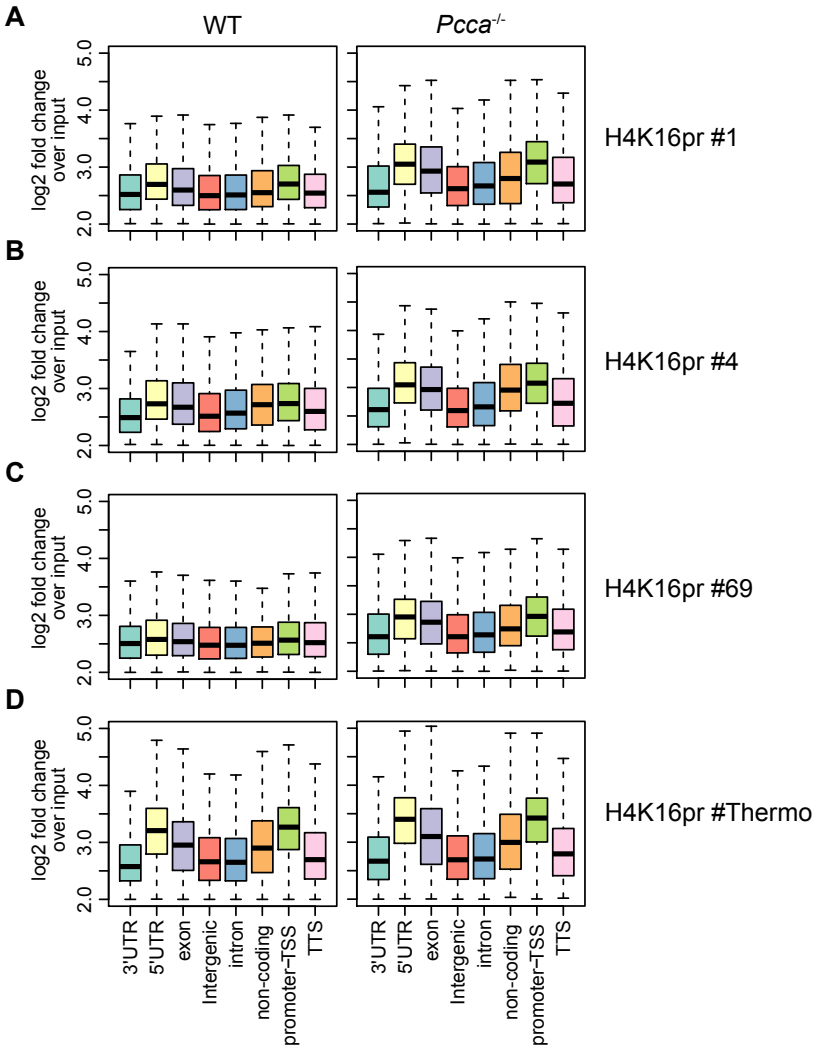

Figure 3.46: Altered H4K16pr peak intensities at genomic features upon PA. After peak calling, H4K16pr peaks (from different antibodies **A**: #1, **B**: #4, **C**: #69, **D**: #Thermo) from WT (left) and *Pcca*$^{-/-}$ (right) samples were annotated to different genomic regions. Shown are the peak intensities (enrichment over input, y-axis) for each annotation category (x-axis). Shown annotations are: 3' UTR exon, 5' UTR exon, exon (coding), intergenic, intron, non-coding, promoter-TSS (-1kb to +100bp), and TTS (transcription termination site, -100 bp to +1kb) regions.

Here we showed, how metabolic diseases can shape the epigenome. We observed a stronger influence on histone acylations upon PA than upon SCAD deficiency. We further showed that an increase of propionyl-CoA was reflected in general histone Kpr levels. More specifically we detected a drastic enrichment of H4K16pr at various genomic loci.

4. Discussion

In 2007, the first non-acetyl short-chain lysine acylations on histones were discovered (Kpr and Kbu) and since then additional novel acylations were revealed (Chen *et al*, 2007). The latest member of the acylation family (Kla) was only added two years ago (Zhang *et al*, 2019). With now 11 different lysine acylations multiple open questions circle around their function. How different are these acylations from each other and especially how do they behave in comparison to the most abundant acylation Kac? And further, do these acylations have their own distinct function, or do they rather act as an entity in which their different ratios contribute to a specific outcome? During this PhD thesis, we wanted to unravel the role of H4K16 short-chain acylations and address their biological role. In addition, we aimed to get a deeper insight into the relationship between epigenetics and metabolism and tried to answer some of the open questions raised above.

4.1. Generation of designer chromatin

For studying chromatin dynamics *in vitro*, we generated site-specific and fully acylated human histone H4 via the native chemical ligation (NCL). We fused a synthetic H4 tail peptide (1-28 aa) containing unmodified or acylated K16 to a truncated H4 (H4Δ1-28) (Fig. 3.3). A requirement for the site-specific ligation approach, is an N-terminal cysteine which we introduced at position 29 of the truncated H4. Our ligated, full-length H4, therefore, has a site mutation at this position (cysteine instead of isoleucine). Since the relevant regions of the H4 tail, which are involved in chromatin compaction and accessibility, are G14-R19 as well as R17-R23, we did not expect the introduced site mutation to have a major structural nor functional impact on the H4 tail (Dorigo *et al*, 2003; Chen *et al*, 2017). Nevertheless, for future studies, such point mutations can be avoided by using different strategies for the production of acylated histones. For example, the amber (stop) codon suppression method can be used for the integration of acylated lysine via an orthogonal acetyl-lysyl-tRNA synthetase (AcKRS)/ tRNA pair but from previous experience in our lab the yield for Kpr or Kbu containing histones was too low for subsequent *in vitro* studies (Neumann *et al*, 2008). An elegant but rather cost-intensive alternative is to completely chemically synthesize acylated histones (Shahidian *et al*, 2021). However, our studies depended on a larger amount of histones so this approach was not optimal for us. In addition, for the generation of designer chromatin, we mainly used DNA templates that were based on the Widom 601 sequence, which is an artificial nucleosome positioning sequence with a high histone-affinity, used for the majority of chromatin related *in vitro* studies (Spakman *et al*, 2020). With the successful generation of acylated designer

chromatin we were able to explore the impact of H4K16 acylations on chromatin architecture in more detail (Fig. 3.5 and Fig. 3.7).

4.2. H4K16 acylations can fine-tune chromatin dynamics

Via our internucleosomal interaction measurements using mono-nucleosomes and the DNA origami force spectrometer, we revealed that unmodified H4 had the highest interaction strength while the weakest interaction strength was observed for H4K16ac (Fig. 3.6D). These results are in line with the original studies from Shogren-Knaak *et al* (2006) in which they showed that H4K16ac inhibits the formation of compact chromatin. In addition, our finding is supported by the work from Funke and colleagues who noticed a decreased interaction strength upon H4K16 acetylation in comparison to unmodified WT octamers using the same DNA origami-based force spectrometer (Funke *et al*, 2016). We now for the first time included H4K16pr and H4K16bu into this approach. Interestingly, we observed that with increasing hydrophobicity (Kac<Kpr<Kbu) the interaction strength decreased (Kac>Kpr>Kbu) (Fig. 3.6D). But can these observed interaction strengths between mono-nucleosomes also affect more complex chromatin structures? That is why we also studied how H4K16 acylations affect nucleosomal stacking using a 12-mer nucleosomal array which actually has a similar length like a small gene (~2000 bp). Using this approach, our experiment revealed again that in comparison to unmodified H4, all H4K16 acylations were able to limit nucleosomal stacking (Fig. 3.9). But if we then actually quantify the compaction strength of the arrays, it seemed like H4K16pr and H4K16bu were able to disrupt nucleosomal stacking more than H4K16ac, indicating a stronger interference with nucleosomal stacking (Kbu≈Kpr>Kac) (Fig. 3.9). In another study, Smestad *et al* (2020) also used 12-mer nucleosomal arrays and observed that lysine acylations with increasing chain-length also destabilized arrays stronger, supporting our findings. Even though the data from our internucleosomal interaction study (Fig. 3.6) and the nucleosomal stacking analysis (Fig. 3.9) go in the same direction, the degree of the effects from the acylations varies. A reason for that might lay in the nature of the assays we used. While the mono-nucleosomes were rather immovably incorporated into the DNA origami force spectrometer (Fig. 3.5A), the 12-mer nucleosomal arrays remained flexible during the measurements (Fig. 3.7A). A more dynamic setup could allow an improved interaction between the H4 tail and the acidic patch of neighboring nucleosomes. Follow-up studies based on the work from Collepardo-Guevara *et al* (2015) can help to clarify and to further unravel the effect of H4K16 acylations on chromatin dynamics. In general, chromatin simulation studies could help to understand how the H4 tail flexibility and internucleosomal interactions are shaped by various H4K16 acylations and how

this can affect higher-order chromatin formation (Collepardo-Guevara *et al*, 2015; Chen *et al*, 2017). Via computational models, the effect of various histone PTM combinations on nucleosome-nucleosome as well as DNA-histones interactions can be studied for broader genomic regions and might help to understand how chromatin function is defined and potentially predict different chromatin states (Lequieu *et al*, 2019). Here, we provided a first glimpse into how H4K16 acylations can affect chromatin architecture that can pave the way for in-depth studies *in silico*.

4.3. General acyltransferases and acylation-specific interactors

So far no acylation-specific writers or erasers have been detected and only "traditional" HATs and HDACs seem to be able to utilize different co-factors (acyl-CoAs) and substrates (acylated lysines). In an elegant study from the Garcia lab, a general preference of HATs towards acetyl-CoA over other acyl-CoAs was demonstrated *in vitro*. Nevertheless, for example, MOF was still able to use propionyl-CoA and butyryl-CoA as co-factors (Simithy *et al*, 2017). We wondered about the activity of MOF towards these acyl-CoAs *in cellulo* and therefore made use of a 4-OHT (4-hydroxytamoxifen) inducible *Mof* KO MEF cell line (Fig. 3.10A). We confirmed that MOF also catalyzes H4K16pr *in cellulo* (Han *et al*, 2018). For the first time, we were able to identify MOF as a histone butyryltransferase responsible for H4K16bu *in cellulo* (Fig. 3.10C). For an in-depth study of the activity of MOF towards different acyl-CoAs, the generation of an auxin-inducible degron (AID) cell line might be beneficial (Nishimura *et al*, 2009). The *Mof* KO via 4-OHT takes at least four days while the protein degradation via the AID system can be achieved within minutes and is also reversible which can be used for MOF kinetics studies *in cellulo* (Natsume *et al*, 2016).

In comparison to writers and erasers preferring acetyl-CoA respectively acetylated lysines, readers containing a YEATS or DPF (double PHD finger) domain were actually shown to have a higher binding activity towards Kcr than Kac (Andrews *et al*, 2016; Xiong *et al*, 2016). In order to identify potential H4K16 acylation-specific readers, we used H4 tail peptides, that were acylated or unmodified at lysine 16, for an affinity purification approach (Fig. 3.11). Our findings suggest that most of the identified proteins preferred binding to H4K16un and that the interactome of H4K16ac, H4K16pr, and H4K16bu seemed comparable (Fig. 3.12). Surprisingly, no expected Kac interactors like bromodomain (BD) containing proteins were significantly enriched for acylated H4K16. Further, no interactors representing protein complexes, that are known to interact with chromatin, could be identified. A potential reason might be the use of only the H4 peptide as a bait. Affinity purifications with octamers, mono-

nucleosomes, or di-nucleosomes might offer a better interaction platform. Another reason for the low abundance of expected epigenetic readers might be that H4K16 acylations on their own cannot efficiently recruit interactors. A study by Filippakopoulos *et al* (2012) highlighted that multiple Kac sites on the H4 tail are essential for the specific binding of BET (bromodomain and extraterminal domain) family members. That combinations of PTMs can lead to a stronger recruitment in comparison to a single PTM was further proved by Zippo and colleagues. By using mono-nucleosomes containing H3K9ac, H4K16ac, or both acetylated histones, they observed an increased BRD4 binding in the presence of both acetylations (Zippo *et al*, 2009). Another example is the enhanced BPTF (bromodomain PHD finger transcription factor) binding upon the co-existence of H3K4me3 (binding via PHD finger) and H4K16ac (binding via BD) on the same nucleosome (Ruthenburg et al, 2011).

What caught our attention was the identification of SIRT3 as an interactor for H4K16ac and H4K16pr but not for H4K16bu (Fig. 3.13). *In vitro* HDAC assays showed that SIRT3 is able to deacetylate H4K16 and can to a lesser extent debutyrylate H4K16 as well (Tanabe *et al*, 2018). No data on SIRT3 activity towards H4K16pr exists so far but due to its described activity, it seems likely that SIRT3 can also act as a depropionylase. Via the MS quantification, we could not identify which isoform of SIRT3 binds H4K16ac and H4K16pr (Fig. 3.13D). We were then able to identify the shorter isoform of SIRT3 as a predominant interactor of H4K16ac and H4K16pr by immunoblotting (Fig. 3.13E). It should be noted that the shorter isoform of SIRT3 is more abundant, so via immunoblotting, we might not be able to detect the longer isoform (Iwahara *et al*, 2012). Notably, it was shown that SIRT3 can not only get processed in the mitochondria but also in the nucleus and that the full-length and processed isoform are both active and can deacetylate H4K16 (Scher et al, 2007).

Taken together, on one hand, we demonstrated how epigenetic players like MOF seem to control various acylations equally despite their preference for Kac, while on the other hand acylation-specific SIRT3 binding highlights how different acylations might modulate interactions and define downstream events.

4.4. H4K16 acylations stimulate transcription to a different degree

With our findings on how H4K16 acylations can fine-tune internucleosomal interactions and nucleosomal stacking, we wondered how this might affect transcription. We made use of a well-established *in vitro* transcription (IVT) assay. Via this highly controllable tool, acetylations on the H3 and H4 tails have been proven to be transcriptionally stimulating (An *et al*, 2002). As a template for the transcription, we used successfully assembled circular chromatin containing

differently modified H4K16 octamers (Fig. 3.14C/D). In comparison to H4K16un, H4K16ac was able to stimulate transcription the most, followed by H4K16pr. Intriguingly, in our experiments, H4K16bu seemed to barely activate transcription compared to H4K16un (Fig. 3.15B). So even though H4K16bu was shown to decrease internucleosomal interaction (Fig. 3.6D) as well as nucleosomal stacking (Fig. 3.9D), it did not stimulate transcription in a similar way as H4K16ac and H4K16pr. In contrast, other IVT assays using propionyl-CoA or butyryl-CoA observed a transcriptional stimulation similar to acetyl-CoA (Kebede *et al*, 2017; Goudarzi *et al*, 2016). But such experimental setups lead to a general acylation of chromatin on various histone lysines while in our case we only introduced one site-specific acylation. Further, potential interactors like BD containing transcription factors (TFs) might prefer H4K16ac and H4K16pr over H4K16bu. This idea is supported by findings that various bromodomains are interacting less with acyl groups longer than three carbons (Flynn *et al*, 2015). The bromodomain of BRDT for example is unable to bind to H4K5bu suggesting a potentially similar trend upon H4K16bu (Goudarzi *et al*, 2016). A conclusive affinity quantification can help to unravel interaction partners and to explain an acylation-dependent transcriptional activity.

Taken together, our results suggest that with increasing acyl chain length on H4K16 the potential to stimulate transcription *in vitro* decreases. We speculate that an efficient assembly of the transcription preinitiation complex might depend on H4K16 acylations. In general, after these insights from our *in vitro* studies (section 3.1-3.3), we wondered about the biological relevance of H4K16 acylations.

4.5. Distinct nuclear localization of H4K16 acylations during aging

To study the biological role of H4K16 acylations, site-specific and acylation type-specific antibodies are essential. At the beginning of this project only antibodies against H4K16ac were commercially available (Fig. 3.16B/C). Therefore, we arranged the immunization of rabbits with H4K16pr and H4K16bu and affinity-purified antibodies against these PTMs from the different sera we received (Fig. 3.16D-I). We decided to further use only one antibody against H4K16ac #285 (Fig. 3.16B) since it showed less cross-reactivity and one against H4K16bu #104 (Fig. 3.16I). The antibody #69 against H4K16pr (Fig. 3.16F) was the first one we were able to purify and this is why it was mainly used while for later ChIP experiments we also included the other antibodies against H4K16pr (Fig. 16D/E/G/H). We then used this set of antibodies to examine the nuclear localization of the H4K16 acylations in cells. Using MEF cells, at a first glance the localization for all H4K16 acylations seemed comparable (Fig. 3.17).

But while H4K16ac and H4K16pr broadly and evenly stained the nucleus, H4K16bu seemed to accumulate in spots. Staining with DAPI further revealed an exclusion of H4K16 acylations from pericentric heterochromatin regions (Fig. 3.17, arrows). This is consistent with previous findings showing an exclusion of H4K16ac from heterochromatin in peripheral blood neutrophils confirming that H4K16ac mainly marks euchromatin (Urdinguio *et al*, 2019). In addition, the nuclear distribution of H4K16ac is known to be involved in the aging of hematopoietic stem cells (HSCs). HSCs guarantee for example a steady blood production throughout life but upon aging, these stem cells can lose their ability to asymmetrically divide which is necessary for maintaining their stem cell potential. Aged HSCs mainly divide symmetrically and differentiate in favor of myeloid over lymphoid lineage cells (Mejia-Ramirez & Florian, 2020). A hallmark of aged HSCs is among others the polarity loss of H4K16ac which seems to be a downstream effect of the apolar distribution and the increased activity of a RhoGTPase namely Cdc42 (cell division control protein 42) (Florian *et al*, 2012). An epigenetic polarity or so-called epipolarity in the nucleus can be observed in young but not in aged HSCs for H4K16ac (Fig. 3.18A). We observed that H4K16pr seems to behave similarly but a clear limitation of this observation is the lack of additional replicates (Fig. 3.18B). Stunningly, no polarity for H4K16bu was observed suggesting a distinct role of H4K16 acylations during HSC aging (Fig. 3.18C). Grigoryan *et al* (2018) were not able to correlate gene expression and H4K16ac distribution in young or aged HSCs but observed a major localization of H4K16ac on chromosome 11. Indeed, an overlap between chromosome 11 and polarized H4K16ac in young HSCs was observed via 3D-ImmunoFISH (fluorescence in situ hybridization) and this overlap was reduced in aged cells (Grigoryan *et al*, 2018). Including our H4K16 acylation antibodies for such a 3D- ImmunoFISH approach and additional co-stainings for H4K16 acylations and epigenetic players regulating H4K16 acylations will be crucial to unravel how epipolarity is established and how the onset of HSCs aging is controlled. An interesting observation was made by Brown and colleagues (2013): SIRT3 was shown to be responsible for maintaining reactive oxygen species (ROS) in HSCs. During HSC aging, SIRT3 levels decrease and therefore ROS levels can increase which reduces the regenerative capabilities of HSCs. Overexpression of SIRT3 in old HSCs can reduce oxidative stress and induce their rejuvenation (Brown *et al*, 2013). Since we observed an acylation-specific binding of SIRT3 to H4K16 acylations it would be attractive to study specifically the nuclear SIRT3 localization.

All in all, we were able to show that H4K16 acylations mark predominantly euchromatin over heterochromatin. Excitingly, we unraveled a distinct biological difference for our acylations of

interest. While H4K16pr like H4K16ac seemed to lose polarity upon aging in HSCs, H4K16bu localization did not change, indicating their diverse function during stem cell fate decisions.

4.6. The genomic localization of H4K16 acylations

We also wanted to study the genomic localization of H4K16 acylations with our H4K16 acylation-specific antibodies and therefore started with the establishment of a working ChIP protocol. First, we compared crosslinked (X-ChIP) and native ChIP (N-ChIP) as well as MNase X-ChIP (MNase digestion of crosslinked material) and CUT&RUN (cleavage under targets & release using nuclease) in HEK293 and MEF cells (Fig. 3.20/22). Since the abundance of H4K16 non-acetyl acylations is known to be less abundant (Simity *et al*, 2017), we aimed for a ChIP approach that already resulted in a high enrichment of H4K16ac over input to increase the probability to also detect the other H4K16 acylations. Consequently, we decided for the N-ChIP approach (Fig. 3.20C) and further validated this protocol in another cell line with more open chromatin. After the successful validation for all H4K16 acylations via ChIP-qPCR (Fig. 3.23), we continued to study the genomic distribution in more detail by ChIP-seq (Fig. 3.24). Taking a closer look at the overview shown in Fig. 3.24 and considering ChIP-seq data from other histone acylations previously studied (Nitsch *et al*, 2021), we realized the co-occurrence of non-acetyl acylations and acylation at active genomic regions. Short-chain acylations are speculated to act collectively and their function is defined by a specific acylation/acetylation ratio rather than by changes in a single acylation type. In a sophisticated study from the Khochbin lab, this speculation was further supported. Gao *et al* (2020) directly demonstrated that an increase in H4K5 non-acetyl acylations can repel BRD4 binding from acetylated nucleosomes and enable binding of other interactors containing for example DPF or YEATS domains (preference for Kbu/Kcr over Kac). In addition, freed BRD4 is able to bind to other mainly acetylated genomic sites highlighting how shifts in the histone acylation/acetylation ratio can fine-tune transcriptional regulation (Gao *et al*, 2020). Our observed genomic annotation of H4K16 acylations in mESCs (Fig. 3.27) might also indicate how changes in this ratio could control gene expression. Satisfactorily, the annotation of H4K16ac enriched regions (Fig. 3.27) was in line with previously published ChIP results from Taylor *et al* (2013) suggesting that our ChIP approach technically worked. While 20 % of H4K16ac peaks were enriched in promoter-TSS regions, hardly any enrichment for H4K16pr and H4K16bu peaks at such regions was observed. Interestingly, intronic regions were mainly enriched for H4K16pr (~70 %), while intergenic regions were mostly enriched by H4K16bu (~40 %) and H4K16ac (~35 %). Excitingly, Taylor *et al* (2013) also observed a similar enrichment of H4K16ac peaks

in intergenic regions and were able to reveal that active enhancers can be marked by H4K16ac. Unfortunately, we were not able to include an analysis on H4K16 acylation enrichment in enhancer regions which would help to define the impact of H4K16 acylation/ acetylation ratios on gene expression.

Even though H4K16 acylations seemed to be preferentially enriched at different regions, still all H4K16 acylations correlated to a comparable degree with increasing gene expression (Fig. 3.28). As far as we are aware this is the first time that short-chain H4K16 acylations were correlated to gene expression *in cellulo*. We then wondered if dietary changes cannot only affect acyl-CoA/acetyl-CoA (co-factor) ratios but also the histone acylation/acetylation (substrate) ratio on chromatin.

4.7. The effect of diet on H4K16 acylations

Previous findings that metabolic changes upon high-fat diet (HFD) in mice can significantly influence hepatic gene expression (Siersbæk *et al*, 2017) made us wonder if such changes in gene expression could be actually induced by an altered epigenome. Since the link between metabolism and epigenetics is unquestionable, we were first interested in quantifying our co-factors of interest (acetyl-CoA, propionyl-CoA, and butryryl-CoA) in livers from HFD mice to reveal potential acyl-CoAs fluctuations upon HFD. Indeed, we observed an increase in acetyl-CoA and a decrease in propionyl-CoA and butyryl-CoA upon HFD (Fig. 3.29B). While the increase of acetyl-CoA upon HFD has not been observed to our knowledge by others, the decrease of propionyl-CoA and butyryl-CoA was also stated by Carrer *et al* (2017). We were then keen to study the genomic distribution of H4K16 acylation via ChIP-seq. We were able to detect an overlap of H4K16ac and H4K16bu signal at active genomic regions (Fig. 3.31) and unfortunately, we were not able to detect an enrichment over background for H4K16pr (data not shown). We observed genomic regions in which H4K16ac and H4K16bu increased while in other regions both acylations decreased upon HFD (Fig. 3.32/33). However, we were not able to detect a general increase or decrease for H4K16ac or H4K16bu upon diet. In comparison, Nie *et al* (2017) reported a decrease of H3K23pr and H3K18bu levels in total histone extracts from livers upon HFD while Bhattacharya *et al* (2021) observed an increase in H4K5bu levels upon HFD via immunofluorescence staining of the liver tissue samples. The described variability between previous HFD studies highlights how easily metabolism is affected by the composition (both chow and high-fat) and the length of the diet, by the age of mice and by laboratory differences (Chandrasekera & Barnard, 2014) and how care must be taken for a conclusive comparison between such studies.

Next, we made use of a publicly available RNA-seq dataset (Siersbæk *et al*, 2017) to link the acylations to gene expression and also to see if observed acyl-CoA changes upon diet (Fig. 3.29B) affect gene expression. We were able to link H4K16ac and H4K16bu levels to gene expression but no significant differences nor changes upon HFD were observed (Fig 3.34). Further, no correlation between up- and downregulated genes and general acylations levels upon HFD was revealed (data not shown). Interestingly, Siersbæk *et al* (2017) described that H3K27ac changes upon HFD can influence the activity of pre-established enhancers resulting in HFD-regulated gene transcription and that chromatin accessibility is mainly not affected upon diet. It would be again interesting to include an enhancer enrichment analysis of H4K16 acylations to study if active enhancers can be marked by them (Taylor *et al*, 2013).

It is further important to mention that HFD can influence the epigenome on multiple layers since secondary metabolic effects can originate from the gut microbiota that can adapt towards diet (Lai *et al*, 2014). Prolonged HFD can lead to an increase of succinic acid while butyric acid decreased potentially due to a microbiota adaption (Jakobsdottir *et al*, 2013) and further it was shown that SCAFs (short-chain fatty acids) like acetate, propionate, and butyrate can limit body weight gain during HFD treatment (Lu *et al*, 2016). Such changes of metabolites can directly affect the epigenome in addition to the actual diet since for example, SCAFs can be used to generate acyl-CoAs, and propionate and butyrate can also act as HDAC inhibitors (Trefely *et al*, 2020; Lu *et al*, 2016). These additional effects should be considered in future HFD approaches and might help to reduce discrepancies between independent studies focusing on the effect of HFD on the epigenome (Liu *et al*, 2015; Nie *et al*, 2017; Bhattacharya *et al*, 2021). All in all, we were able to observe H4K16ac and H4K16bu genomic-wide and correlate their levels to gene expression. The complex interactions between HFD, gut microbiota, and metabolism and their influence on the epigenome made us turn towards metabolic diseases for which the metabolic changes are better defined.

4.8. H4K16 acylations: A reservoir in metabolic disorders

We received liver samples from *Acads*$^{-/-}$ and *Pcca*$^{-/-}$ mice mimicking short-chain specific acyl-CoA dehydrogenase (SCAD) deficiency or propionic acidemia (PA). Importantly for us, a hallmark of SCAD deficiency is the increase of butyryl-CoA (16-fold increase) while upon PCCA deficiency propionylcarnitine (indicative for propionyl-CoA levels) is elevated (18-fold increase) in corresponding mouse models (Palladino *et al*, 2012; Guenzel *et al*, 2013). Excitingly, we observed an increase in H3K14pr and H4K16pr in livers from PCCA deficient mice by immunoblotting (Fig. 3.35) which we further validated by quantification via MS and

revealed a significant increase of propionylation in various lysines across H3 and H4 (Fig. 3.36). In SCAD-deficient mice, we were only able to observe a mild increase in H3K14bu and H4K16bu levels (Fig. 3.35). In line with this, Kebede *et al* (2017) were also not able to observe an increase of H3K14pr in liver-derived from *Acads*$^{-/-}$ mice. In contrast to these observations, Yang *et al* (2021) stated an increase in H3K9bu levels in heart samples from *Acads*$^{-/-}$ mice while H3K9cr levels decreased which might indicate again how histone acylations can act together and that their ratios can regulate chromatin functions. In addition, SCAD converts preferentially butyryl-CoA to crotonyl-CoA during the first step of β-oxidation and it was shown that MCAD (medium-chain acyl-CoA dehydrogenase) can compensate for malfunctional SCAD (Touw *et al*, 2014) which might explain why we were not able to detect severer changes in Kbu levels. Unfortunately, we were not able to analyze Kbu levels via a more sensitive MS approach.

We decided to focus more on the liver samples from the PA mouse model and performed ChIP-seq and RNA-seq experiments. Interestingly, we did not observe global changes in the gene expression upon PCCA deficiency (Fig. 3.38). Since hyperammonemia in the liver was reported in PA patients, we checked the expression levels of enzymes involved in the urea cycle but observed no significant differences upon PCCA deficiency (data not shown). This supports previous findings that hyperammonemia is rather induced by the inhibition of the first enzyme of the urea cycle (NAGS, N-acetylglutamate synthase) by accumulated propionyl-CoA competing against acetyl-CoA than by gene expression changes (Häberle *et al*, 2018; Filipowicz *et al*, 2006). We also checked the expression of apoptosis-related genes since hyperammonemia can induce hepatocyte cell death (Li et al., 2014) but we were not able to observe any significant changes in gene expression (data not shown). However, via our ChIP-seq data set we were able to observe various changes in the H4K16 acylation levels in samples from *Pcca*$^{-/-}$ mice (Fig. 3.39). We identified genomic regions in which H4K16pr was enriched upon PCCA deficiency while H4K16ac levels decreased and H3K9ac levels remained similar (Fig. 3.40/41). When comparing the enrichment of histone acylations to the level of gene expression, H3K9ac at TSSs did not change upon PCCA deficiency, while the H4K16ac enrichment decreased upon the deficiency. We observed a similar increase between H4K16bu enrichment (Fig. 3.43) and H4K16pr enrichment in *Pcca*$^{-/-}$ livers (~2-fold increase) around TSSs (Fig. 3.44) while the general coverage was higher for H4K16pr. Based on these results, we wanted to explore different genomic regions at which H4K16 acylations occurred and observed a general increase at various genomic regions only for H4K16pr in PCCA-deficient mice (Fig. 3.46). Considering that even though we observed a general increase in histone Kpr levels (Fig. 3.36 & Fig. 3.41) but no severe global effect on global gene expression profiles

(Fig. 3.38), our findings point to a rather "unconventional" role for histone acylations. Highly dynamic histone acetylations were described as a "reservoir for acetate" which can easily provide acetyl-CoA depending on cellular needs (Ye & Tu, 2019). We speculate that upon PCCA deficiency, constantly elevated propionyl-CoA levels could result in a prolonged storage of propionate which might be beneficial to cope with the accumulation of C3 molecules. In addition, since our *in vitro* findings suggest that H4K16pr can fine-tune chromatin dynamics differently than H4K16ac and also activates transcription to a lesser degree than H4K16ac, we hypothesize that a genome-wide increase of bulk histone propionylation might mainly help to absorb excess propionyl-CoA and that potential changes of chromatin dynamics or gene expression might not necessarily be significantly affected upon increased Kpr levels. Further, the liver itself is considered to be a sink for PA-related metabolites and one potential treatment of PA is actually liver transplantation which decreases the amount of accumulated toxic side products (Guenzel *et al*, 2015). In the future, we aim to address this "acylation sink hypothesis" in more detail which will help to dissect the role of histone acylations in metabolic diseases and might provide a new therapeutic perspective for the aberrant accumulation of metabolites.

4.9. Conclusion

With this thesis, I managed to answer multiple of the questions raised in the aims section. In summary, we were able to provide new insights into the roles of short-chain lysine acylations and demonstrated that histone acylations are not just another flavor of acetylation. Our *in vitro* data highlights how H4K16 acylations can fine-tune chromatin dynamics with the same tendency but to a different degree and that this can also stimulate *in vitro* transcription differently. *In cellulo*, we showed how diverse and cell type-specific the role of H4K16 acylations can be. *In vivo*, histone acylations can actually integrate fluctuations of metabolic intermediates and further seem to compensate for drastic metabolic changes by acting as a reservoir for short-chain fatty acids. What remains challenging is to gain a deeper understanding on how these different flavors of short-chain acylations could act synergistically through varying ratios that could define chromatin function. Another complex challenge is to unravel how metabolic information is integrated into the histone short-chain acylome and also to decipher the functions of histone acylations in metabolic diseases.

5. Materials

5.1. Antibodies

Table 5.1: Antibodies

Internal ID	Antibody	Species	Company	Catalogue/ serum number
267	H2B	Rabbit	Abcam	ab1790
268	H3K9ac	Rabbit	Abcam	ab4441
285	H4K16ac	Rabbit	Millipore	07-329
332	H4K16ac	Rabbit	Active Motive	39167
	H4K16pr #1	Rabbit	In house	
	H4K16pr #4	Rabbit	In house	
	H4K16pr #69	Rabbit	In house	
	H4K16pr	Rabbit	Thermo Fischer	PA5-112557
	H4K16bu #104	Rabbit	In house	
	SIRT3	Mouse	Santa Cruz	sc-365275
A	Goat anti-mouse HRP	Goat	Dako	P0447
J	Mouse anti-rabbit HRP	Mouse	JR	211-032-171
	anti-mouse IgG conjugated to alexa fluor 488	Donkey	Jackson ImmunoResearch	711-545-152
	anti-rabbit IgG conjugated to alexa fluor 594	Donkey	Jackson ImmunoResearch	111-585-144

5.2. Bacterial strains

Table 5.2: Bacterial strains

Strain	Genotype	Origin
DH5alpha	F– φ80lacZΔM15 Δ(lacZYA-argF)U169 recA1 endA1 hsdR17(r_K, m_K^+) phoA supE44 λ^- thi-1 gyrA96 relA1	Lab stock
BL21 Gold – Codon Plus (DE3) strain (for protein expression)	*E.coli* B F- ompT hsdS(rB- mB-) dcm+ Tetr galλ (DE3) endA [argUileY leuW CamR]	Stratagene
Stellar	F-, endA1, supE44, thi-1, recA1, relA1, gyrA96, phoA, Φ80d lacZΔ M15, Δ(lacZYA-argF) U169, Δ(mrr-hsdRMS-mcrBC), ΔmcrA, λ-	Lab stock

5.3. Buffers, medium and solutions

Table 5.3: Buffers, medium and solutions

Name	Specification	Composition
1x Phosphate-Buffered Saline (PBS)		10 mM Na_2HPO_4 2 mM KH_2PO_4 2.7 mM KCl 137 mM NaCl (adjust to pH 7.2)
1x Tris-Acetate-EDTA (TAE)		40 mM Tris-Acetate 1 mM EDTA
1x Tris-Borate-EDTA (TBE)		89 mM Tris-HCl 89 mM Boric acid 2 mM EDTA (pH 8.0)
1x Tris-Buffered Saline Tween (TBST)		150 mM NaCl 50 mM Tris-HCl pH 8 0.2 % Tween-20
1x Tris-EDTA (TE)		10 mM Tris-HCl (pH 8.0) 1 mM EDTA (pH 8.0)
RIPA buffer	Total protein extraction	50 mM Tris-HCl (pH 8.0) 150 mM NaCl 1 % IGEPAL 0.1 % SDS 1 % NP-40 0.5 % Sodium deoxycholate
Nuclear Isolation Buffer (NIB)	Histone extraction	15 mM Tris-HCl (pH 7.5) 60 mM KCl 15 mM NaCl 5 mM $MgCl_2$ 1 mM $CaCl_2$ 50 mM Sucrose
Buffer B	Histone acylation quantification via MS	0.1 % (v/v) Formic acid 98 % (v/v) Acetonitrile
SDS running gel	SDS-PAGE electrophoresis	6 to 18.7 % Acrylamide 375 mM Tris-HCl (pH 8.8) 0.1 % SDS
SDS stacking gel		5 % Acrylamide 125 mM Tris-HCl (pH 6.8) 0.1 % SDS
6x Laemmli sample loading buffer		30 % Glycerol 6 mM EDTA 10 % SDS 60 mM DTT 0.1 % Bromophenol Blue

10x SDS running buffer		247 mM Tris-HCl 1.9 M Glycine 0.5 % SDS
10x Transfer buffer	Western blot transfer	247 mM Tris-HCl 1.9 M Glycine
Coomassie brilliant blue staining		2 % Coomassie brilliant blue 40 % Ethanol 10 % Acetic acid
Ponceau S staining solution		0.5 % (w/v) Ponceau S 1 % Acetic acid
Histone Wash Buffer	Core histone expression	50 mM Tris-HCl (pH 7.5) 100 mM NaCl 1 mM EDTA (pH 8.0) 20 mM Nicotinamide 1x cOmplete™ EDTA-free protease inhibitor cocktail
SAU200/600/1000 Buffer		7 M Urea 20 mM CH_3COONa (pH 5.2) 200 mM/ 600 mM/ 1000 mM NaCl 1 mM EDTA (pH 8.0) 5 mM ß-mercaptoethanol
Unfolding Buffer	Truncated H4	7 M Guanidium hydrochloride 20 mM Tris-HCl (pH 7.5) 100 mM DTT
Buffer B_{trunc}		0.1 % Tri-fluoro acetic acid 90 % Acetonitrile
Chemical ligation buffer	Native chemical ligation for H4	200 mM $KHPO_4$ pH 7.9 2 mM EDTA pH 8.0 6 M Guanidine HCl
RPC Buffer A		0.1 % Tri-fluoro acetic acid/ H2O
RPC $B_{ligation}$		0.1 % Tri-fluoro acetic acid 90 % Acetonitrile
Unfolding Buffer	Octamer refolding	7 M Guanidium hydrochloride 20 mM Tris-HCl (pH 7.5) 10 mM DTT
Refolding Buffer		10 mM Tris-HCl (pH 7.5) 1 mM EDTA (pH 8.0) 2 M NaCl 5 mM ß-mercaptoethanol
RB-high	Nucleosome assembly	10 mM Tris/HCl pH7.5 1 mM EDTA 2 M NaCl 1 mM DTT

RB-low	Nucleosome assembly	10 mM Tris/HCl pH7.5 1 mM EDTA 100 mM NaCl 1 mM DTT
Loading buffer	DNA origami	5 mM $MgCl_2$ 5 mM TRIS base 1 mM EDTA 5 mM NaCl
Lysis buffer F	ACF purification	20 mM Tris-HCl (pH 7.9) 500 mM NaCl 4 mM $MgCl_2$ 0.4 mM EDTA 2 mM DTT 20 mM ß-glycerophosphate 20 % (v/vl) Glycerol 0.4 mM PMSF 1 mM Benzamidine-HCl 4 µg/ mL Leupeptin 2 µg/ mL Aprotinin
Wash buffer F		20 mM Tris-HCl (pH 7.9) 150 mM NaCl 2 mM $MgCl_2$ 0.2 mM EDTA 1 mM DTT 10 mM ß-glycerophosphate 15 % (v/v) glycerol 0.01 % (v/v) NP-40 0.2 mM PMSF 0.5 mM Benzamidine-HCl 2 µg/ mL Leupeptin 1 µg/ mL Aprotinin
Dilution buffer F		20 mM Tris-HCl (pH 7.9) 10 % Glycerol (v/v) 0.02 % NP-40
Lysis buffer H	NAP1 purification	50 mM Sodium phosphate (pH 7.6) 500 mM NaCl 20 mM Imidazole 15 % (v/v) Glycerol 0.01 % (v/v) NP-40 10 mM ß -glycerophosphate 0.2 mM PMSF 0.5 mM Benzamidine

Wash buffer	NAP1 purification	50 mM Sodium phosphate (pH 7.6) 100 mM NaCl 20 mM Imidazole 15 % (v/v) Glycerol 0.01 % (v/v) NP-40 10 mM ß -glycerophosphate 0.2 mM PMSF 0.5 mM Benzamidine
Dialysis buffer		25 mM HEPES (pH 7.6) 1 mM EDTA 10 % (v/v) Glycerol 100 mM NaCl 0.01 % (v/v) NP-40 10 mM ß -glycerophosphate
NAP1 buffer		10 mM HEPES (pH 7.6) 1 mM KCl 1.5 mM $MgCl_2$ 0.5 mM EDTA 10 % (v/v) Glycerol 0.01 % (v/v) NP-40 10 mM ß -glycerophosphate
HEPES-EDTA-Glycerol (HEG) Buffer	Chromatin assembly for IVT	25 mM HEPES (pH7.6) 0.1 mM EDTA 10 % Glycerol
Sucrose gradient buffer		50 mM HEPES (pH 7.5) 50 mM KCl 1 mM EDTA (pH 8.0) 5-40 % (w/v) Sucrose
BC50		20 mM Tris-HCl (pH 7.9) 50 mM KCl 0.2 mM EDTA 20 % Glycerol
8x Phosphate buffer	Gal4-VP16 purification	160 mM Sodium phosphate 4 M NaCl
Storag buffer		20 mM Tris-HCl (pH 7.9) 20 % (v/v) Glycerol 100 mM KCl 1 mM DTT 0.2 mM EDTA

Buffer B	p300 purification	20 mM Tris-HCl (pH 7.5) 250 mM NaCl 0.1 % IGEPAL 30 mM Imidazole 1x cOmplete™ EDTA-free protease inhibitor cocktail
Elution Buffer		20 mM Tris-HCl (pH 7.5) 100 mM NaCl 0.1 % IGEPAL 250 mM Imidazole 10 % (v/v) Glycerol 1x cOmplete™ EDTA-free protease inhibitor cocktail
Buffer A	Nuclear extract from HeLa cells	10 mM HEPES (pH 7.9) 1.5 mM $MgCl_2$ 10 mM KCl 0.5 mM DTT
Buffer C		20 mM HEPES (pH 7.9) 25 % (v/v) Glycerol 0.42 M NaCl 1.5 mM $MgCl_2$ 0.2 mM EDTA
Buffer D		20 mM HEPES (pH 7.9) 20 % (v/v) Glycerol 0,1 M KCl 0.2 mM EDTA 0.5 mM DTT
BC100	IVT	20 mM Tris-HCl (pH 7.9) 100 mM KCl 0.2 mM EDTA 20 % Glycerol
Coupling buffer	H4 peptide coupling	50 mM Tris-HCl (pH 8.5) 5 mM EDTA (pH 8.0)
Pull-down buffer A	Peptide affinity purification	50 mM Tris-HCl (pH 8.0) 150 mM NaCl 0.1 % IGEPAL 20 mM Nicotinamide 20 mM Sodium butyrate 1x cOmplete™ EDTA-free protease inhibitor cocktail 0.5 mM DTT
Pull-down dilution buffer		50 mM Tris-HCl (pH 8.0) 150 mM NaCl 0.25 % IGEPAL 20 mM Nicotinamide 20 mM Sodium butyrate 0.5 mM DTT

Dilution Buffer	X-ChIP	1 % Triton X-100 2 mM EDTA (pH 8.0) 150 mM NaCl 20mM Tris-HCl (pH8.0)
Elution Buffer		100 mM $NaHCO_3$ 1 % SDS
Final wash buffer		0.1 % SDS 0.5 % NP-40 2 mM EDTA 500 mM NaCl 20 mM Tris-HCl (pH 8.0)
L1 lysis buffer		50 mM Tris-HCl (pH 8.0) 2 mM EDTA (pH 8.0) 0.1 % NP-40 10 % Glycerol
L2 lysis buffer		1 % SDS 10 mM EDTA 50 mM Tris-HCl (pH 8.0)
Wash buffer		0.1 % SDS 0.5 % NP-40 2 mM EDTA 150 mM NaCl 20 mM Tris-HCl (pH 8.0)
10x Fixing solution	Mnase X-ChIP	100 mM NaCl 50 mM HEPES (pH 8.0) 1 mM EDTA (pH 8.0) 0.5 mM EGTA 11 % Formaldehyde
RIPA buffer		10 mM Tris-HCl (pH 8.0) 140 mM NaCl 1 % Triton X-100 0.1 % SDS 0.1 % Sodiumdeoxycholate 1 mM EDTA 1 mM PMSF 1x cOmplete™ EDTA-free protease inhibitor cocktail
Binding buffer	CUT&RUN	20 mM HEPES KOH (pH 7.5) 10 mM KCl 1 mM $CaCl_2$ 1 mM $MnCl_2$
Wash buffer		20 mM HEPES KOH (pH 7.5) 150 mM NaCl 0.5 mM Spermidine 1x cOmplete™ EDTA-free protease inhibitor cocktail

Dig-wash buffer	CUT&RUN	0.07 % Digitonin in wash buffer
Antibody buffer		2 mM EDTA in Dig-wash buffer
2x stop buffer		200 mM NaCl 20 mM EDTA 4 mM EGTA 50 mg/mL RNase A
NBA	N-ChIP (cells)	85 mM NaCl 5.5 % Sucrose 10 mM Tris-HCl (pH 7.5) 0.2 mM EDTA (pH 8.0) 0.2 mM PMSF 1x cOmplete™ EDTA-free protease inhibitor cocktail 1 mM DTT
NBB		85 mM NaCl 5.5 % Sucrose 10 mM Tris-HCl (pH 7.5) 0.2 mM EDTA (pH 8.0) 0.2 mM PMSF 0.1 % NP-40 1x cOmplete™ EDTA-free protease inhibitor cocktail 1 mM DTT
NBR		85 mM NaCl 5.5 % Sucrose 10 mM Tris-HCl (pH 7.5) 3 mM $MgCl_2$ 1.5 mM $CaCl_2$ 0.2 mM PMSF 1 mM DTT
Stop buffer	N-ChIP (general)	215 mM NaCl 5.5 % Sucrose 10 mM Tris-HCl (pH 8.0) 20 mM EDTA (pH 8.0) 2 % Triton X-100 0.2 mM PMSF 2x cOmplete™ EDTA-free protease inhibitor cocktail 1 mM DTT
Elution buffer		0.1 M $NaHCO_3$ 1 % SDS
Block solution		1x PBS 0.5 % BSA (w/v)
ChIP W1		150 mM NaCl 10 mM Tris-HCl (pH 8) 2 mM EDTA (pH 8.0) 1 % NP-40

	N-ChIP (general)	1 % Sodium deoxycholate 0.1 mM PMSF 1x cOmplete™ EDTA-free protease inhibitor cocktail 0.5 mM DTT
Buffer 1	N-ChIP (tissue)	0.3 M Sucrose 60 mM KCl 15 mM NaCl 5 mM $MgCl_2$ 0.1 mM EDTA (pH 8.0) 15 mM Tris-HCl (pH 7.5) 0.1 mM PMSF 1x cOmplete™ EDTA-free protease inhibitor cocktail 0.5 mM DTT
Buffer 2		0.3 M Sucrose 60 mM KCl 15 mM NaCl 5 mM $MgCl_2$ 0.1 mM EDTA (pH 8.0) 15 mM Tris-HCl (pH 7.5) 0.4 % IGEPAL 0.1 mM PMSF 1x cOmplete™ EDTA-free protease inhibitor cocktail 0.5 mM DTT

5.4. Chemicals and reagents

Table 5.4: Chemicals and reagents

Name	**Source/ Specification**
2-[4-(2-hydroxyethyl)piperazin-1-yl]ethanesulfonic acid (HEPES)	Roth, Karlsruhe, Germany
2X Absolute Blue qPCR SYBR Green Mix	Thermo Fisher Scientific, Waltham, USA
4-(2-Aminoethyl)benzolsulfonylfluorid (AEBSF)	Sigma-Aldrich, St. Louis, USA
Acetic acid	VWR, Ismaning, Germany
Acrylamide 40 %	SERVA Electrophoresis, Heidelberg, Germany
Agarose	Roth, Karlsruhe, Germany
Agencourt AMPure XP magnetic beads (Beckman Coulter)	Agilent Technologies, Waldbronn
Ammonium sulfate	VWR, Ismaning, Germany
Ammonium chloride	Roth, Karlsruhe, Germany

Ammonium persulfate (APS)	Roth, Karlsruhe, Germany
Ampicillin	Roth, Karlsruhe, Germany
Aprotinin	Roth, Karlsruhe, Germany
Adenosine 5′-triphosphate disodium salt hydrate (ATP)	Sigma-Aldrich, St. Louis, USA
Beta-mercaptoethanol (ß-mercaptoethanol)	Roth, Karlsruhe, Germany
Bradford reagent	Roth, Karlsruhe, Germany
Bromophenol blue	Sigma-Aldrich, St. Louis, USA
Bovine Serum Albumin Fraction V	Carl Roth, Karlsruhe, Germany
Calcium chloride ($CaCl_2$)	Merck, Darmstadt, Germany
Cesium chloride (CsCl)	Sigma-Aldrich, St. Louis, USA
Charcoal activated	VWR, Ismaning, Germany
CHIR 99021	Axon Biochemicals BV, Groningen, the Netherlands
Colloidal coomassie stock	Roth, Karlsruhe, Germany
cOmplete™ EDTA-free protease inhibitor cocktail	Roche, Basel, Switzerland
Coomassie brilliant blue	Roth, Karlsruhe, Germany
Coverslips	Thermo Fisher Scientific, Waltham, USA
Creatine phosphate	Roche, Basel, Switzerland
Creatine phosphokinase	Roche, Basel, Switzerland
Cysteine-HCl	Roth, Karlsruhe, Germany
Digitonin	Merck, Darmstadt, Germany
Di-potassium hydrogen phosphate (HK_2O_4P)	Roth, Karlsruhe, Germany
Di-sodium hydrogen phosphate (Na_2HPO_4)	Roth, Karlsruhe, Germany
Dimethyl sulfoxide (DMSO)	Roth, Karlsruhe, Germany
Dithiothreitol (DTT)	Applichem, Darmstadt, Germany
DMEM Dulbecco's Modified Eagle's Medium - low glucose	Sigma-Aldrich, St. Louis, USA
DMEM Dulbecco's Modified Eagle's Medium - high glucose	Sigma-Aldrich, St. Louis, USA
Dynabeads™	Thermo Fisher Scientific, Waltham, USA
ECL detection reagent	Bio-Rad Laboratories, München, Germany
Ethylenediaminetetraacetic acid (EDTA)	Roth, Karlsruhe, Germany

Ethylene glycol bis(β-aminoethylether) tetraacetic acid (EGTA)	Roth, Karlsruhe, Germany
Ethanol (EtOH) 100 %	Roth, Karlsruhe, Germany
Ethidium bromide (EtBr)	Roth, Karlsruhe, Germany
Fetal bovine serum (FBS) (GIBCO)	Thermo Fisher Scientific, Waltham, USA
Formaldehyde 37 %	Sigma-Aldrich, St. Louis, USA
Glycerol	Roth, Karlsruhe, Germany
Hydrochloric acid (HCl)	Roth, Karlsruhe, Germany
NP-40	Sigma-Aldrich, St. Louis, USA
IGEPAL CA-630®	Sigma-Aldrich, St. Louis, USA
Imidazole	Roth, Karlsruhe, Germany
Isopropyl β-d-1-thiogalactopyranoside (IPTG)	Roth, Karlsruhe, Germany
Isoamylalcohol	Roth, Karlsruhe, Germany
Isopropanol	VWR, Ismaning, Germany
Kanamycin	Roth, Karlsruhe, Germany
Leukemia inhibitory factor (LIF)	IGBMC, Strasbourg, France
Leupeptin	Roth, Karlsruhe, Germany
Magnesium chloride ($MgCl_2$)	Roth, Karlsruhe, Germany
MEM Non-essential Amino Acid Solution 100X	Sigma-Aldrich, St. Louis, USA
Nicotinamide (Nam)	Alfa Aesar, Haverhill, USA
Nε-acetyllysine (KAc)	Bachem, Bubendorf, Switzerland
PBS (Dulbeco's phosphate buffered saline)	Sigma-Aldrich, St. Louis, USA
PD 0325901	Axon Biochemicals BV, Groningen, the Netherlands
Penicillin-Streptomycin	Sigma-Aldrich, St. Louis, USA
Ponceau Red S	Sigma-Aldrich, St. Louis, USA
Potassium chloride (KCl)	Roth, Karlsruhe, Germany
Potassium di-hydrogen phosphate (KH_2PO_4)	Roth, Karlsruhe, Germany
Powdered milk, blotting grade	Carl Roth, Karlsruhe, Germany
Propionic anhydride-d_{10}	Merck, Darmstadt, Germany
Proteinase K	Sigma-Aldrich, St. Louis, USA
RNase A	Sigma-Aldrich, St. Louis, USA

RNasin® Ribonuclease Inhibitors	Promega, Madison, USA
Sodium acetate (CH_3COONa)	Roth, Karlsruhe, Germany
Sodium azide (NaN_3)	Roth, Karlsruhe, Germany
Sodium bicarbonate ($NaHCO_3$)	Roth, Karlsruhe, Germany
Sodium butyrate (NaBu)	Alfa Aesar, Haverhill, USA
Sodium chloride (NaCl)	Roth, Karlsruhe, Germany
Sodium dihydrogen phosphate (NaH_3PO_4)	Roth, Karlsruhe, Germany
Sodium dodecyl sulfate (SDS)	Roth, Karlsruhe, Germany
Sodium hydroxide (NaOH)	Roth, Karlsruhe, Germany
Sodium thiosulfate ($Na_2S_2O_3$)	Sigma-Aldrich, St. Louis, USA
Spectinomycin	Roth, Karlsruhe, Germany
Sucrose	Roth, Karlsruhe, Germany
SulfoLink™ Coupling Resin	Thermo Fisher Scientific, Waltham, USA
SYBR Green I	Thermo Fisher Scientific, Waltham, USA
Tetramethylethylenediamine (TEMED)	Roth, Karlsruhe, Germany
Tricine	Roth, Karlsruhe, Germany
Tris-Base	Sigma-Aldrich, St. Louis, USA
Tris-HCl	Sigma-Aldrich, St. Louis, USA
Triton X-100	Roth, Karlsruhe, Germany
Tween-20	Sigma-Aldrich, St. Louis, USA
Urea	Sigma-Aldrich, St. Louis, USA
UTP, [α-32P]	Perkin Elmer, Waltham, USA
Vector mounting media with DAPI	Vector Laboratories, Burlingame, USA

5.5. Kits

Table 5.5: Kits

Name	**Source/ Specification**
Agilent High Sensitivity DNA Bioanalysis kit	Agilent Technologies, Waldbronn
Agilent RNA 6000 Nano kit	Agilent Technologies, Waldbronn
BCA Protein Assay kit (Pierce)	Thermo Fisher Scientific, Waltham, USA
NEBNext High-Fidelity 2X PCR Master Mix	New England Biolabs, Frankfurt a.M., Germany

NEBNext Multiplex Oligos for Illumina	New England Biolabs, Frankfurt a.M., Germany
NEBNext Ultra II DNA Library Prep kit for Illumina	New England Biolabs, Frankfurt a.M., Germany
TruSeq stranded mRNA Sample Preparation kit	Illumina, San Diego, USA
QIAGEN Plasmid Mini/ Maxi Kit	Qiagen, Hilden, Germany
QIAquick PCR Purification kit	Qiagen, Hilden, Germany
Qubit dsDNA HS Assay kit	Thermo Fisher Scientific, Waltham, USA
Qubit RNA HS Assay kit	Thermo Fisher Scientific, Waltham, USA
Quick-RNA Miniprep kit	Zymo, Freiburg, Germany
RevertAid First Strand cDNA kit	Thermo Fisher Scientific, Waltham, USA

5.6. Mammalian cell lines and tissues

Table 5.6: Mammalian cell lines and tissues

Name	**Specification & Source**
HEK293	Human embryonic kidney
HeLa S3	Human cervix carcinoma immortalized cell Line (IGBMC, Straßbourg, FR)
HSCs	Human hematopotic stem cells (Universität Ulm, Ulm, DE)
MEFs	Mouse embryonic fibroblasts, immortalized
$Mof^{flox/flox}Cre^{+}$ MEFs	Mouse embryonic fibroblasts (USC, Los Angeles, USA)
mESCs	Mouse embryonic stem cells (ESW26) (MPI, Freiburg, DE)
Pcca$^{-/-}$ liver tissue	Propionyl-CoA carboxylase alpha deficient mice (CSIC-UAM, Madrid, ES)
Acads$^{-/-}$ liver tissue	Short-chain acyl-CoA dehydrogenase deficien mice (ISMMS, New York, US)

5.7. Plasmids

Table 5.7: Plasmids

Internal ID	**Vector**	**Origin**
pTB089	pET24b(+)-hH4MetI29C	Till Bartke (HMGU, München, DE)
pTB008	pET21b(+)-hH2B	
pTB024	pET21b(+)-hH2A	

pTB013	pET21b(+)-hH3.1	
PL1527	pG5-MLP	Raphael Margueron (Institut Curie, Paris, FR)
pET0395	pET15b GAL4-VP16	
PL1675	pFastBac1 Acf1-FLAG	Peter Becker (LMU, München, DE)
PL1676	pFastBac1 ISWI-FLAG	
	pK19-PA-MN	Ahmed El Marjou (Institut Curie, Paris, FR)

5.8. Peptides

Table 5.8: Peptides

Internal ID	Vector	Origin
H4K16un	Genecust	GKGGAKRHRKGC
	Cambridge Peptide	Ac-SGRGKGGKGLGKGGA-K(un)-RHRKVLRDNIQG-S-Bzl
H4K16ac	Genecust	GKGGAK(ac)RHRKGC
	Cambridge Peptide	Ac-SGRGKGGKGLGKGGA-K(ac)-RHRKVLRDNIQG-S-Bzl
H4K16pr	Genecust	GKGGAK(pr)RHRKGC
	Cambridge Peptide	Ac-SGRGKGGKGLGKGGA-K(pr)-RHRKVLRDNIQG-S-Bzl
H4K16bu	Genecust	GKGGAK(bu)RHRKGC
	Cambridge Peptide	Ac-SGRGKGGKGLGKGGA-K(bu)-RHRKVLRDNIQG-S-Bzl

5.9. Primer

Table 5.9: Primers

Internal ID	Name	Forward/ Reverse	5'-3' sequence
	m*Mof*	F	AAGAACCGACTCGCACTGAC
		R	AAGACAAAGGGCTCCACATC
OL929	h*ACTB*	F	TAGAAGTCGCAGGACCACACT
OL930		R	TGGGTAGGTTTGTAGCCTTCAT
OL1657	h*RPL10*	F	ACCCGTCTTCGACAGGACT
OL1658		R	GGAACGGAAGACGAGAACAG
OL161	h*MYOD1*	F	GGCAACCGCTGGTTTGG
OL162		R	CCGCCTGAGCAAAGTAAATGA
OL919	Gene desert (human)	F	AATCACCTTGCATCTGTTTGG

OL920	Gene desert (human)	R	AAAAGGAGAAACCCAGTGGAA
OL603	m*Pou5f1*	F	TGAACTGTGGTGGAGAGTGC
OL604		R	AGGAAGGGCTAGGACGAGAG
	m*Sox2*	F	CTTGTGTCAGGGTTGGGAGT
		R	GAGTCCTCTGCCCATGTAGC
	m*Tcl1*	F	GGCATTGCAATTTTCTGCTT
		R	GGTCTCCTGCTACCAGCATC
OL506	m*1500005IO2Rik*	F	GGGACAGTCAAGTCCAGAGC
OL507		R	AACCAATCCATGGCAGAGAC
OL439	mIntergenic	F	GCTCCGGGTCCTATTCTTGT
OL440		R	TCTTGGTTTCCAGGAGATGC
OL 435	m*Gapdh*	F	CTCTGCTCCTCCCTGTTCC
OL 436		R	TCCCTAGACCCGTACAGTGC
OL 437	m*Hprt*	F	CCAAGACGACCGCATGAGAG
OL 438		R	CAACGGAGTGATTGCGCATT
	m*Pck1*	F	TATGAAGTCCAAGAGGCGTC
		R	GACTAAACTTTGACCCTGCC
	m*Trim63*	F	TGGAAACGCTATGGAGAACC
		R	ATGTCGTTGGCACACTTCC

6. Methods

6.1. Molecular biology methods

6.1.1. Purification of nucleic acids by phenol-chloroform extraction

For the purification of nucleic acids, one sample volume of phenol-chloroform was added to the sample. After mixing by inversion, the sample was centrifuged at 20000 xg for 10 min at RT. The upper aqueous phase was transferred to a new tube and one sample volume of 100 % ice-cold ethanol, 1/10 sample volume of 3 M sodium acetate pH 5.2 and 10 µg glycogen were added. The mixture was vortexed and the DNA or RNA was precipitated for at least 1h at -20 °C. After the precipitation, samples were centrifuged at 4 °C for 20 min at 20000 xg. The supernatant was carefully removed and the pellet was washed with 70 % ice-cold ethanol and centrifuged at 4 °C for 10 min at 20000 xg. The pellet was dried for around 5 min at RT and resuspended in 1x Orange G loading buffer for immediate agarose gel electrophoresis.

6.1.2. Agarose gel electrophoresis

5x DNA loading dye was added to samples containing DNA. The mixture was loaded on a 0.8-2 % agarose gel in 1x TAE or 0.5x TBE depending on the expected DNA fragment size. The gel was either pre-stained with 1x SYBR Safe DNA gel dye or stained after the electrophoresis with 1 mg/mL ethidium bromide for 15-20 min. The agarose gel was then analyzed under 254 nm UV light.

6.1.3. Heat shock transformation of *E. coli*

Chemically competent *E. coli* were thawed on ice and were mixed with 20 to 100 ng of DNA plasmid. Bacteria were incubated on ice for 15 min and transformed via a heat shock at 42 °C for 45 sec. After a 5 min incubation on ice, 500 µL of LB was added to the transformed *E. coli*. Bacteria were recovered for 1 h at 37 °C (shaking at 500 rpm) and then plated on a LB-agar plate supplemented with appropriate antibiotics. The BL21 DE Gold strain was used for protein expression. The DH5alpha strain was used for general plasmid propagation, while Stellar cells were used for the plasmid generation for the *in vitro* transcription assay. All incubation steps with Stellar cells were performed at 30 °C.

6.1.4. Plasmid DNA purification from *E. coli*

Single colonies from transformed *E. coli* were picked from LB-agar plates to inoculate LB media supplemented with the appropriate antibiotics. Depending on the culture volume,

plasmid DNA was purified with QIAGEN Plasmid Mini or Maxi kit according to the manufacturer's instructions.

6.1.5. Cesium chloride gradient centrifugation of plasmid DNA

For the *in vitro* transcription assay, the assembly of chromatin highly depends on intact plasmid DNA. That is why such a plasmid was further purified via a cesium chloride (CsCl) gradient after the purification via the QIAGEN Plasmid Maxi kit. A CsCl gradient purification allows a separation of supercoiled DNA from nicked, linearized, and genomic DNA and RNA. Therefore, up to 500 µg of pG5-MLP plasmid were resuspended in 4.5 mL of TE buffer containing 4.4 g of CsCl at RT. 400 µL of 1 mg/mL ethidium bromide in 1x TE were added to the mix for the later visualization of the DNA. The sample was centrifuged at 48.000 rpm overnight at RT (NVT90 rotor, Beckman, USA). After centrifugation, the separation of plasmid DNA was observed under 254 nm UV light, and only supercoiled DNA was recovered (lower band). Ethidium bromide was extracted from the purified DNA by repetitive washing steps with isopropanol saturated with CsCl. The plasmid DNA was further precipitated with isopropanol (2x the sample volume) and pelleted at 17000 xg for 20 min at 4 °C. The DNA pellet was washed with 70 % ethanol before being resuspended in 100 µL 1x TE. The plasmid was aliquoted and stored at -20 °C.

6.1.6. RNA purification and reverse transcription from mammalian cells and tissue

Total RNA was extracted and purified from mammalian cells and tissue (5-30 mg) using the Quick-RNA Miniprep kit according to the manufacturer's instructions. RNA concentration was measured on a Nanodrop or via Qubit (RNA HS Assay kit). For reverse transcription, 100 ng of total RNA was used per reaction. The RevertAid H Minus First Strand cDNA Synthesis kit was used to synthesize complementary DNA (cDNA). For one reverse transcription reaction 100 ng of RNA were mixed with 4 µL 5x reaction buffer, 2 µL dNTP mix, 1 µL oligo(dT) 18 primer, 1 µL RiboLock RNase inhibitor, 1 µL RevertAid H Minus reverse transcriptase and nuclease-free water was added for a final volume of 20 µL. The mixture was incubated for 1 h at 42 °C and then for 5 min at 70 °C.

6.1.7. Quantitative PCR

In order to quantify the concentration of specific DNA fragments, quantitative PCR (qPCR) was carried out. For a standard reaction, 1 µL of ChIP DNA or 1:5 diluted cDNA (1:2 or 1:5) was mixed with 10 µL 2x SYBR Green PCR Master Mix, 2 µL of 1µM forward/ reverse primer

mix (100 nM final) and 7 µL ddH_2O. The qPCR run started with a 15 min long initial denaturation at 95 °C which was followed by 40 cycles of: denaturation (15 sec at 95 °C), annealing (30 sec at 60 °C), and elongation (30 sec at 72 °C). A melting curve was generated for 3 min at 60 °C and for 1 sec at 95 °C. The Ct-values were used to calculate the expression of genes. Fold changes were calculated by normalizing target gene expression to housekeeping gene expression (GAPDH) via the ΔΔct-method. ChIP-qPCR data was normalized to 1 % input material via the percent input method (Haring *et al*, 2007).

6.1.8. RNA-seq from liver samples

Total RNA samples purified from tissues were further analyzed via Bioanalyzer measurement using the Agilent RNA 6000 Nano kit following the manufacturer's instructions. Samples with an RNA integrity number (RIN) higher than 7 were further diluted to a final concentration of 100 ng/µL. For the library preparation and sequencing, samples were submitted to the HMGU sequencing facility. For each condition, three technical replicates were submitted for mRNA sequencing (poly-A selected). The libraries were prepared using the TruSeq stranded mRNA Sample Preparation kit, following the kit's instructions. After a final QC, the libraries were sequenced in a paired-end mode (2x150 bp) in the Novaseq6000 sequencer (Illumina) with a depth of ≥ 100 million paired reads per sample.

6.1.9. RNA-seq analysis

Paired-end sequencing reads (150 bp) were mapped to the reference genome (Mus musculus GRCm38 dna primary assembly) using STAR aligner (version 2.7.6a). Uniquely mapped reads were counted per genes with STAR --quantMode GeneCounts using the annotation GRCm38.101. RNA abundance was estimated by calculating TPM (transcript per million) using rsem (version 1.3.1).

Downstream analyses were carried out in R (version 3.6.1) using helper function from the HelpersforDESeq2 package (https://github.com/tschauer/HelpersforDESeq2). Differential analysis on read counts was performed by DESeq2 (version 1.26). Genes with at least one mapped read detected in half of the samples were considered. Significant differentially expressed genes were defined by an adjusted p-value cutoff of 0.05. GO enrichment analysis on up- or down-regulated genes was performed by the topGO package (version 2.36.0) using Fisher statistics.

6.2. Biochemical assays

6.2.1. SDS-PAGE electrophoresis

Sodium Dodecyl Sulfate Polyacrylamide Gel Electrophoresis (SDS-PAGE) was performed to separate proteins according to their molecular weight (MW). Depending on the MW of the protein of interest the polyacrylamide percentage of the running gel ranged between 8 and 18.7 % in 375 mM Tris pH 8.8 and 0.1 % SDS. The running gel was overlaid with a stacking gel (5 % polyacrylamide in 125 mM Tris pH 6.8 and 0.1 % SDS). Before loading the protein samples on the gel, they were boiled in 1x Laemmli loading buffer for 5 min at 95 °C. Electrophoresis was performed in 1x SDS running buffer and depending on the running gel percentage for 1-2 hours at 140-200 V. Once the gel run was complete, the proteins were immediately stained with Coomassie blue or transferred to a nitrocellulose membrane for specific detection of a protein or PTM of interest.

6.2.2. Western blot transfer

After the SDS-PAGE electrophoresis, separated proteins were transferred from the SDS gel to a 0.45 µm pore size nitrocellulose membrane to further detect proteins or PTMs of interest. Proteins were transferred in 1x glycine transfer buffer for 1 h at 230 mA. For proteins with a higher molecular weight, the transfer was extended for 30 min at 350 mA. Transfer efficiency as well as relative loading amounts were checked immediately after the transfer by staining the membrane for at least 5 min with ponceau S staining solution.

6.2.3. Immunoblotting

After an efficient western blot transfer, the nitrocellulose membrane was then blocked with 4 % BSA or 5 % milk in 1x TBST for 1 hour at RT. After blocking, the membrane was incubated overnight at 4 °C with the primary antibody diluted in blocking solution. The next day, the membrane was washed three times in 1x TBST for 5 min each time before the secondary antibody conjugated to horseradish peroxidase (HRP) in 4 % BSA in 1x TBST was added. After an 1 h incubation at RT, the membrane was again washed three times with 1x TBST for 5 min. For the detection of the protein or PTM of interest, the membrane was incubated with Clarity or Clarity Max enhanced chemiluminescent (ECL) western blotting substrate for 5 min at RT. Membranes were then developed via a ChemiDoc imager. The signal quantification was performed via ImageJ.

6.2.4. Protein extraction

Total protein extraction from cells was performed with RIPA buffer containing sodium deoxycholate, an ionic detergent, to disrupt the nuclear membrane. Cells and homogenized tissue were washed with ice-cold PBS supplemented with inhibitors (10 mM nicotinamide, 10 mM sodium butyrate, 1x protease inhibitor cocktail) and pelleted at 4000 xg for 10 min. For ~5 mg of tissue 300 µL RIPA buffer with mentioned inhibitors was used, while ~1x10^6 cells were resuspended in 60 µL RIPA buffer. Samples were incubated for 30 min on ice and then centrifuged for 30 min at maximum speed at 4 °C. The supernatant was collected and stored at -20 °C. Protein concentrations were measured via Bradford or BCA protein assay.

6.2.5. Acidic histone extraction

Cells were collected by centrifugation at 300 xg for 5 min at RT and washed twice with PBS. The packed cell volume was approximately estimated and cells were washed with 1:10 cell pellet to NIB buffer (appropriate inhibitors were added freshly). Cells were collected again by centrifugation at 700 xg for 5 min. Cells were then lysed by resuspension in 1:10 cell pellet to NIB buffer containing 0.2 % NP-40 and incubated for 10 min on ice. For tissue samples, 10-30 mg of frozen tissue were directly homogenized via douncing (10 to 20 strokes) in 100-300 µL NIB buffer containing 0.2 % NP-40. The sample was then centrifuged at 1000 xg for 10 min at 4 °C. The nuclei pellet was gently resuspended in 1:10 NIB buffer and centrifuged at 1000 xg for 5 min at 4 °C. This wash step was repeated two more times. The nuclei were then resuspended in 1:5 (v/v) pre-cooled 0.2 M H_2SO_4, and incubated for 4 h while rotating at 4 °C. The sample was centrifuged at 3400 xg at 4 °C for 5 min and the supernatant was collected and centrifuged again to remove any insoluble material. Histones were precipitated from the cleared supernatant by adding 100 % TCA for a final concentration of 33 %. Samples were mixed by inversion and incubated overnight on ice. The next day, samples were centrifuged at 3400 xg for 5 min at 4 °C. The supernatant was carefully removed and pelleted histones were rinsed with 0.1 % HCl in ice-cold acetone. After centrifugation for 2 min at 3400 xg at 4 °C, the supernatant was again carefully removed. This washing step was repeated one more time with 100 % ice-cold acetone. Finally, the pellet was dried and dissolved in 50 to 100 µL ddH_2O depending on the size of the pellet. Resolved histones were centrifuged at 4 °C for 2 min at 3400 xg and the supernatant was transferred to a new tube. Extracted histones were quantified via BCA assay and their purity was validated by SDS-PAGE analysis on an 18.7 % acrylamide gel and coomassie staining.

6.2.6. Histone acylation quantification via MS

Acylation levels from extracted histones were analyzed via LC-MS/MS using a hybrid chemical derivatization method as described previously (Maile *et al*, 2015). For this, 4 µg of purified histones were diluted with MS grade H_2O to a total volume of 18 µl. Then, 2 µL of 1 M TEAB (triethylammonium bicarbonate buffer) was added to adjust the pH to 8.5. Heavy propionic anhydride-d10 containing deuterium was diluted 1:100 with MS grade $H_2O$and 2 µl of the mixture was added immediately to the prepared histone sample while vortexing. The sample was incubated for 5 min at RT after which 2 µl of 80 mM hydroxylamine was added. The mixture was incubated for 20 min at RT. 0.5 µg trypsin was added and the sample was digested at 37 °C overnight. The next day, 6 µl of a freshly prepared 1% v/v solution of PIC (phenyl isocyanate) in acetonitrile was added to the peptides. The mixture was incubated for 1 h at 37 °C after which TFA was added to the sample for a final concentration of 1 %. The mixture was de-salted with C18 spin columns following the manufacturer's instructions. After eluting the peptides from the C18 spin columns with 70 % acetonitrile, peptides were partially speed-vacuum dried and resuspended in 30 µl 0.1 % TFA. The mixture was then analyzed by a nano-flow liquid chromatography-tandem mass spectrometry (LC-MS/MS) on a Q-Exactive HF mass spectrometer coupled to an Ultimate 3000 nanoUPLC (Ultimate 3000, Dionex, Sunnyvale, CA) in data-dependent acquisition (DDA) mode. Around 300 ng of peptides per sample were used per injection and the peptides were automatically loaded on a trap column (300 µm inner diameter ×5 mm, Acclaim PepMap100 C18, 5 µm, 100 Å; LC Packings, Sunnyvale, USA). Peptides were then separated on a C18 reversed-phase chromatography on the analytical column (nanoEase MZ HSS T3 Column, 100 Å, 1.8 µm, 75 µm × 250 mm; Waters, Milford, USA). Peptide separation was performed at a flow rate of 0.250 µL/min over a linear gradient from 1 % to 25 % buffer B for 40 min followed by a linear gradient to 40 % B in 20 min and then to 85 % B in 5 min. After 5 min at 85 % buffer B, the gradient was reduced to 1 % buffer B over 2 min and remained at this concentration for 8 min. Full mass range spectra were at 60,000 resolution (at m/z 400), and product ions spectra were collected in a "top 15" data-dependent scan cycle at 15000 resolution. RAW MS data were analyzed using EpiProfile 2.0 software. The reported relative abundances of histone modifications were validated by manual re-quantification using an open-source Skyline software.

6.2.7. Expression of recombinant unmodified histones and truncated histone H4

Canonical recombinant human histones were expressed and purified from *E.coli* as described by Luger *et al*, 1999. H3, H2A, H2B, and truncated H4 were expressed in BL21 DE3 Gold

strain. After the transformation of bacterial cells with the plasmid DNA, the cells were plated on agar plates containing the appropriate antibiotics overnight at 37 °C. The next day, a single colony was picked to inoculate an overnight culture of 50 mL LB with antibiotics at 37 °C. 1 L of LB with antibiotics was inoculated with ~25 mL from the overnight culture (initial OD600 < 0.1) and grown at 37 °C until OD600 reached 0.4-0.5. Expression of histones was induced with 0.5 mM IPTG and was continued for 3-3.5 h at 37 °C. The expression of H4Δ1-28 I29C was induced at an OD600 of 0.6 with 0.2 mM IPTG and the cultures were further incubated at 37 °C for 2 h. Next, the bacteria were collected at 4000 xg for 5 min. For unmodified core histones, the bacterial pellet was resuspended in 25 mL histone (unmodified) wash buffer without Triton X-100 but supplemented with 1x protease inhibitor cocktail and snap frozen at -80 °C for at least 1 h before the purification was performed as described in 6.2.5. For expressed truncated H4, the bacterial pellet was resuspended in 40 mL histone (truncated) wash buffer and snap frozen at -80 °C before the purification was performed as described in 6.2.6.

6.2.8. Purification of recombinant unmodified histones

All histones were purified with the same protocol, except for the truncated histone H4 (see 6.2.6). The cells were rapidly thawed in a water bath at 37°C and all the following steps were performed on ice. The cell suspension was sonicated on ice (Branson sonicator setting: duration: 3 times for 1 min, 0.5 sec ON and 0.5 sec OFF, amplitude: 50 %). After sonication, the lysate was centrifuged for 10 min at 17000 xg. The pelleted inclusion bodies were washed twice in 20 mL wash buffer with 1% Triton X-100 and twice in 20 mL wash buffer without Triton X-100. The pellet was then resuspended in 20 ml unfolding buffer and the histones were unfolded by rotating at RT for 1h. The solution was centrifuged for 15 min at 17000 xg. The supernatant was transferred to a new tube and centrifuged again. Then the supernatant was dialyzed at 4 °C against three changes of 2 L freshly prepared SAU200 buffer (incubation for 3 h, overnight, and again for 3 h). The next day, the histones were centrifuged at 17000 xg for 20 min to remove precipitated material. A 6 mL ResourceS cation exchange column (GE) was equilibrated with SAU200 buffer before the cleared supernatant was loaded onto it. The sample was separated over a linear gradient ranging from 0 to 100 % of SAU200 to SAU600 over 40 mL. Fractions of 500 µl were collected and the peak fractions were analyzed by SDS-PAGE. Fractions containing pure histone were pooled and dialyzed against three changes of 2 L H_2O supplemented with 2 mM ß-mercaptoethanol. The next day, precipitations from dialyzed histones were removed by centrifugation at 17000 xg for 20 min at 4 °C. Histone were quantified via absorbance measurements at 276 nm and the following equation from Luger *et*

al 1999: OD276/molar extinction coefficient (ε_{276}) * molecular weight = µg/µl. Molecular weight and molar extinction coefficients are listed in Table 6.1 below. Histones were lyophilized in 1-2 mg aliquots and stored at -80 °C.

Table 6.1: Molecular weight & molar extinction coefficient of core human histones

Histone	Molecular weight	ε_{276} for cm/M
H2A	13960	4050
H2B	13774	6070
H3	15273	4040
H4	11236	5400

6.2.9. Purification of truncated histone H4

All the following steps during the purification of truncated histone H4 were performed on ice or at 4 °C. The frozen samples from section 6.2.20 were rapidly thawed in a water bath at 30 °C. The cell suspension was sonicated on ice (Branson sonicator settings: duration 4 times for 1 min, 1 sec ON and 1 sec OFF, amplitude: 20 %). The lysate was then centrifuged for 20 min at 12000 xg and the pellet was resuspended in 20 mL histone wash buffer I containing 1 % Triton X-100 and was sonicated again with the same setting as previously described. The lysate was centrifuged again for 20 min at 12.000 xg. This was repeated two more times but with histone wash buffer I without Triton-X 100. After the last spin, the supernatant was discarded and the pellet was resuspended in 25 mL unfolding buffer 1. Histones were unfolded for 1 h at RT, rotating. After the unfolding, histones were centrifuged at 20.000 xg for 20 min at RT. The resulting supernatant was centrifuged again with the same conditions to remove any debris. The supernatant was further cleared through a 0.45 µm filter before it was loaded to a 50 mL super-loop. The sample was loaded twice onto a equilibrated (0.5 CV degassed ddH_2O, 1 CV SAU1000 buffer) HiPrep 26/60 Sepharyl S-200 HR column during two consecutive gel filtration runs that were performed in SAU1000 buffer at a flow rate of 1 mL/min overnight at RT while collecting 5 mL fractions. The next day, peak fractions were analyzed via SDS-PAGE and fractions containing solely truncated histone H4 were combined and loaded onto a 4 mL reversed-phase Resource RPC column via a sample pump. The column was then washed with 2 CV RPC buffer A. Samples were eluted in 2 mL fractions during a linear gradient over 20 CV from 0 to 65 % of RPC buffer A to RPC buffer B. The peak fractions were analyzed via SDS-PAGE and only fractions with truncated H4 were pooled and lyophilized. The dried protein was resuspended in ~10 mL ddH_2O before the concentration was calculated using OD280 measurements and the following formula: OD280/molar extinction coefficient (ε_{280}) *

molecular weight = µg/µl (ε_{280}: 5960, molecular weight: 8355.8) Aliquots of 1 mg were prepared, lyophilized and stored at -80 °C.

6.2.10. Ligation of truncated histone H4 and acylated peptide

Chemically synthesized and modified H4 peptides (amino acids 1-28) acylations were obtained commercially and were used to obtain full-length histone H4 site-specifically modified at lysine 16. A native chemical ligation approach was performed to ligate H4 peptides to purify truncated H4 (6.2.22). For this, 20 mg of TCEP was resuspended in 1 mL of degassed chemical ligation buffer. For the adjustment of the pH, 50 µL of 5 M KOH was added before the solution was degassed again. Then, 25 mg of MPAA was resuspended and the pH was again adjusted with 5 M KOH (final pH ~7.7). The solution was degassed. For one native chemical ligation reaction, 550 µL of the prepared ligation buffer was used to dissolve 1 mg of acylated H4 peptide and subsequently 4 mg of truncated histone H4. The ligation reaction was incubated at 40 °C overnight and was afterwards quenched with 60 µL 1 M DTT and 700 µL 0.5 % acetic acid. The mixture was then centrifuged at maximum speed for 10 min at 4 °C and the cleared supernatant was loaded and purified on an equilibrated reversed-phase chromatography column (4 mL C-8 Perkin Elmer Aquapore RP300 250x4.6 HPLC) at 4 °C. The column was washed with 2 CV buffer A, 1 CV to reach a 35 % gradient with buffer B and 2 CV of 35 % buffer B. Ligated H4 was eluted with a gradient of 35-45 % buffer B over 10 CV. 1 mL fraction were collected and peak fractions were analyzed via SDS-PAGE. Positive fractions were combined, lyophilized and stored at -80 °C.

6.2.11. Refolding of octamers

For the refolding of octamers, 0.5 mg of histone H2A, H2B, and H3.1 and 0.4 mg of ligated histone H4 (see 6.2.24) were separately dissolved in unfolding buffer to a concentration of 1 mg/mL. Histones were unfolded for 1 h rotating at RT and then pooled together. The histone mixture was transferred into a dialysis tubing (6-8 kDa MWCO) and dialyzed against three changes of 500 mL octamer refolding buffer (incubation for 3 h, overnight, and again for 3 h). The next day, the dialyzed sample was concentrated via centrifugal spin filtration unit (Sartorius Vivaspin 4 – 10 kDa MWCO/PES) to a final volume of ~400 µL. The concentrated sample was cleared twice via centrifugation at maximum speed for 10 min at 4 °C and the cleared supernatant was loaded on an equilibrated gel filtration column (Superdex-200 16/60 Prep Grade). Peak fractions were analyzed via SDS-PAGE and positive fractions (octamer with a

1:1:1:1 ratio of all histones) were combined. Octamers were stored at a concentration of 1 mg/mL in 50 % glycerol at -20 °C.

6.2.12. Nucleosome assembly

Nucleosomes were assembled via a salt gradient dialysis as described by Luger *et al* (1999). Mono-, di-nucleosomes, and 12-mer nucleosomal arrays were assembled in the presence of competitor DNA (so-called MMTV DNA). For an efficient assembly different ratios (0.8:1 to 1.4:1) of octamer:DNA were tested. 1x147 bp DNA (DNA origami) or 12x187 bp DNA (FRET-based array), competitor MMTV DNA and 5 M NaCl (final concentration 2 M) were mixed on ice and volumes were further adjusted with 1x TE (pH 7.5). Octamers were added and the solution was gently mixed. The mixture was transferred to dialysis buttons (3.5 kDa MWCO) and incubated in RB-high buffer for 30 min at 4 °C, stirring. A dual channel pump was then used for a continuous exchange of RB-high buffer against RB-low buffer over 1.6 L. The buffer exchange was performed for 24 h at a flow rate of ~1.1 mL/min. After 24 h, the samples were further dialyzed against 400 mL RB-low buffer for 4 h while stirring and were then transferred to siliconized tubes. The quality of assembled mono-nucleosomes was checked on a 5 % native PAGE. Assembled 12-mer nucleosomal arrays were checked on a 1.3 % agarose gel in 0.5x TBE buffer. For long-term storage nucleosomes were dialyzed overnight at 4 °C while stirring against 10 mM Tris (pH 7.5), 50 mM NaCl, and 1 mM EDTA.

6.2.13. DNA-origami force spectrometer

Mono-nucleosomes were assembled by using 2.65 µg of branched template DNA and 3.125-3.75 µg octamers following the protocol described in section 6.2.25. The assembly of the DNA-origami force spectrometer was performed as described in Funke *et al* (2017). The mono-nucleosomes and assembled DNA-origami force spectrometers were incubated in loading buffer at 4 °C overnight. The samples were loaded on glow-discharged formvar-supported carbon-coated Cu400 TEM grids and were stained using a 2 % aqueous uranyl formate solution containing 25 mM sodium hydroxide (pH 5). After imaging the particles with Philips CM100 electron microscope (set to 100 kV) at least 300 particles loaded with two mono-nucleosomes were analyzed per H4K16 modification. The opening angles of fully loaded DNA origami force spectrometers were measured using ImageJ. The probability distribution was normalized between 50°-90° before the free energy landscape was computed.

6.2.14. Nucleosomal stacking assay

12-mer nucleosomal arrays were assembled by Dr. Harsh Nagpal (EPFL, Lausanne, CH) using our H4K16 acylation containing octamers. Assembly and measurements were performed following the protocol published by Kilic *et al* (2018).

6.2.15. ACF purification

ACF was expressed in baculovirus-infected Sf9 insect cells and was purified as described in Peterson, 2009. For this, infected Sf9 insect cells were pelleted at 2000 xg for 5 min at 4 °C and the pellet was washed with ice-cold PBS. The pellet was resuspended in 8 mL of lysis buffer F and homogenized via douncing for three times every 10 min each time with 10 strokes on ice. The lysate was then centrifuged at 14500 xg for 10 min at 4 °C. The supernatant was diluted with dilution buffer F and 250 µL FLAG-M2 resin was added. The mixture was rotated at 4 °C for 4 h and then centrifuged at 775 xg for 3 min at 4 °C. The resin was resuspended in 12 mL wash buffer F and centrifuged again at 775 xg for 3 min at 4 °C. In total, this washing step was performed four times. 100 µL wash buffer F containing FLAG peptide and insulin (final concentration of 0.4 mg/mL for both) was added to the washed resin which was then incubated for 10 min on ice. The slurry was centrifuged for 30 sec at maximum speed and the elutant was transferred to a new tube. The elution was repeated two more times and all elutions were combined and aliquoted. Purified ACF was stored at -80 °C after snap freezing.

6.2.16. NAP1 purification

NAP1 was expressed in baculovirus-infected Sf9 insect cells and was purified as described in Peterson *et al* (2009). For this, infected Sf9 insect cells were pelleted at 2000 xg for 5 min at 4 °C and the pellet was washed once with ice-cold PBS. The pellet was resuspended in lysis buffer H to 1/40 of the original culture volume and was homogenized by sonication (Branson sonicator setting: duration: 3 times for 1 min, 0.5 sec ON and 0.5 sec OFF, amplitude: 50 %). After sonication, the sample was centrifuged at 15000 xg for 10 min at 4 °C. The collected supernatant was purified over a pre-equilibrated 5 ml HisTrap™ HP column (GE Healthcare, USA) which was connected to an Äkta™ pure. After loading the sample, the column was washed with 5 CV of lysis buffer H and 5 CV of wash buffer. NAP1 was eluted over 8.4 CV of elution buffer collecting 500 µL fractions. Peak fractions were analyzed on an 8 % SDS-PAGE gel followed by coomassie staining. Positive fractions were pooled and dialyzed overnight against 4 L of dialysis buffer. The next day, the sample was again dialyzed for 2 h against 4 L dialysis buffer and another 2 h against 4 L of NAP1 purification buffer

supplemented with 100 mM NaCl. After dialysis, the sample was collected and centrifuged at 20000 xg for 20 min at 4°C before the protein was quantified using BSA as a mass standard on an 8 % SDS-PAGE gel followed by coomassie staining. An appropriate amount of dialyzed protein was purified over a pre-equilibrated 6 ml Resource™ Q (GE Healthcare, USA) column connected to an Äkta™ pure. After loading the sample, the column was washed with 5 CV of NAP1 buffer supplemented with 200 mM NaCl. NAP1 was eluted over a linear gradient from NAP1 buffer supplemented with 200 mM NaCl to NAP1 buffer supplemented with 500 mM NaCl (gradient over 20 CV) and fractions of 500 µL were collected. Peak fractions were analyzed on an 8 % SDS-PAGE gel followed by coomassie staining. Only fractions containing no NAP1 inhibitor (14 kDa) in addition to NAP1 (65 kDa) were combined and dialyzed against two changes of 2 L NAP1 buffer plus 100 mM NaCl for 2 h each. After dialysis, the sample was centrifuged at 14500 xg for 15 min at 4°C. The protein concentration was quantified using BSA as mass standard on an 8 % SDS–PAGE gel followed by coomassie staining. The samples were snap-frozen in liquid nitrogen and stored at -80°C.

6.2.17. Chromatin assembly with NAP1 and ACF

For the *in vitro* transcription assay, regularly spaced chromatin was assembled with the histone chaperone NAP1 and the chromatin remodeling complex ACF. For one reaction with a final volume of 140 µL, HEG buffer containing 0.2 mM AEBSF, 2 mM NaBu, 1 mM DTT, and 100 ng/µL of BSA was prepared and 7 µL of 1 M KCl and 8 to 12 µL of histone octamers (stock: 100 ng/µL) were added. The optimal ratio between histone octamer and DNA concentration for an efficient chromatin assembly had to be determined by titration. The reaction was gently mixed before adding 2 µL of NAP1 (stock: 1.8 µg/ µL). The sample was gently mixed again and then incubated at RT for 30 min. Afterward, 4 µL of ACF (stock: 70 ng/µL), 16.8 µL of freshly prepared ATP-regenerating system, and 10 µL of plasmid DNA (stock: 100 ng/µL). The ATP-regenerating system was prepared as follows: 13.5 µL HEG buffer was mixed with 90 µL 500 mM of creatine phosphate, 1.5 µL of creatine phosphokinase (stock: 5 µg/µL), 45 µL of 100 mM ATP and 30 µL 250 mM $MgCl_2$. The chromatin assembly reaction was incubated for 3 h at 27 °C.

6.2.18. MNase digestion of *in vitro* assembled chromatin

The efficiency of assembled chromatin was tested via MNase digestion. For this, $CaCl_2$ was added to 200 µL of chromatin (corresponding to approximately 1.4 µg) to a final concentration of 2 mM. The sample was split into two 100 µL aliquots to which 6 or 30 mU MNase/µL in

5 µL HEG buffer were added. The samples were mixed and incubated at 30 °C for 10 min. The digestion was stopped by adding 110 µL of MNase stop buffer. The mixtures were incubated for 1 h at 37 °C before the DNA was extracted via phenol:chloroform and precipitated by ethanol. The resulting DNA pellet was resuspended in 15 µL of 1x DNA loading dye and electrophoresed in a 1.3 % unstained agarose gel. After separation, the gel was stained with 10 mg/mL ethidium bromide. For good-quality chromatin, a nucleosomal ladder with more than four nucleosomes was expected.

6.2.19. Sucrose gradient centrifugation of *in vitro* assembled chromatin

Efficiently assembled chromatin was further purified over a linear sucrose gradient ranging from 10 to 40 % sucrose. The sucrose gradient was generated by a peristaltic pump using a 5 % and a 40 % sucrose solution in a total volume of 5 mL. 400 µL of assembled chromatin were added carefully on top of the sucrose gradient cushion. The samples were centrifuged in an SW55Ti rotor (Beckman, USA) at 4 °C for 3 h at 48000 rpm. After 3 h, the run was stopped without any deceleration and the sample was fractionated into 300 µL aliquots. To 5 µL of each fraction, 1 % SDS and 1x DNA loading dye were added and the samples were run on a 1.3 % agarose gel in 0.5x TBE. The gel was stained afterwards with 10 mg/mL ethidium bromide. The same positive fractions for different chromatin samples were pooled together. Pooled samples were dialyzed against 2 L of BC50 buffer overnight at 4 °C. The next day, samples were concentrated via centrifugal spin filtration units (Sartorius Vivaspin 100 kDa MWCO/PES) to a final concentration of 7.14 ng/µL. Concentrated chromatin samples with different modifications were again run on a 1.3 % agarose gel in 0.5x TBE buffer and stained with 1 mg/mL ethidium bromide observe equal concentrations visually.

6.2.20. GAL4-VP16 purification

His-tagged GAL4-VP16 was expressed in the BL21 DE3 Gold strain. After transformation, the cells were plated on agar plates supplemented with ampicillin. The next day, a single colony was picked to inoculate an overnight culture of 50 mL LB supplemented with ampicillin at 37 °C. 1 L of LB supplemented with ampicillin was inoculated with ~25 mL overnight culture (initial OD600 < 0.1) and grown at 37 °C until OD600 reached 0.4-0.5. Expression of histones was induced with 0.5 mM IPTG and was continued for 3-3.5 h at 37 °C. Bacterial cells were collected for 5 min at 1000 xg at 4 °C and were washed with 20 mL ice-cold PBS. The pellet was then resuspended in 5x packed cell volume (PCV) of ice-cold 1x phosphate buffer supplemented with 20 mM imidazole. The bacteria suspension sonicated (Branson sonicator

setting: duration: three times for 1 min, 0.5 sec ON and 0.5 sec OFF, amplitude: 50 %). After the sonication, samples were centrifuged at 4 °C at 12000 xg for 10 min and the supernatant was filtered through a 0.45 µm pore size syringe filter before it was loaded on a pre-equilibrated 1 mL HisTrap HP column (GE Healthcare, USA). After loading the sample, the column was washed with 10 CV of 1x phosphate buffer supplemented with 20 mM imidazole. GAL4-VP16 was eluted with 5 CV of 1x phosphate buffer supplemented with 500 mM imidazole and 500 µL fractions were collected. Peak fractions were analyzed on a 12.5 % SDS-PAGE gel and only fractions containing purified GAL4-VP16 were pooled. The sample was then dialyzed against 2 L of 1x PBS using a peristaltic pump over 16 h at 4 °C. The next day, the sample was again dialyzed against 2 L of GAL4-VP16 storage buffer before it was centrifuged at 10000 xg for 10 min at 4 °C. The supernatant was aliquoted, snap-frozen, and stored at -80 °C. The protein concentration was quantified on a 12.5 % SDS–PAGE gel using BSA as mass standard followed by coomassie staining

6.2.21. P300 purification

His-tagged p300 was expressed in baculovirus-infected Sf9 insect cells. 250 mL infected Sf9 insect cells were pelleted at 400 xg for 5 min at 4 °C and the pellet was washed twice with 25 mL ice-cold PBS. The pellet was resuspended in 2.5 ml of buffer B and homogenized by douncing using an “A” pestle with 10 strokes. The homogenized sample was incubated for 15 min on ice and the 700 - 800 µL aliquots were prepared. Aliquoted samples were sonicated (Qsonica setting: duration: 3 times for 5 min, 30 sec ON and 30 sec OFF, amplitude: 90 %). Aliquots were again combined and centrifuged at 16000 xg for 15 min at 4 °C. The supernatant was loaded on a pre-equilibrated 1 ml HisTrap™ HP column (GE Healthcare, USA) connected to an Äkta™ pure. After loading the sample, the column was washed with 5 CV of buffer B and p300 was eluted with 10 CV elution buffer. During elution, 500 µL fractions were collected and peak fractions were analyzed on a 4-12% gradient SDS–PAGE gel followed by coomassie staining. Positive fractions were pooled and the sample concentration was measured by Bradford assay. The samples were diluted with 50% glycerol, aliquoted, snap-frozen, and stored at -80°C.

6.2.22. Nuclear extraction for affinity purification and IVT

Hela S3 spinner cells were grown to a density of at least $1x10^6$ cells/mL and were collected by centrifugation at 500 xg for 10 min at 4 °C. The pellet was washed twice with ice-cold PBS (10 mL/L of culture) and was then resuspended with 5 PCV of buffer A and incubated on ice

for 10 min. The sample was then centrifuged at 750 xg for 10 min at 4 °C and the pellet was resuspended with 2 PCV of buffer A. The cell suspension was then homogenized and lysed by douncing with a tight-fitted pestle for 10 strokes. Cell lysis efficiency was observed under the microscope and douncing was repeated until at least 70 % of cells were lysed. The lysed cells were then centrifuged at 10000 rpm for 20 min at 4 °C. The supernatant was decanted and any traces of lipids were removed with a pipette. The nuclear pellet was centrifuged at 25000 xg for 20 min in order to remove any traces of residual cytoplasmic material. The nuclear pellet was resuspended in buffer C (3 mL per $1x10^9$ cells). The nuclei were extracted by gentle stirring for 30 min on ice. The suspension was then centrifuged at 25000 xg for 20 min at 4 °C and the supernatant was transferred to a new tube. The nuclear extract was dialyzed for 50 volumes of buffer D for 5 h at 4 °C. The dialyzed sample was centrifuged for 20 min at 25000 xg. The supernatant was aliquoted and snap-frozen in liquid nitrogen. The nuclear extract aliquots were stored at -80 °C. For peptide-based affinity purifications, the protein concentration was measured by Bradford assay.

6.2.23. *In vitro* transcription (IVT) assays

For one IVT reaction, 7 µL of assembled and purified chromatin (~ 50 ng) were mixed with 1 µL purified GAL4-VP16 (stock: 50 ng/µL), 7.2 µL c-mix and 6 µL BC100. The mixture was incubated for 15 min at RT. 1 µL of purified p300 (stock: 120 ng/µL) and 1 µL of the ac-CoA/NaBu mix was added and the sample was further incubated for 30 min at 30 °C. Then, 10 µL of HeLa nuclear extract was added and the mixture was again incubated for 30 min at 30 °C. 3 µL of rNTPs containing radioactively labeled rUTP-32P (Perkin BLU007H; Perkin-Elmer, USA) were added to the mixture and the reaction was incubated for 40 min at 30 °C before the reaction was quenched with 6 µL of rUTPs. The sample was incubated for 20 min at 30 °C and then 150 µL stop mix was added. Under a fume hood, 200 µL of phenol-chloroform was added to each reaction and the samples were mixed by inversion for five times. The samples were centrifuged for 5 min at maximum speed and the aqueous upper phase (~180 µL) was transferred to an RNase-free tube. The same volume of absolute ethanol was added and the sample was again mixed by inversion. The sample was then loaded on to an RNA cleanup column from the Monarch® RNA Cleanup kit (10 µg) and the manufacturer's protocol was followed. The RNA was eluted in 12 µL nuclease-free water and 3 µL of 6x loading buffer was added. The samples were boiled for 95 °C for 5 min and were then electrophoresed through an urea-denaturing gel for 1 h at 130 V. The gel was then dried for 50 min at 80 °C. The dried gel was used to expose a phosphor screen at RT overnight. The exposed screen was analyzed via

the Amersham Typhoon 5 Biomolecular Imager (GE Healthcare, USA) and the signals were quantified by ImageQuant™ TL.

6.2.24. Coupling of H4 peptides to agarose beads

Chemically synthesized H4 peptides (stock: 5 mg/mL) were diluted with coupling buffer containing 50 mM TCEP to a final concentration of 1.5 mg/mL in 1 mL. 1 mL of SulfoLink™ Coupling Resin was washed three times with 1 mL coupling buffer before the diluted peptides were added to the beads. The peptides were coupled to the beads for 1 h, rotating at RT. The mixture was then centrifuged for 1 min at 2000 xg. After removing the supernatant, 1 mL of 50 mM L-cysteine solution was added to the beads and the beads were blocked for 1 h while rotating at RT. The beads were then washed three times with 1 mL 1M NaCl and three times with 1 mL 1x TBS/ 5 mM EDTA. The beads were stored in 1 mL of degassed 1x TBS/ 5 mM EDTA, 0.05 % NaN_3 at 4 °C.

6.2.25. Peptide-based affinity purification

20 µL (for MS analysis) or 50 µL (for immunoblotting) of beads coupled to H4 peptides were washed twice with 1 mL buffer A and were centrifuged at 2000 xg for 2 min at 4 °C. 500 µg (for MS analysis) or 1.25 mg (for immunoblotting) of HeLa nuclear extract were added to the washed beads and 150 mM NaCl containing dilution buffer was added for a final volume of 600 µL. The affinity purification was performed for 1.5 - 4 h at 4 °C on a rotating wheel. The beads were then washed three times with 1 mL 350 mM NaCl containing dilution buffer and twice with PBS. For immunoblotting, 35 µL 2x Laemmli buffer was added and the samples were boiled for 5 min while shaking at 95 °C. For MS analysis, the beads were resuspended in 50 µL elution buffer and the slurry was incubated for 15 min shaking at RT. IAA was then added for a final concentration of 50 mM and the mixture was incubated for 10 min shaking at RT in the dark. 2.5 µL trypsin was added and the sample was digested for 1 h on a shaker at RT. The sample was then centrifuged for 2 min at 1500 xg and the supernatant was collected. The beads were again resuspended in 50 µL elution buffer and incubated for 5 min at RT while shaking. The sample was centrifuged for 2 min at 1500 xg and the supernatants were combined. 1 µL of trypsin was added to the combined supernatants and the digestion was performed overnight at RT. The next day, the digestion was stopped with 5 µL TFA and the peptides were then purified on C18 stage tips. The analysis of interacting proteins via MS identification was performed as previously described (Vermeulen, 2012).

6.2.26. Antibody purification

For the generation of anti-H4K16pr and anti-H4K16bu antibodies, rabbits were immunized with the H4K16pr or H4K16bu peptide according to the immunization protocol from BioGenes GmbH (Germany). First, rabbit serum was purified by the addition of EDTA to a final concentration of 5 mM and centrifugation for 20 min at 10000 xg at 4 °C. Cleared serum was used to purify specific antibodies using H4 peptides coupled to beads (slurry). Purification strategies for various antibodies are listed in Table 6.2. All depletion or purification steps were performed at RT for 2 h while rotating. For the purification, beads were washed three times with 1 mL TBS/5 mM EDTA for 5 min at RT while rotating. Antibodies were eluted from beads by the addition of an equal volume of 0.1 M glycine (pH 2.5) and shaking for 2 min at 1000 rpm (RT). The sample was centrifuged for 1 min at 2000 xg and the supernatant was transferred to a pre-cooled tube and neutralized with 1 M Tris-HCl (pH 9.5) for a final concentration of 55 mM. In total, the elution was repeated three times and all eluates were combined.

Table 6.2: Purification of H4K16 acylation-specific antibodies.

Epitop	Internal ID	Purification
H4K16pr	#1	1:10 (v/v) H4K16pr slurry and 40 nM free H4K16un/ac/bu peptide
	#4	1:10 (v/v) H4K16pr slurry and 40 nM free H4K16un/ac/bu peptide
	#69	Depletion of serum with 1:10 (v/v) H4K16un slurry Depleted serum: 1:20 (v/v) H4K16pr slurry and 40 nM free H4K16bu peptide
H4K16bu	#104	1:10 (v/v) H4K16bu slurry and 40 nM free H4K16un/ac/pr peptide

6.2.27. Peptide immunoblotting

In order to test the specificity of antibodies targeting various histone acylations, peptide immunoblotting was performed. Serial dilutions (1:5) of unmodified or differently modified chemically-synthesized H4 peptides (amino acids 11-20) were spotted on a 0.1 µm pore size nitrocellulose membranes. Membranes were air-dried for at least 30 min at RT. Immunostaining of these blots was performed as described in 6.2.3.

6.2.28. Immunofluorescence of MEFs

Immortalized mouse embryonic fibroblasts (MEFs) were grown in one well of a 6-well plate containing one coverslip (diameter: 18 mm) until reaching a confluency of ~90 %. Cells were then fixed in 4 % PFA in 1x PBS for 10 min at RT and permeabilized with 0.6 % Triton X-100 in 1x PBS for 20 min at RT. Cells were further washed once with 4 % BSA in 1x PBS at RT before they were blocked in 4 % BSA- 0.2 % Tween in 1x PBS for 1 h at RT. After blocking, the primary antibody in 4 % BSA- 0.2% Tween in 1x PBS overnight at 4 °C in a humid chamber. The next day, cells were washed three times in 4 % BSA in 1x PBS at RT before they were incubated with the secondary antibody in 4 % BSA- 0.2 % Tween in 1x PBS for 1 h at RT in a humid chamber in the dark. Cells were then washed three times with 4 % BSA in 1x PBS at RT, once with 1x PBS, and once with H_2O. Coverslips were mounted in vectashield containing DAPI and sealed with nail varnish. Cells were observed on a Confocal Laser Scanning Microscope TCS SP8 (Leica) using a 63x objective.

6.2.29. Immunofluorescence of hHSCs

This staining was performed by Dr. Amanda Amoah following the protocol from Grigoryan *et al* (2018). In short, freshly sorted HSCs were seeded on fibronectin-coated glass coverslips and incubated for 12-16 h. Cells were fixed via BD Cytofix Fixation Buffer (BD Biosciences). Fixed cells were washed with PBS and permeabilized for 20 min with 0.2 % Triton X-100 in PBS. Cells were blocked for 30 min with 10 % donkey serum at RT. Primary and secondary antibody incubations were performed for 1 h at RT. Coverslips were mounted with ProLong Gold Antifade Reagent containing DAPI (Invitrogen, Molecular Probes). For imaging a LSM710 confocal microscope (Zeiss) equipped with a ×63 objective was used. Images were analysed and converted into 3D images with the Volocity Software (Version 6.2, Perkin Elmer).

6.2.30. Crosslinked (X-) ChIP

HEK293 cells were grown on 15 cm dishes until they reached a ~80 % confluency and were directly crosslinked with formaldehyde (final concentration of 1 %). After a 5 min incubation at RT, the fixation was quenched with glycine (final concentration of 125 mM) for 5 min shaking at RT. The cells were washed three times with ice-cold PBS and collected by scrapping in PBS supplemented with 1x protease inhibitor cocktail and the appropriate HDAC inhibitors. All following steps were carried out on ice unless indicated otherwise and buffers were all supplemented with 1x protease inhibitor cocktail and the appropriate HDAC inhibitors.

Collected cells were centrifuged at 500 xg for 5 min at 4 °C. Cell pellet was resuspended in 1 mL per 15 cm dish of L1 buffer on ice for 5 min. The samples were then centrifuged at 800 xg for 5 min at 4 °C. The pellet was resuspended in 1 mL of L2 buffer per 15 cm dish. Next, chromatin was fractionated by sonication (Qsonica settings: 80 % amplitude, 20 sec ON, 40 sec OFF, total time: 15 min). After sonication, the samples were centrifuged at 14000 xg for 10 min at 4 °C. The supernatant, containing the chromatin, was transferred to a new 1.5 mL tube. Chromatin concentration was measured by using the Qubit dsDNA HS Assay kit and diluted with dilution buffer to 150 ng/µL. To check the sonication efficiency, 100 µL of diluted sample were mixed with 80 µL of L2 buffer and 8.4 µL of 5 M NaCl and incubated at 65 °C overnight. The remaining sample was stored on ice. For the pre-blocking of the beads, a mixture of 500 µL of protein A agarose beads and 500 µL of protein G agarose beads (GE Healthcare, USA) were washed three times with 1 mL 1x TE and incubated overnight at 4 °C with 100 µL of pre-boiled single stranded salmon sperm DNA (10 mg/mL) and 100 µL of 10 mg/ mL BSA. On the following day, the beads were washed three times with 1 mL 1x TE and stored as a 50 % slurry in 1x TE. Efficiently sonicated chromatin was pre-cleared by diluting 40 µg of chromatin (per IP) with dilution buffer (supplemented with the appropriate HDAC inhibitors) to a final volume of 1 mL. The samples were then incubated for 1 hour at 4 °C on a rotation wheel with 20 µL of pre-blocked agarose bead-slurry. After incubation, the samples were centrifuges for 5 min at 1000 xg. Antibodies were added to the pre-cleared supernatant and the samples were incubated overnight at 4 °C on a rotation wheel. On the next day, 50 µL of pre-blocked agarose bead-slurry were added to each IP and incubated for 3 h at 4 °C on a rotation wheel. The beads were washed two times with 1 mL of washing buffer. After the last wash, the samples were resuspended in 150 µL of elution buffer and incubated for 10 min at RT on a rotation wheel. The samples were centrifuged for 1 min at 4000 rpm. The supernatant was collected and this step was repeated one more time. The two supernatants were pooled together. To each sample 12 µL of 5 M NaCl and 1.56 µL of RNase A (10 mg/mL) were added and the samples were incubated for 30 min at 37 °C. Next, 1 µL of proteinase K (20 mg/mL) was added to each sample and incubated for 4 to 5 h at 65 °C. DNA was purified with QIAquick PCR Purification kit according to the manufacturer's instructions.

6.2.31. Crosslinked MNase (X-MNase) ChIP

HEK293 cells were grown on 15 cm dishes until they reached a ~80 % confluency. To 10 mL of cell medium, 1 mL of 10x fixing solution containing formaldehyde was added. Cells were fixed for 8 min at RT. Freshly prepared glycine was added to a final concentration of 125 mM.

The cells were washed three times with ice-cold PBS and collected by scrapping in PBS supplemented with 1x protease inhibitor cocktail and the appropriate HDAC inhibitors. The samples were centrifuged at 800 xg for 5 min at 4 °C. The cell pellet was resuspended 0.5 % Triton X-100 in PBS ($1x10^7$ cells/ mL) and the mixture was rotated for 15 min at 4 °C. The cells were centrifuged for 10 min at 1000 xg at 4 °C. Cells were washed with 1 mL PBS and centrifuged again for 10 min at 1000 xg at 4 °C. The cell pellet was then resuspended in RIPA buffer ($1x10^7$ cells/ mL) and snap-frozen in liquid nitrogen. Aliquots of 500 µL were prepared and 1 µL or 2.5 µL MNase was added. The sample was digested for 35 min at 37 °C shaking (1000 rpm). 22 µL of 0.5 M EGTA were added to the digested sample on ice. The sample was then sheared by the Covaris sonicator (12x12 fibre tube, 50 W, 8 min, 20 %). The sonicated sample was centrifuged for 20 min at 4 °C at maximum speed. 12.5 µL Protein A Sepharose® and 12.5 µL Protein G Sepharose® beads were mixed in 1 mL RIPA buffer. Beads were washed with RIPA buffer, rotated for 30 min at 4 °C and collected via centrifugation at 500 xg for 1 min at 4 °C. Beads were mixed in 225 µL RIPA buffer and 200 µL of chromatin (~ 80 µg) was added. The total volume was adjusted to 650 µL with RIPA buffer. Chromatin was pre-cleared for 3h at 4 °C while rotating. Beads were centrifuged for 500 xg for 1 min at 4 °C and the supernatant containing the chromatin was transferred to new low-binding tubes. 50 µL of chromatin was used as input material (10 %) and kept on ice. Antibodies were added to the remaining chromatin and the IP was performed overnight at 4 °C while rotating. 500 µL of the antibody chromatin mixture was added to equilibrated beads and the sample was rotated for 3 h at 4 °C. The beads were then washed four times with RIPA buffer. 10 % input and washed beads were then diluted with 1x TE to a final volume of 100 µL and were incubated overnight at 65 °C shaking at 1000 rpm. The next day, 1 µg RNAse A was added and the samples were incubated for 30 min at 37 °C. 5 µL 10 % SDS and 1 µg proteinase K were added and the samples were incubated for 1.5 h at 55 °C. The DNA was then purified via AmpureXP bead following the manufacturer's protocol (1.8x volume of beads) and eluted in 15 µL elution buffer. DNA was stored at -20 °C.

6.2.32. CUT&RUN

Cleavage Under Targets & Release Using Nuclease (CUT&RUN) is a recently established alternative for traditional ChIP approaches and can be compared to native ChIP. During CUT&RUN non-fixed cells are permeabilized and incubated first with a target antibody and then with a pA-MNase (Protein A-Micrococcal Nuclease) which will interact with antibodies and release chromatin fragments. We followed the protocol as published by Janssens &

Henikoff (2019). Briefly, $1x10^5$ MEFs were harvested per sample and washed two times with 1 mL wash buffer. Cell pellets were resuspended in 1 mL wash buffer and 10 µL ConA-coated magnetic beads were added. Cells were bound to beads during rotation for 10 min at RT. Samples were then placed on a magnetic stand and the supernatant was removed. 150 µL antibody buffer was added to the beads and mixed while gently vortexing before adding the primary antibody. Samples were placed on a tube rotator and rotated for 2 h at 4 °C. Beads were then washed once with 300 µL Dig-wash buffer and 150 µL pA-MNase (at a concentration of 700 ng/mL in Dig-wash buffer) was added. Samples were placed on a tube rotator and rotated for 1 h at 4 °C. Beads were washed twice with 300 µL Dig-wash buffer. Beads were resuspended gently in 100 µL Dig-wash buffer and placed on ice. 2 µL of pre-cooled 100 mM $CaCl_2$ was added to the beads while gently vortexing and incubated for 30 min at 4 °C. After the digestion, 100 µL 2x stop buffer were added and incubated for 30 min at 37 °C for the release of CUT&RUN fragments. Samples were placed on a magnetic rack and supernatant containing released chromatin fragments was transferred to a new tube. Released chromatin was purified by the QIAquick PCR Purification kit following the manufacturer's instructions. The DNA was eluted with 30 µL H_2O and quantified via Qubit dsDNA HS kit following the manufacturer's protocol.

6.2.33. Native (N-) ChIP for cells

$1x10^6$ HEK293 cells or mESCs were used for one IP. Described volumes can be upscaled corresponding to the IPs that need to be performed. All steps until the addition of RNase A were carried out on ice/ at 4 °C. Appropriate HDAC inhibitors and protease inhibitors were freshly added to used buffers. $1x10^6$ cells were collected and pelleted at 500 g for 3 min. Cells were washed two times with 200 µL of ice-cold 1x PBS. Cells were then resuspended in 100 µL ice-cold NBA buffer. 100 µL NBB buffer was added to the mix and further incubated for 3 min on ice. The sample was then centrifuged for 3 min at 1000 xg. The pellet, containing now nuclei, was resuspended in 200 µL NBR buffer and centrifuged for 3 min at 2000 xg. The nuclear pellet was resuspended in 60 µL NBR and 10 µg RNase A was added. After a 5 min incubation at RT, 4U MNase was added and gently mixed by pipetting. MNase digestion was performed for 10 min at 20 °C. After 5 min, the sample was mixed by pipetting. The digestion was quenched by adding 60 µL stop buffer and diluted with a 1:1 NBR:stop buffer mix for a final volume of 200 µL. The sample was then incubated overnight on ice and pre-cleared the next day for 5 min at maximum speed at 4 °C. For the IP, 5 µL of Protein A and 5 µL Protein G beads were mixed and washed twice with 400 µL block solution. 10 µL of slurry was finally mixed with 600 µL

block solution and 1 µg of antibody. Antibodies were bound to the beads for 2 h, rotating at 4 °C. Beads were then washed once with 200 µL block solution. 200 µL of diluted and pre-cleared chromatin were added to the beads and incubated for 3 h rotating at 4 °C. Afterwards, beads were washed three times with 1 mL ice-cold ChIP W1 washing buffer. An additional washing step with 1x TE was performed at RT. 100 µL of elution buffer was then added to the beads. The mixture was shortly vortexed and then incubated for 15 min at 37 °C (shaking at 400 rpm). In order to adjust the pH of the sample, 7 µL of 1 M Tris-HCl (pH 6.8) was added. 20 µg of Proteinase K were mixed to the sample which was incubated overnight at 55 °C. The next day, the beads were removed from the sample via a magnetic rack, and the IPs were purified QIAquick PCR Purification kit. The DNA was eluted with 20 µL H_2O and quantified via Qubit dsDNA HS kit following the manufacturer's protocol.

6.2.34. Native (N-) ChIP for tissue

10 mg to 30 mg of liver were added to 1 mL ice-cold buffer 1 supplemented with appropriate HDAC inhibitors and protease inhibitors in a tight homogenizer. Homogenization was performed by manual douncing (~ 20 times). Homogenized material was diluted to a final volume of 4 mL of ice-cold buffer 1. The cell suspension was centrifuged at 6000 xg for 10 min at 4°C. The supernatant was poured off and the cells were resuspended in 500 µL ice-cold buffer 1. 500 µL pre-cooled buffer 2 was added and after gently mixing the sample was incubated for 3 min on ice. After centrifuging the sample for 3 min at 3000 xg the nuclei pellet was washed with 1 mL of ice-cold NBR buffer and centrifuged as before. The pellet was then re-suspended in 200 µL NBR to which 10 µg RNaseA was added. The mixture was incubated for 5 min at RT. 1 U of MNase (Sigma, Boehringer units; 1U for 2M cells) was added and gently mixed by pipetting. MNse digestion was performed for 15 min at 20 °C. The sample was gently mixed by pipetting after 7 min. The reaction was stopped by adding 200 µL Stop buffer. A 1:1 NBR:Stop buffer solution was added to the sample for a final volume of 3 mL. The chromatin was released overnight on ice. The next day, the released chromatin was cleared by centrifugation for 10 min at maximum speed, 4 °C. All the following steps were performed as described in the previous section.

6.2.35. Library preparation for ChIP-seq

Libraries for ChIP-seq samples were prepared with the NEBNext Ultra II DNA Library Prep kit following the manufacturer's instructions using 5-10 ng of fragmented DNA diluted in 0.1x TE. After adaptor ligation, adaptor-ligated DNA was cleaned up without size selection. For the

PCR enrichment of adaptor-ligated DNA, 6-8 cycles of denaturation and annealing/ extension were performed. Purified PCR reactions were analyzed on the BioAnalyzer using an HS DNA chip. Library size was further optimized following the instructions of SPRIselect User Guide using a double size selection approach (0.85-0.56). For the elution of size-selected fragments, 25 µL of 1x TE was added to the AmpureXP beads. After mixing the beads and an incubation at RT for 2 min, tubes were placed on a magnetic rack and 22 µL were transferred to a new tube. The size selection of samples was controlled via BioAnalyzer measurements using a HS DNA chip. Optimal samples were then pooled in equimolar ratios for a final pooled library concentration of 5 nM. Libraries were submitted to the HMGU sequencing facility for 50 bp paired-end sequencing on the Illumina 4500. Total reads ranged from 25-40x10^6 reads.

6.2.36. ChIP-seq analysis

Paired-end sequencing reads (150 bp) were mapped to the reference genome (Mus musculus GRCm38 dna primary assembly) using bowtie2 (version 2.3.5). Reads were filtered by samtools (version 1.3.1) with parameter -q 12. ChIP-seq peaks were called using Homer (version 4.10) findPeaks with parameters -style histone -fragLength 150 -inputFragLength 150. Peaks were annotated with Homer annotatePeaks. Downstream analyses and visualizations were carried out in R (version 3.6.1) using functions from tsTools (https://github.com/musikutiv/tsTools) and HelpersforChIPSeq packages (https://github.com/tschauer/HelpersforChIPSeq). Differential analysis was performed by DESeq2 (version 1.26) on reads counted in 4 kb windows surrounding transcription start sites (TSS). DESeq2 size factors were calculated on read counts in 100 kb non-overlapping genomic bins. Significant differentially marked TSSs were defined by an adjusted p-value cutoff of 0.05. When comparing $\log_2$ fold changes of ChIP-seq counts in groups of up-, down- or non-significant differentially regulated genes in RNA-seq, an adjusted p-value cutoff 0.1 was used for grouping genes in RNA-seq.

6.2.37. Acyl-Coa measurements via MS

Acyl-CoA measurements were performed by Dr. Michael Witting. In short, metabolites were extracted from cell pellets or tissue powder using 1mL of cold $CHCl_3$/MeOH/H_2O (1/3/1, v/v/v). After suspension in the solvent, the samples were transferred to 2 mL MN Bead Tubes Type A (Macherey-Nagel, Düren, Germany). Samples were lysed using a Precellys Bead Beating system connected to a Cryolys cooling module (Bertin Instruments, Montigny-le-Bretonneux, France). The sample was then incubated for 10 min in an ice-cold ultrasonic bath

and was centrifuged for 15 min at 13000 rpm and 4 °C. The supernatant was transferred to a new tube and was dried via a centrifugal evaporator. From the residual cell debris pellet, proteins were quantified using a BCA kit. Metabolite profiling was performed using a Sciex Exion AD LC coupled to a Sciex X500R Q-ToF-MS under control of Sciex OS 1.7.0.36606 (Sciex, Darmstadt, Germany) and the separation was achieved on an Agilent InfinityLab Poroshell 120 HILIC-Z column (2.1 mm x 150 mm, 2.7 µm particle size, PEEK-lined) (Agilent Technologies, Waldbronn, Germany). Eluent A consisted of 10 mM ammonium formate in water with 0.1 % formic acid and eluent B of 10 mM ammonium formate in water/ACN (10/90, v/v) with 0.1 % formic acid. Gradient conditions were as followed: 2/98 at a 0 min, 2/98 at 3 min, 30/70 at 11 min, 40/60 at 12 min, 95/5 at 16 min, 95/5 at 18 min, 2/98 at 19 min and 2/98 at 20 min. The flow was set to 0.25 mL/min and the column temperature to 25 °C. After separation, the column was re-equilibrated for 4 minutes. Dried samples were re-dissolved in 50 µL $CHCl_3$/MeOH/H_2O (1/3/1, v/v/v) and 40 µL were transferred to an autosampler vial and 10 µL to a pooled QC sample. Autosampler temperature was set to 5°C and 0.5 µL was injected for analysis in positive ionization mode. The spray voltage was set to 5500 V and a declustering potential of 50 V was used. In MS1 ion in the m/z range from 50-1000 were accumulated for 0.1s and information-dependent acquisition of MS2 was used with a maximum number of 6 candidate ions and a collision energy of 35V with a spread of 15 V. Accumulation time for MS2 was set to 0.025 s yielding a total cycle time of 0.299s. QC samples were used for conditioning of the column and were also injected every 10 samples. Automatic calibration of the MS in MS1 and MS2 mode was performed every 5 injections using ESI positive Calibration Solution for the Sciex X500 system (Sciex, Darmstadt, Germany). Data analysis was performed in Sciex OS 1.7.0.36606 (Sciex, Darmstadt, Germany). Peaks for CoA, Acetyl-CoA, Propionyl-CoA, and butyryl-CoA were integrated with a XIC width of 0.02 Da and a gaussian smooth width of 3 points using the MQ4 peak picking algorithm. The identity of peaks was confirmed using authentic standards of all substances and comparison against reference spectra. Peak areas were exported to a .txt file and normalized according to the protein content of the respective sample.

6.3. Animal experiments and cell culture methods

6.3.1. Cell culturing

In general, cells were maintained at 37 °C in a humidified atmosphere containing 5 % CO_2. MEF and HEK293 cells were grown in high-glucose DMEM supplemented with 10 % fetal bovine serum, 2 mM L-glutamine, 100 U/mL penicillin, and 0.1 mg/mL streptomycin. Mouse

ES cells were cultured in high-glucose DMEM supplemented with 15 % FBS, 100 U/mL penicillin, 0.1 mg/mL streptomycin, 1 % non-essential amino acids, 0.1 mM ß-mercapto-ethanol, 2x LIF and 2i (final concentration of 25 ng/mL of PD 0325901 and 75 ng/mL of CHIR 99021). Hela S3 spinner cells were maintained in RPMI media supplemented with 5 % NCS, 2 mM L-Glutamine (200 mM) and 100 U/mL penicillin, and 0.1 mg/mL streptomycin. Human HSCs were incubated at 37 °C in a humidified atmosphere containing 5 % CO_2 and 3 % O_2 in HBSS and 10 % FBS in growth factor-free medium cells.

6.3.2. Mice

Mice from the C57BL/6J strain were used for the HFD experiments which were performed by Dr. Raian E. Contreras (HMGU, München, DE) with approval by the State of Bavaria, Germany. Mice were either fed with standard Chow diet (Altromin, #1314) or with a 58 % high-fat diet (HFD) for 15 weeks (Research Diets, D12331).

WT and hypomorphic *Pcca*$^{-/-}$ (A138T) mice (FVB background) were maintained by Dr. Alejandro Fulgencio Covián (Universidad Autónoma de Madrid, Spain, ES). Mice were maintained on standard chow and sacrificed at the age of 5 months. All the experiments were carried out in a pathogen-free environment at the Animal Facility of Centro de Biología Molecular Severo Ochoa, in accordance with the Spanish Law of Animal Protection.

7. Abbreviations

7.1. General abbreviations

4-OHT	4-hydroxytamoxifen
Ac	Acetylated
ACAD	Acyl-CoA dehydrogenase
ACF	ATP-utilizing chromatin assembly and remodeling factor
AcKRS	Acetyl-lysyl-tRNA synthetase
ACLY	ATP-citrate lyase
ACSS2	Acyl-CoA synthetase short-chain family member 2
ACSS3	Acyl-CoA synthetase short-chain family member 3
ADD	ATRX-DNMT3-DNMT3L
AID	Auxin-inducible degron
αKG	α-ketoglutarate
BD	Bromodomain
BET	Bromodomain and extraterminal domain
BRCT	BRCA1 carboxy-terminal
Bu	Butyrylated
Cdc42	Cell division control protein 42
cDNA	Complementary DNA
ChIP-seq	Chromatin immunoprecipitation followed by next generation sequencing
CRAT	O-acetyltransferase
CUT&RUN	Cleavage under targets & release using nuclease
CV	Column volume
DNA	Deoxyribonucleic acid
DPF	Double PHD finger
E. coli	*Escherichia coli*
ECL	Enhanced chemiluminescent
E_{FRET}	FRET efficiency
FBS	Fetal bovin serum
FRET	Förster resonance energy transfer
GNAT	GCN5-related N-acetyltransferase
HAT	Histone acetyltransferase
HDAC	Histone deacetylase
HEK	Human embryonic kidney
HFD	High-fat diet

HRP	Horseradish peroxidase
HSC	Hematopoietic stem cell
IDR	Intrinsically disordered region
IGV	Integrative Genomics Viewer
ImmunoFISH	Fluorescence in situ hybridization
IP	Immunoprecipitation
IVT	*In vitro* transcription
Kac	Lysine acetylation
Kbhb	Lysine β-hydroxybutyrylation
Kbu	Lysine butyrylation
Kbz	Lysine benzoylation
Kcr	Lysine crotonylation
Kd	Dissociation constant
Kglu	Lysine glutarylation
Khib	Lysine 2-hydroxyisobutyrylation
Kla	Lysine lactylation
Kmal	Lysine malonylation
KO	Knockout
Kpr	Lysine propionylation
Ksucc	Lysine succinylation
LB	Lysogeny broth
LC-MS/MS	Liquid chromatography tandem mass spectrometry
LLPS	Liquid-liquid phase separation
MBT	Malignant Brain Tumor
MCAD	Medium-chain acyl-CoA dehydrogenase
MEF	Mouse embryonic fibroblast
mESC	Mouse embryonic stem cell
MLP	Major late promoter
MOF	Males absent on the first
MS	Mass spectrometer
MSL	Male-specific lethal
MW	Molecular weight
MYST	MOZ, YBF2/SAS3, SAS2 and TIP60
N-ChIP	Native ChIP
NAD+	Nicotinamide adenine dinucleotide
NAGS	N-acetylglutamate synthase

NAP1	Nucleosome assembly protein 1
NCL	Native chemical ligation
NCP	Nucleosome core particle
ncRNA	Non-coding RNA
NGS	Next generation sequencing
NSL	Non-specific lethal
OAA	Oxaloacetic acid
OAADPr	O-acetyl-ADP-ribose
OD	Optical density
PA	Propionic acidemia
pA-MNase	Protein A-Micrococcal Nuclease
PCC	Propionyl-CoA carboxylase
Pcca	Propionyl-CoA carboxylase alpha subunit
PCR	Polymerase chain reaction
PCV	Packed cell volume
PDC	Pyruvate dehydrogenase complex
PHD	Plant homeodomain
Pr	Propionylated
PTM	Post-translational modifications
qPCR	Quantitative PCR
RIN	RNA integrity number
RNA	Ribonucleic acid
rNTPs	Ribonucleotides
ROS	Rreactive oxygen species
RT	Room temperature
SCAD	Short-chain acyl-CoA dehydrogenase
SCAF	Short-chain fatty acid
SDS-PAGE	Sodium Dodecyl Sulfate Polyacrylamide Gel Electrophoresis
STD	Standard deviation
TCA	Tricarboxylic acid
TF	Transcription factor
tRNA	Transfer RNA
TSS	Transcriptional start site
TTS	Transcriptional termination site
Un	Unmodified
WAT	White adipose tissue

WT	Wild type
X-ChIP	Crosslinking ChIP
YEATS domain	Yaf9, ENL, AF9, Taf14 and Sas5

7.2. Units abbreviations

A	Amperes
Au	Absorbance unit
bp	Basepair
°C	Degree Celsius
Da	Dalton
g	Gram
k	Kilo
kcal/mol	Kilocalorie per mole
L	Liter
m	Mili
µ	Micro
m	Meter
M	Molar
min	Minutes
n	Nano
p	Pico
rpm	Rotations per minute
RPM	Reads per million
sec	seconds
U	Units
V	Volts
v/v	Volume per volume
w/v	Weight per volume
xg	Times gravity

8. Acknowledgments

I would like to first thank Robert Schneider for allowing me to work on this exciting project, for all the guidance and the enthusiasm. I would also like to thank Stephan Herzig and Sebastian Bultmann for being great TAC meeting members and for the fruitful discussions and inspiration. I would like to thank everyone in the Schneider and Bartke lab. Thanks to Adam Kebede for getting this project started. Thanks to Ben Foster for introducing me to the whole *in vitro* histone world. Thanks to Anna Nieborak for her constant help and inspiration. Thanks to Lara Zorro Shahidian for being the best benchie. Thanks to Jessica Pellegrino for protecting the bay and for all the culinary treats. Thanks to Igor Kukhtevich for completing the perfect bay. Thanks to Poonam Bheda for being so much more than a postdoc. Thanks to Kevin Brockers, a great lab twin. Thanks to Magdalena Valenta for being a true friend and having my back. Thanks to Palma Rico Lastres for being so uplifting and undramatic. Thanks to Carlos Mario Genes Robles for being a great IVT buddy. Thanks to Sarah Christine Pereira de Oliveira for her brightness. Thanks to Roberto Olayo Alarcon, María Rocha-Acevedo, Fotios Gkountromichos, and Chris Blum for the light and fun times. Thanks to Rebecca Deutsch for all the hard work and great contribution to the project. Thanks to Andrey Tvardovskiy and Bihter Özdemir Aygenli for their help. Thanks also to the Schmollerians, Kora-Lee Claude, Anika Seel, Dimitra Chatzitheodoridou, and Daniela Bureik for offering a different perspective and for all the fun moments. Thanks to Raian Contreras and Konstantinos Makris for the potential brain dissection and liver supply. Thanks to André Mourao and Arie Geerlof for purified proteins and enzymes but also for stimulating discussions. Thanks to Nadia Prayitno, Anna Kiss, and Peter Becker for trying to solve ChIP and MOF-related problems. Thanks to Tamas Schauer for all the great computational help, effort, and discussions. Thanks to Inti Alberto De La Rosa Velazquez and his sequencing team. Thanks to Natalie Möritz, Jonas Funke, and Hendrik Dietz for teaming up with us and for the coolest *in vitro* tool. Thanks to Harsh Nagpal and Beat Fierz for another cool tool and all the help. Thanks to Joshua Moller, Yiheng Wu, Aria E. Coraor, and Juan de Pablo for stunning *in silico* chromatin simulations. Thanks to Lourdes Ruiz Desviat and Sander Houten for saving our *in vivo* part. Without all of these colleagues, collaborators, and friends this thesis would have not been possible. But an even bigger thank you to family and friends for their support, understanding, and inspiration. Without you, I would not have been able to achieve this or whatever is up next.

9. References

Allis CD, Jenuwein T. The molecular hallmarks of epigenetic control. Nat Rev Genet 2016;17:487–500. https://doi.org/10.1038/nrg.2016.59.

An W, Palhan VB, Karymov MA, Leuba SH, Roeder RG. Selective Requirements for Histone H3 and H4 N Termini in p300-Dependent Transcriptional Activation from Chromatin. Mol Cell 2002;9:811–21. https://doi.org/10.1016/S1097-2765(02)00497-5.

An W, Palhan VB, Karymov MA, Leuba SH, Roeder RG. Selective Requirements for Histone H3 and H4 N Termini in p300-Dependent Transcriptional Activation from Chromatin. Mol Cell 2002;9:811–21. https://doi.org/10.1016/S1097-2765(02)00497-5.

Andrews FH, Shinsky SA, Shanle EK, Bridgers JB, Gest A, Tsun IK, et al. The Taf14 YEATS domain is a reader of histone crotonylation. Nat Chem Biol 2016;12:396–8. https://doi.org/10.1038/nchembio.2065.

Bannister AJ, Kouzarides T. Regulation of chromatin by histone modifications. Cell Res 2011;21:381–95. https://doi.org/10.1038/cr.2011.22.

Bao X, Liu Z, Zhang W, Gladysz K, Fung YME, Tian G, et al. Glutarylation of Histone H4 Lysine 91 Regulates Chromatin Dynamics. Mol Cell 2019;76:660-675.e9. https://doi.org/10.1016/j.molcel.2019.08.018.

Barnes CE, English DM, Cowley SM. Acetylation and Co: An expanding repertoire of histone acylations regulates chromatin and transcription. Essays Biochem 2019;63:97–107. https://doi.org/10.1042/EBC20180061.

Bhala A, Willi SM, Rinaldo P, Bennett MJ, Schmidt-Sommerfeld E, Hale DE. Clinical and biochemical characterization of short-chain acyl-coenzyme A dehydrogenase deficiency. J Pediatr 1995;126:910–5. https://doi.org/10.1016/S0022-3476(95)70207-5.

Bhattacharya A, Chatterjee S, Bhaduri U, Singh AK, Vasudevan M, Sashidhara K V, et al. EP300 (p300) mediated histone butyrylation is critical for adipogenesis. BioRxiv 2021:2021.08.01.454641. https://doi.org/10.1101/2021.08.01.454641.

Boon R, Silveira GG, Mostoslavsky R. Nuclear metabolism and the regulation of the epigenome. Nat Metab 2020;2:1190–203. https://doi.org/10.1038/s42255-020-00285-4.

Boukouris AE, Zervopoulos SD, Michelakis ED. Metabolic Enzymes Moonlighting in the Nucleus: Metabolic Regulation of Gene Transcription. Trends Biochem Sci 2016;41:712–30. https://doi.org/10.1016/j.tibs.2016.05.013.

Brown K, Xie S, Qiu X, Mohrin M, Shin J, Liu Y, et al. SIRT3 Reverses Aging-Associated Degeneration. Cell Rep 2013;3:319–27. https://doi.org/10.1016/j.celrep.2013.01.005.

Carrer A, Parris JLD, Trefely S, Henry RA, Montgomery DC, Torres A, et al. Impact of a High-fat Diet on Tissue Acyl-CoA and Histone Acetylation Levels. J Biol Chem 2017;292:3312–22. https://doi.org/10.1074/jbc.M116.750620.

Carrer A, Parris JLD, Trefely S, Henry RA, Montgomery DC, Torres A, et al. Impact of a High-fat Diet on Tissue Acyl-CoA and Histone Acetylation Levels. J Biol Chem 2017;292:3312–22. https://doi.org/10.1074/jbc.M116.750620.

Chen P, Guo Z, Chen C, Tian S, Bai X, Zhai G, et al. Identification of dual histone modification-binding protein interaction by combining mass spectrometry and isothermal titration calorimetric analysis. J Adv Res 2020;22:35–46. https://doi.org/10.1016/j.jare.2019.11.003.

Chen Q, Yang R, Korolev N, Liu CF, Nordenskiöld L. Regulation of Nucleosome Stacking and Chromatin Compaction by the Histone H4 N-Terminal Tail–H2A Acidic Patch Interaction. J Mol Biol 2017;429:2075–92. https://doi.org/10.1016/j.jmb.2017.03.016.

Chen Q, Yang R, Korolev N, Liu CF, Nordenskiöld L. Regulation of Nucleosome Stacking and Chromatin Compaction by the Histone H4 N-Terminal Tail–H2A Acidic Patch Interaction. J Mol Biol 2017;429:2075–92. https://doi.org/10.1016/j.jmb.2017.03.016.

Chen Y, Sprung R, Tang Y, Ball H, Sangras B, Kim SC, et al. Lysine propionylation and butyrylation are novel post-translational modifications in histones. Mol Cell Proteomics 2007;6:812–9. https://doi.org/10.1074/mcp.M700021-MCP200.

Chypre M, Zaidi N, Smans K. ATP-citrate lyase: A mini-review. Biochem Biophys Res Commun 2012;422:1–4. https://doi.org/10.1016/j.bbrc.2012.04.144.

Collepardo-Guevara R, Portella G, Vendruscolo M, Frenkel D, Schlick T, Orozco M. Chromatin Unfolding by Epigenetic Modifications Explained by Dramatic Impairment of Internucleosome Interactions: A Multiscale Computational Study. J Am Chem Soc 2015;137:10205–15. https://doi.org/10.1021/jacs.5b04086.

Crown SB, Marze N, Antoniewicz MR. Catabolism of Branched Chain Amino Acids Contributes Significantly to Synthesis of Odd-Chain and Even-Chain Fatty Acids in 3T3-L1 Adipocytes. PLoS One 2015;10:e0145850. https://doi.org/10.1371/journal.pone.0145850.

Dai L, Peng C, Montellier E, Lu Z, Chen Y, Ishii H, et al. Lysine 2-hydroxyisobutyrylation is a widely distributed active histone mark. Nat Chem Biol 2014;10:365–70. https://doi.org/10.1038/nchembio.1497.

Dai Z, Ramesh V, Locasale JW. The evolving metabolic landscape of chromatin biology and epigenetics. Nat Rev Genet 2020;21:737–53. https://doi.org/10.1038/s41576-020-0270-8.

Deans C, Maggert KA. What Do You Mean, "Epigenetic"? Genetics 2015;199:887–96. https://doi.org/10.1534/genetics.114.173492.

Dignam JD, Martin PL, Shastry BS, Roeder RG. [36] Eukaryotic gene transcription with purified components, 1983, p. 582–98. https://doi.org/10.1016/0076-6879(83)01039-3.

Dorigo B, Schalch T, Bystricky K, Richmond TJ. Chromatin Fiber Folding: Requirement for the Histone H4 N-terminal Tail. J Mol Biol 2003;327:85–96. https://doi.org/10.1016/S0022-2836(03)00025-1.

Erdel F, Rippe K. Formation of Chromatin Subcompartments by Phase Separation. Biophys J 2018;114:2262–70. https://doi.org/10.1016/j.bpj.2018.03.011.

Fierz B, Poirier MG. Biophysics of Chromatin Dynamics. Annu Rev Biophys 2019;48:321–45. https://doi.org/10.1146/annurev-biophys-070317-032847.

Filipowicz HR, Ernst SL, Ashurst CL, Pasquali M, Longo N. Metabolic changes associated with hyperammonemia in patients with propionic acidemia. Mol Genet Metab 2006;88:123–30. https://doi.org/10.1016/j.ymgme.2005.11.016.

Filippakopoulos P, Knapp S. The bromodomain interaction module. FEBS Lett 2012;586:2692–704. https://doi.org/10.1016/j.febslet.2012.04.045.

Filippakopoulos P, Picaud S, Mangos M, Keates T, Lambert J-P, Barsyte-Lovejoy D, et al. Histone Recognition and Large-Scale Structural Analysis of the Human Bromodomain Family. Cell 2012;149:214–31. https://doi.org/10.1016/j.cell.2012.02.013.

Florian MC, Dörr K, Niebel A, Daria D, Schrezenmeier H, Rojewski M, et al. Cdc42 Activity Regulates Hematopoietic Stem Cell Aging and Rejuvenation. Cell Stem Cell 2012;10:520–30. https://doi.org/10.1016/j.stem.2012.04.007.

Florian MC, Dörr K, Niebel A, Daria D, Schrezenmeier H, Rojewski M, et al. Cdc42 Activity Regulates Hematopoietic Stem Cell Aging and Rejuvenation. Cell Stem Cell 2012;10:520–30. https://doi.org/10.1016/j.stem.2012.04.007.

Flynn EM, Huang OW, Poy F, Oppikofer M, Bellon SF, Tang Y, et al. A Subset of Human Bromodomains Recognizes Butyryllysine and Crotonyllysine Histone Peptide Modifications. Structure 2015;23:1801–14. https://doi.org/10.1016/j.str.2015.08.004.

Funke JJ, Ketterer P, Lieleg C, Schunter S, Korber P, Dietz H. Uncovering the forces between nucleosomes using DNA origami. Sci Adv 2016;2:e1600974. https://doi.org/10.1126/sciadv.1600974.

Gao T, Díaz-Hirashi Z, Verdeguer F. Metabolic Signaling into Chromatin Modifications in the Regulation of Gene Expression. Int J Mol Sci 2018;19:4108. https://doi.org/10.3390/ijms19124108.

Gelbart ME, Larschan E, Peng S, Park PJ, Kuroda MI. Drosophila MSL complex globally acetylates H4K16 on the male X chromosome for dosage compensation. Nat Struct Mol Biol 2009;16:825–32. https://doi.org/10.1038/nsmb.1644.

Gibney ER, Nolan CM. Epigenetics and gene expression. Heredity (Edinb) 2010;105:4–13. https://doi.org/10.1038/hdy.2010.54.

Glozak MA, Sengupta N, Zhang X, Seto E. Acetylation and deacetylation of non-histone proteins. Gene 2005;363:15–23. https://doi.org/10.1016/j.gene.2005.09.010.

Goetzman ES. Modeling Disorders of Fatty Acid Metabolism in the Mouse, 2011, p. 389–417. https://doi.org/10.1016/B978-0-12-384878-9.00010-8.

Goudarzi A, Zhang D, Huang H, Barral S, Kwon OK, Qi S, et al. Dynamic Competing Histone H4 K5K8 Acetylation and Butyrylation Are Hallmarks of Highly Active Gene Promoters. Mol Cell 2016;62:169–80. https://doi.org/10.1016/j.molcel.2016.03.014.

Grigoryan A, Guidi N, Senger K, Liehr T, Soller K, Marka G, et al. LaminA/C regulates epigenetic and chromatin architecture changes upon aging of hematopoietic stem cells. Genome Biol 2018;19:189. https://doi.org/10.1186/s13059-018-1557-3.

Guenzel AJ, Hofherr SE, Hillestad M, Barry M, Weaver E, Venezia S, et al. Generation of a Hypomorphic Model of Propionic Acidemia Amenable to Gene Therapy Testing. Mol Ther 2013;21:1316–23. https://doi.org/10.1038/mt.2013.68.

Guenzel AJ, Collard R, Kraus JP, Matern D, Barry MA. Long-Term Sex-Biased Correction of Circulating Propionic Acidemia Disease Markers by Adeno-Associated Virus Vectors. Hum Gene Ther 2015;26:153–60. https://doi.org/10.1089/hum.2014.126.

Gurdon JB. The Developmental Capacity of Nuclei taken from Intestinal Epithelium Cells of Feeding Tadpoles. Development 1962;10:622–40. https://doi.org/10.1242/dev.10.4.622.

Haberland M, Montgomery RL, Olson EN. The many roles of histone deacetylases in development and physiology: implications for disease and therapy. Nat Rev Genet 2009;10:32–42. https://doi.org/10.1038/nrg2485.

Häberle J, Chakrapani A, Ah Mew N, Longo N. Hyperammonaemia in classic organic acidaemias: a review of the literature and two case histories. Orphanet J Rare Dis 2018;13:219. https://doi.org/10.1186/s13023-018-0963-7.

Han A, Bennett N, MacDonald A, Johnstone M, Whelan J, Donohoe DR. Cellular Metabolism and Dose Reveal Carnitine-Dependent and -Independent Mechanisms of Butyrate Oxidation in Colorectal Cancer Cells. J Cell Physiol 2016;231:1804–13. https://doi.org/10.1002/jcp.25287.

Han Z, Wu H, Kim S, Yang X, Li Q, Huang H, et al. Revealing the protein propionylation activity of the histone acetyltransferase MOF (males absent on the first). J Biol Chem 2018;293:3410–20. https://doi.org/10.1074/jbc.RA117.000529.

Haring M, Offermann S, Danker T, Horst I, Peterhansel C, Stam M. Chromatin immunoprecipitation: optimization, quantitative analysis and data normalization. Plant Methods 2007;3:11. https://doi.org/10.1186/1746-4811-3-11.

Haws SA, Leech CM, Denu JM. Metabolism and the Epigenome: A Dynamic Relationship. Trends Biochem Sci 2020;45:731–47. https://doi.org/10.1016/j.tibs.2020.04.002.

He C, Bonasio R. A cut above. Elife 2017;6. https://doi.org/10.7554/eLife.25000.

Hilfiker A, Hilfiker-Kleiner D, Pannuti A, Lucchesi JC. mof, a putative acetyl transferase gene related to the Tip60 and MOZ human genes and to the SAS genes of yeast, is required for dosage compensation in Drosophila. EMBO J 1997;16:2054–60. https://doi.org/10.1093/emboj/16.8.2054.

Hirschey MD, Shimazu T, Capra JA, Pollard KS, Verdin E. SIRT1 and SIRT3 Deacetylate Homologous Substrates: AceCS1,2 and HMGCS1,2. Aging (Albany NY) 2011;3:635–42. https://doi.org/10.18632/aging.100339.

Hodawadekar SC, Marmorstein R. Chemistry of acetyl transfer by histone modifying enzymes: structure, mechanism and implications for effector design. Oncogene 2007;26:5528–40. https://doi.org/10.1038/sj.onc.1210619.

Horikoshi N, Kumar P, Sharma GG, Chen M, Hunt CR, Westover K, et al. Genome-wide distribution of histone H4 Lysine 16 acetylation sites and their relationship to gene expression. Genome Integr 2013;4:3. https://doi.org/10.1186/2041-9414-4-3.

Houston R, Sekine S, Calderon MJ, Seifuddin F, Wang G, Kawagishi H, et al. Acetylation-mediated remodeling of the nucleolus regulates cellular acetyl-CoA responses. PLOS Biol 2020;18:e3000981. https://doi.org/10.1371/journal.pbio.3000981.

Huang H, Tang S, Ji M, Tang Z, Shimada M, Liu X, et al. p300-Mediated Lysine 2-Hydroxyisobutyrylation Regulates Glycolysis. Mol Cell 2018;70:663-678.e6. https://doi.org/10.1016/j.molcel.2018.04.011.

Huang H, Zhang D, Wang Y, Perez-Neut M, Han Z, Zheng YG, et al. Lysine benzoylation is a histone mark regulated by SIRT2. Nat Commun 2018;9:3374. https://doi.org/10.1038/s41467-018-05567-w.

Iwahara T, Bonasio R, Narendra V, Reinberg D. SIRT3 Functions in the Nucleus in the Control of Stress-Related Gene Expression. Mol Cell Biol 2012;32:5022–34. https://doi.org/10.1128/MCB.00822-12.

Izzo A, Kamieniarz K, Schneider R. The histone H1 family: specific members, specific functions? Biol Chem 2008;389:333–43. https://doi.org/10.1515/BC.2008.037.

Jakobsdottir G, Xu J, Molin G, Ahrné S, Nyman M. High-Fat Diet Reduces the Formation of Butyrate, but Increases Succinate, Inflammation, Liver Fat and Cholesterol in Rats, while Dietary Fibre Counteracts These Effects. PLoS One 2013;8:e80476. https://doi.org/10.1371/journal.pone.0080476.

Jenuwein T, Allis CD. Translating the Histone Code. Science (80-) 2001;293:1074–80. https://doi.org/10.1126/science.1063127.

Jethva R, Bennett MJ, Vockley J. Short-chain acyl-coenzyme A dehydrogenase deficiency. Mol Genet Metab 2008;95:195–200. https://doi.org/10.1016/j.ymgme.2008.09.007.

Jing Y, Ding D, Tian G, Kwan KCJ, Liu Z, Ishibashi T, et al. Semisynthesis of site-specifically succinylated histone reveals that succinylation regulates nucleosome unwrapping rate and DNA accessibility. Nucleic Acids Res 2020;48:9538–49. https://doi.org/10.1093/nar/gkaa663.

Jo C, Park S, Oh S, Choi J, Kim E-K, Youn H-D, et al. Histone acylation marks respond to metabolic perturbations and enable cellular adaptation. Exp Mol Med 2020;52:2005–19. https://doi.org/10.1038/s12276-020-00539-x.

Kaczmarska Z, Ortega E, Goudarzi A, Huang H, Kim S, Márquez JA, et al. Structure of p300 in complex with acyl-CoA variants. Nat Chem Biol 2017;13:21–9. https://doi.org/10.1038/nchembio.2217.

Kafkia E, Andres-Pons A, Ganter K, Seiler M, Jouhten P, Pereira F, et al. Operation of a TCA cycle subnetwork in the mammalian nucleus. BioRxiv 2020:2020.11.22.393413. https://doi.org/10.1101/2020.11.22.393413.

Kalashnikova AA, Porter-Goff ME, Muthurajan UM, Luger K, Hansen JC. The role of the nucleosome acidic patch in modulating higher order chromatin structure. J R Soc Interface 2013;10:20121022. https://doi.org/10.1098/rsif.2012.1022.

Karmodiya K, Krebs AR, Oulad-Abdelghani M, Kimura H, Tora L. H3K9 and H3K14 acetylation co-occur at many gene regulatory elements, while H3K14ac marks a subset of inactive inducible promoters in mouse embryonic stem cells. BMC Genomics 2012;13:424. https://doi.org/10.1186/1471-2164-13-424.

Kebede AF, Nieborak A, Shahidian LZ, Le Gras S, Richter F, Gómez DA, et al. Histone propionylation is a mark of active chromatin. Nat Struct Mol Biol 2017;24:1048–56. https://doi.org/10.1038/nsmb.3490.

Kilic S, Felekyan S, Doroshenko O, Boichenko I, Dimura M, Vardanyan H, et al. Single-molecule FRET reveals multiscale chromatin dynamics modulated by HP1α. Nat Commun 2018;9:235. https://doi.org/10.1038/s41467-017-02619-5.

Klaus VS, Schriever SC, Monroy Kuhn JM, Peter A, Irmler M, Tokarz J, et al. Correlation guided Network Integration (CoNI) reveals novel genes affecting hepatic metabolism. Mol Metab 2021;53:101295. https://doi.org/10.1016/j.molmet.2021.101295.

Klinker H, Mueller-Planitz F, Yang R, Forné I, Liu C-F, Nordenskiöld L, et al. ISWI Remodelling of Physiological Chromatin Fibres Acetylated at Lysine 16 of Histone H4. PLoS One 2014;9:e88411. https://doi.org/10.1371/journal.pone.0088411.

Kouzarides T. Histone methylation in transcriptional control. Curr Opin Genet Dev 2002;12:198–209. https://doi.org/10.1016/S0959-437X(02)00287-3.

Kuo M-H, Allis CD. Roles of histone acetyltransferases and deacetylases in gene regulation. BioEssays 1998;20:615–26. https://doi.org/10.1002/(SICI)1521-1878(199808)20:8<615::AID-BIES4>3.0.CO;2-H.

Lagerwaard B, Pougovkina O, Bekebrede AF, Brinke H, Wanders RJA, Nieuwenhuizen AG, et al. Increased protein propionylation contributes to mitochondrial dysfunction in liver cells and fibroblasts, but not in myotubes. J Inherit Metab Dis 2021;44:438–49. https://doi.org/10.1002/jimd.12296.

Lai M, Chandrasekera PC, Barnard ND. You are what you eat, or are you? The challenges of translating high-fat-fed rodents to human obesity and diabetes. Nutr Diabetes 2014;4:e135–e135. https://doi.org/10.1038/nutd.2014.30.

Leemhuis H, Packman LC, Nightingale KP, Hollfelder F. The Human Histone Acetyltransferase P/CAF is a Promiscuous Histone Propionyltransferase. ChemBioChem 2008;9:499–503. https://doi.org/10.1002/cbic.200700556.

Lequieu J, Córdoba A, Moller J, de Pablo JJ. 1CPN: A coarse-grained multi-scale model of chromatin. J Chem Phys 2019;150:215102. https://doi.org/10.1063/1.5092976.

Li J, Yu Z, Wang Q, Li D, Jia B, Zhou Y, et al. Hyperammonia induces specific liver injury through an intrinsic Ca2+-independent apoptosis pathway. BMC Gastroenterol 2014;14:151. https://doi.org/10.1186/1471-230X-14-151.

Li X, Wu L, Corsa CAS, Kunkel S, Dou Y. Two Mammalian MOF Complexes Regulate Transcription Activation by Distinct Mechanisms. Mol Cell 2009;36:290–301. https://doi.org/10.1016/j.molcel.2009.07.031.

Li Y, Wen H, Xi Y, Tanaka K, Wang H, Peng D, et al. AF9 YEATS Domain Links Histone Acetylation to DOT1L-Mediated H3K79 Methylation. Cell 2014;159:558–71. https://doi.org/10.1016/j.cell.2014.09.049.

Liu X, Sadhukhan S, Sun S, Wagner GR, Hirschey MD, Qi L, et al. High-Resolution Metabolomics with Acyl-CoA Profiling Reveals Widespread Remodeling in Response to Diet*. Mol Cell Proteomics 2015;14:1489–500. https://doi.org/10.1074/mcp.M114.044859.

Lombard DB, Zwaans BMM. SIRT3: As Simple As It Seems? Gerontology 2014;60:56–64. https://doi.org/10.1159/000354382.

Lu Y, Fan C, Li P, Lu Y, Chang X, Qi K. Short Chain Fatty Acids Prevent High-fat-diet-induced Obesity in Mice by Regulating G Protein-coupled Receptors and Gut Microbiota. Sci Rep 2016;6:37589. https://doi.org/10.1038/srep37589.

Luger K, Mäder AW, Richmond RK, Sargent DF, Richmond TJ. Crystal structure of the nucleosome core particle at 2.8 Å resolution. Nature 1997;389:251–60. https://doi.org/10.1038/38444.

Luger K, Rechsteiner TJ, Richmond TJ. Preparation of nucleosome core particle from recombinant histones, 1999, p. 3–19. https://doi.org/10.1016/S0076-6879(99)04003-3.

Madiraju P, Pande S V., Prentki M, Madiraju SRM. Mitochondrial acetylcarnitine provides acetyl groups for nuclear histone acetylation. Epigenetics 2009;4:399–403. https://doi.org/10.4161/epi.4.6.9767.

Maile TM, Izrael-Tomasevic A, Cheung T, Guler GD, Tindell C, Masselot A, et al. Mass Spectrometric Quantification of Histone Post-translational Modifications by a Hybrid Chemical Labeling Method. Mol Cell Proteomics 2015;14:1148–58. https://doi.org/10.1074/mcp.O114.046573.

Martinez-Redondo P, Vaquero A. The Diversity of Histone Versus Nonhistone Sirtuin Substrates. Genes Cancer 2013;4:148–63. https://doi.org/10.1177/1947601913483767.

McGhee JD, Felsenfeld G. Nucleosome Structure. Annu Rev Biochem 1980;49:1115–56. https://doi.org/10.1146/annurev.bi.49.070180.005343.

Mejia-Ramirez E, Florian MC. Understanding intrinsic hematopoietic stem cell aging. Haematologica 2020;105:22–37. https://doi.org/10.3324/haematol.2018.211342.

Mendjan S, Taipale M, Kind J, Holz H, Gebhardt P, Schelder M, et al. Nuclear Pore Components Are Involved in the Transcriptional Regulation of Dosage Compensation in Drosophila. Mol Cell 2006;21:811–23. https://doi.org/10.1016/j.molcel.2006.02.007.

Mikhail FM. Chromosomal Basis of Inheritance. Emery Rimoin's Princ. Pract. Med. Genet. Genomics, Elsevier; 2019, p. 237–65. https://doi.org/10.1016/B978-0-12-812537-3.00009-3.

Monod J, Jacob F. General Conclusions: Teleonomic Mechanisms in Cellular Metabolism, Growth, and Differentiation. Cold Spring Harb Symp Quant Biol 1961;26:389–401. https://doi.org/10.1101/SQB.1961.026.01.048.

Morrison EA, Sanchez JC, Ronan JL, Farrell DP, Varzavand K, Johnson JK, et al. DNA binding drives the association of BRG1/hBRM bromodomains with nucleosomes. Nat Commun 2017;8:16080. https://doi.org/10.1038/ncomms16080.

Mulligan P, Yang F, Di Stefano L, Ji J-Y, Ouyang J, Nishikawa JL, et al. A SIRT1-LSD1 Corepressor Complex Regulates Notch Target Gene Expression and Development. Mol Cell 2011;42:689–99. https://doi.org/10.1016/j.molcel.2011.04.020.

Natsume T, Kiyomitsu T, Saga Y, Kanemaki MT. Rapid Protein Depletion in Human Cells by Auxin-Inducible Degron Tagging with Short Homology Donors. Cell Rep 2016;15:210–8. https://doi.org/10.1016/j.celrep.2016.03.001.

Neumann H, Peak-Chew SY, Chin JW. Genetically encoding Nε-acetyllysine in recombinant proteins. Nat Chem Biol 2008;4:232–4. https://doi.org/10.1038/nchembio.73.

Nie L, Shuai L, Zhu M, Liu P, Xie Z-F, Jiang S, et al. The Landscape of Histone Modifications in a High-Fat Diet-Induced Obese (DIO) Mouse Model. Mol Cell Proteomics 2017;16:1324–34. https://doi.org/10.1074/mcp.M117.067553.

Nieborak A, Schneider R. Metabolic intermediates – Cellular messengers talking to chromatin modifiers. Mol Metab 2018;14:39–52. https://doi.org/10.1016/j.molmet.2018.01.007.

Nishimura K, Fukagawa T, Takisawa H, Kakimoto T, Kanemaki M. An auxin-based degron system for the rapid depletion of proteins in nonplant cells. Nat Methods 2009;6:917–22. https://doi.org/10.1038/nmeth.1401.

Nitsch S, Zorro Shahidian L, Schneider R. Histone acylations and chromatin dynamics: concepts, challenges, and links to metabolism. EMBO Rep 2021;22. https://doi.org/10.15252/embr.202152774.

Nizon M, Ottolenghi C, Valayannopoulos V, Arnoux J-B, Barbier V, Habarou F, et al. Long-term neurological outcome of a cohort of 80 patients with classical organic acidurias. Orphanet J Rare Dis 2013;8:148. https://doi.org/10.1186/1750-1172-8-148.

Oki M, Aihara H, Ito T. Role Of Histone Phosphorylation In Chromatin Dynamics And Its Implications in Diseases. Chromatin Dis., Dordrecht: Springer Netherlands; 2007, p. 323–40. https://doi.org/10.1007/1-4020-5466-1_14.

Olins DE, Olins AL. Chromatin history: our view from the bridge. Nat Rev Mol Cell Biol 2003;4:809–14. https://doi.org/10.1038/nrm1225.

Palladino AA, Chen J, Kallish S, Stanley CA, Bennett MJ. Measurement of tissue acyl-CoAs using flow-injection tandem mass spectrometry: acyl-CoA profiles in short-chain fatty acid oxidation defects. Mol Genet Metab 2012;107:679–83. https://doi.org/10.1016/j.ymgme.2012.10.007.

Parada Venegas D, De la Fuente MK, Landskron G, González MJ, Quera R, Dijkstra G, et al. Short Chain Fatty Acids (SCFAs)-Mediated Gut Epithelial and Immune Regulation and Its Relevance for Inflammatory Bowel Diseases. Front Immunol 2019;10. https://doi.org/10.3389/fimmu.2019.00277.

Paradowska AS, Miller D, Spiess A-N, Vieweg M, Cerna M, Dvorakova-Hortova K, et al. Genome wide identification of promoter binding sites for H4K12ac in human sperm and its relevance for early embryonic development. Epigenetics 2012;7:1057–70. https://doi.org/10.4161/epi.21556.

Park S-Y, Kim J-S. A short guide to histone deacetylases including recent progress on class II enzymes. Exp Mol Med 2020;52:204–12. https://doi.org/10.1038/s12276-020-0382-4.

Parthun MR. Hat1: the emerging cellular roles of a type B histone acetyltransferase. Oncogene 2007;26:5319–28. https://doi.org/10.1038/sj.onc.1210602.

Peterson CL. Purification of Recombinant Drosophila ACF. Cold Spring Harb Protoc 2009;2009:pdb.prot5115-pdb.prot5115. https://doi.org/10.1101/pdb.prot5115.

Pietrocola F, Galluzzi L, Bravo-San Pedro JM, Madeo F, Kroemer G. Acetyl Coenzyme A: A Central Metabolite and Second Messenger. Cell Metab 2015;21:805–21. https://doi.org/10.1016/j.cmet.2015.05.014.

Pitsavos C, Panagiotakos D, Weinem M, Stefanadis C. Diet, Exercise and the Metabolic Syndrome. Rev Diabet Stud 2006;3:118–118. https://doi.org/10.1900/RDS.2006.3.118.

Pougovkina O, te Brinke H, Wanders RJA, Houten SM, de Boer VCJ. Aberrant protein acylation is a common observation in inborn errors of acyl-CoA metabolism. J Inherit Metab Dis 2014;37:709–14. https://doi.org/10.1007/s10545-014-9684-9.

Radzisheuskaya A, Shliaha P V., Grinev V V., Shlyueva D, Damhofer H, Koche R, et al. Complex-dependent histone acetyltransferase activity of KAT8 determines its role in transcription and cellular homeostasis. Mol Cell 2021;81:1749-1765.e8. https://doi.org/10.1016/j.molcel.2021.02.012.

Rando OJ. Combinatorial complexity in chromatin structure and function: revisiting the histone code. Curr Opin Genet Dev 2012;22:148–55. https://doi.org/10.1016/j.gde.2012.02.013.

Reichardt N, Duncan SH, Young P, Belenguer A, McWilliam Leitch C, Scott KP, et al. Phylogenetic distribution of three pathways for propionate production within the human gut microbiota. ISME J 2014;8:1323–35. https://doi.org/10.1038/ismej.2014.14.

Reszko AE, Kasumov T, Pierce BA, David F, Hoppel CL, Stanley WC, et al. Assessing the Reversibility of the Anaplerotic Reactions of the Propionyl-CoA Pathway in Heart and Liver. J Biol Chem 2003;278:34959–65. https://doi.org/10.1074/jbc.M302013200.

Richard E, Pérez B, Pérez-Cerdá C, Desviat LR. Understanding molecular mechanisms in propionic acidemia and investigated therapeutic strategies. Expert Opin Orphan Drugs 2015;3:1427–38. https://doi.org/10.1517/21678707.2015.1092380.

Ringel AE, Wolberger C. Structural basis for acyl-group discrimination by human Gcn5L2. Acta Crystallogr Sect D Struct Biol 2016;72:841–8. https://doi.org/10.1107/S2059798316007907.

Roth SY, Denu JM, Allis CD. Histone Acetyltransferases. Annu Rev Biochem 2001;70:81–120. https://doi.org/10.1146/annurev.biochem.70.1.81.

Rothbart SB, Dickson BM, Ong MS, Krajewski K, Houliston S, Kireev DB, et al. Multivalent histone engagement by the linked tandem Tudor and PHD domains of UHRF1 is required for the epigenetic inheritance of DNA methylation. Genes Dev 2013;27:1288–98. https://doi.org/10.1101/gad.220467.113.

Ruthenburg AJ, Li H, Milne TA, Dewell S, McGinty RK, Yuen M, et al. Recognition of a Mononucleosomal Histone Modification Pattern by BPTF via Multivalent Interactions. Cell 2011;145:692–706. https://doi.org/10.1016/j.cell.2011.03.053.

Sabari BR, Dall'Agnese A, Young RA. Biomolecular Condensates in the Nucleus. Trends Biochem Sci 2020;45:961–77. https://doi.org/10.1016/j.tibs.2020.06.007.

Sabari BR, Tang Z, Huang H, Yong-Gonzalez V, Molina H, Kong HE, et al. Intracellular Crotonyl-CoA Stimulates Transcription through p300-Catalyzed Histone Crotonylation. Mol Cell 2015;58:203–15. https://doi.org/10.1016/j.molcel.2015.02.029.

Sabari BR, Zhang D, Allis CD, Zhao Y. Metabolic regulation of gene expression through histone acylations. Nat Rev Mol Cell Biol 2017;18:90–101. https://doi.org/10.1038/nrm.2016.140.

Sadava D. No Title 2014. https://www.nature.com/scitable/content/DNA-is-Packed-into-a-Mitotic-Chromosome-3497/.

Scher MB, Vaquero A, Reinberg D. SirT3 is a nuclear NAD+-dependent histone deacetylase that translocates to the mitochondria upon cellular stress. Genes Dev 2007;21:920–8. https://doi.org/10.1101/gad.1527307.

Seto E, Yoshida M. Erasers of Histone Acetylation: The Histone Deacetylase Enzymes. Cold Spring Harb Perspect Biol 2014;6:a018713–a018713. https://doi.org/10.1101/cshperspect.a018713.

Shanle EK, Andrews FH, Meriesh H, McDaniel SL, Dronamraju R, DiFiore J V., et al. Association of Taf14 with acetylated histone H3 directs gene transcription and the DNA

damage response. Genes Dev 2015;29:1795–800. https://doi.org/10.1101/gad.269977.115.

Sharma GG, So S, Gupta A, Kumar R, Cayrou C, Avvakumov N, et al. MOF and Histone H4 Acetylation at Lysine 16 Are Critical for DNA Damage Response and Double-Strand Break Repair. Mol Cell Biol 2010;30:3582–95. https://doi.org/10.1128/MCB.01476-09.

Shi L, Tu BP. Acetyl-CoA and the regulation of metabolism: mechanisms and consequences. Curr Opin Cell Biol 2015;33:125–31. https://doi.org/10.1016/j.ceb.2015.02.003.

Shogren-Knaak M, Ishii H, Sun J-M, Pazin MJ, Davie JR, Peterson CL. Histone H4-K16 Acetylation Controls Chromatin Structure and Protein Interactions. Science (80-) 2006;311:844–7. https://doi.org/10.1126/science.1124000.

Siersbæk M, Varticovski L, Yang S, Baek S, Nielsen R, Mandrup S, et al. High fat diet-induced changes of mouse hepatic transcription and enhancer activity can be reversed by subsequent weight loss. Sci Rep 2017;7:40220. https://doi.org/10.1038/srep40220.

Simithy J, Sidoli S, Yuan ZF, Coradin M, Bhanu N V., Marchione DM, et al. Characterization of histone acylations links chromatin modifications with metabolism. Nat Commun 2017;8. https://doi.org/10.1038/s41467-017-01384-9.

Singh M, Popowicz GM, Krajewski M, Holak TA. Structural Ramification for Acetyl-Lysine Recognition by the Bromodomain of Human BRG1 Protein, a Central ATPase of the SWI/SNF Remodeling Complex. ChemBioChem 2007;8:1308–16. https://doi.org/10.1002/cbic.200600562.

Sivanand S, Viney I, Wellen KE. Spatiotemporal Control of Acetyl-CoA Metabolism in Chromatin Regulation. Trends Biochem Sci 2018;43:61–74. https://doi.org/10.1016/j.tibs.2017.11.004.

Smestad J, Erber L, Chen Y, Maher LJ. Chromatin Succinylation Correlates with Active Gene Expression and Is Perturbed by Defective TCA Cycle Metabolism. IScience 2018;2:63–75. https://doi.org/10.1016/j.isci.2018.03.012.

Smestad J, McCauley M, Amato M, Xiong Y, Liu J, Sin Y-C, et al. Protein hyperacylation links mitochondrial dysfunction with nuclear organization. BioRxiv 2020:2020.10.23.350892. https://doi.org/10.1101/2020.10.23.350892.

Smith BC, Denu JM. Acetyl-lysine Analog Peptides as Mechanistic Probes of Protein Deacetylases. J Biol Chem 2007;282:37256–65. https://doi.org/10.1074/jbc.M707878200.

Sohlenius-Sternbeck A-K. Determination of the hepatocellularity number for human, dog, rabbit, rat and mouse livers from protein concentration measurements. Toxicol Vitr 2006;20:1582–6. https://doi.org/10.1016/j.tiv.2006.06.003.

Spakman D, King GA, Peterman EJG, Wuite GJL. Constructing arrays of nucleosome positioning sequences using Gibson Assembly for single-molecule studies. Sci Rep 2020;10:9903. https://doi.org/10.1038/s41598-020-66259-4.

Strahl BD, Allis CD. The language of covalent histone modifications. Nature 2000;403:41–5. https://doi.org/10.1038/47412.

Sun X-J, Man N, Tan Y, Nimer SD, Wang L. The Role of Histone Acetyltransferases in Normal and Malignant Hematopoiesis. Front Oncol 2015;5. https://doi.org/10.3389/fonc.2015.00108.

Sutendra G, Kinnaird A, Dromparis P, Paulin R, Stenson TH, Haromy A, et al. A Nuclear Pyruvate Dehydrogenase Complex Is Important for the Generation of Acetyl-CoA and Histone Acetylation. Cell 2014;158:84–97. https://doi.org/10.1016/j.cell.2014.04.046.

Taipale M, Rea S, Richter K, Vilar A, Lichter P, Imhof A, et al. hMOF Histone Acetyltransferase Is Required for Histone H4 Lysine 16 Acetylation in Mammalian

Cells. Mol Cell Biol 2005;25:6798–810. https://doi.org/10.1128/MCB.25.15.6798-6810.2005.

Tan M, Luo H, Lee S, Jin F, Yang JS, Montellier E, et al. Identification of 67 Histone Marks and Histone Lysine Crotonylation as a New Type of Histone Modification. Cell 2011;146:1016–28. https://doi.org/10.1016/j.cell.2011.08.008.

Tanabe K, Liu J, Kato D, Kurumizaka H, Yamatsugu K, Kanai M, et al. LC-MS/MS-based quantitative study of the acyl group- and site-selectivity of human sirtuins to acylated nucleosomes. Sci Rep 2018;8:1–11. https://doi.org/10.1038/s41598-018-21060-2.

Taylor GCA, Eskeland R, Hekimoglu-Balkan B, Pradeepa MM, Bickmore WA. H4K16 acetylation marks active genes and enhancers of embryonic stem cells, but does not alter chromatin compaction. Genome Res 2013;23:2053–65. https://doi.org/10.1101/gr.155028.113.

Thomas T, Dixon MP, Kueh AJ, Voss AK. Mof (MYST1 or KAT8) Is Essential for Progression of Embryonic Development Past the Blastocyst Stage and Required for Normal Chromatin Architecture. Mol Cell Biol 2008;28:5093–105. https://doi.org/10.1128/MCB.02202-07.

Timmermann S, Lehrmann H, Polesskaya A, Harel-Bellan A. Histone acetylation and disease. Cell Mol Life Sci 2001;58:728–36. https://doi.org/10.1007/PL00000896.

Touw CML, Derks TGJ, Bakker BM, Groen AK, Smit GPA, Reijngoud DJ. From genome to phenome—Simple inborn errors of metabolism as complex traits. Biochim Biophys Acta - Mol Basis Dis 2014;1842:2021–9. https://doi.org/10.1016/j.bbadis.2014.05.032.

Trefely S, Lovell CD, Snyder NW, Wellen KE. Compartmentalised acyl-CoA metabolism and roles in chromatin regulation. Mol Metab 2020:1–18. https://doi.org/10.1016/j.molmet.2020.01.005.

Trefely S, Huber K, Liu J, Singh J, Doan M, Lovell CD., et al. Quantitative sub-cellular acyl-CoA analysis reveals distinct nuclear regulation. BioRxiv 2020. https://doi.org/10.1101/2020.07.30.229468.

Tropberger P, Pott S, Keller C, Kamieniarz-Gdula K, Caron M, Richter F, et al. Regulation of Transcription through Acetylation of H3K122 on the Lateral Surface of the Histone Octamer. Cell 2013;152:859–72. https://doi.org/10.1016/j.cell.2013.01.032.

Turner BM, O'Neill LP, Allan IM. Histone H4 acetylation in human cells Frequency of acetylation at different sites defined by immunolabeling with site-specific antibodies. FEBS Lett 1989;253:141–5. https://doi.org/10.1016/0014-5793(89)80947-0.

Ugarte M, Pérez-Cerdá C, Rodríguez-Pombo P, Desviat LR, Pérez B, Richard E, et al. Overview of mutations in the PCCA and PCCB genes causing propionic acidemia. Hum Mutat 1999;14:275–82. https://doi.org/10.1002/(SICI)1098-1004(199910)14:4<275::AID-HUMU1>3.0.CO;2-N.

Urdinguio RG, Lopez V, Bayón GF, Diaz de la Guardia R, Sierra MI, García-Toraño E, et al. Chromatin regulation by Histone H4 acetylation at Lysine 16 during cell death and differentiation in the myeloid compartment. Nucleic Acids Res 2019;47:5016–37. https://doi.org/10.1093/nar/gkz195.

van Maldegem BT, Wanders RJA, Wijburg FA. Clinical aspects of short-chain acyl-CoA dehydrogenase deficiency. J Inherit Metab Dis 2010;33:507–11. https://doi.org/10.1007/s10545-010-9080-z.

Vaquero A, Sternglanz R, Reinberg D. NAD+-dependent deacetylation of H4 lysine 16 by class III HDACs. Oncogene 2007;26:5505–20. https://doi.org/10.1038/sj.onc.1210617.

Vaquero A, Scher MB, Lee DH, Sutton A, Cheng H-L, Alt FW, et al. SirT2 is a histone deacetylase with preference for histone H4 Lys 16 during mitosis. Genes Dev 2006;20:1256–61. https://doi.org/10.1101/gad.1412706.

Vaquero A. The conserved role of sirtuins in chromatin regulation. Int J Dev Biol 2009;53:303–22. https://doi.org/10.1387/ijdb.082675av.

Verdin E, Ott M. 50 years of protein acetylation: from gene regulation to epigenetics, metabolism and beyond. Nat Rev Mol Cell Biol 2015;16:258–64. https://doi.org/10.1038/nrm3931.

Violante S, IJlst L, Ruiter J, Koster J, van Lenthe H, Duran M, et al. Substrate specificity of human carnitine acetyltransferase: Implications for fatty acid and branched-chain amino acid metabolism. Biochim Biophys Acta - Mol Basis Dis 2013;1832:773–9. https://doi.org/10.1016/j.bbadis.2013.02.012.

Vollmuth F, Geyer M. Interaction of Propionylated and Butyrylated Histone H3 Lysine Marks with Brd4 Bromodomains. Angew Chemie Int Ed 2010;49:6768–72. https://doi.org/10.1002/anie.201002724.

Waddington CH. The Epigenotype. Int J Epidemiol 2012;41:10–3. https://doi.org/10.1093/ije/dyr184.

Wanders RJA, Waterham HR, Ferdinandusse S. Metabolic Interplay between Peroxisomes and Other Subcellular Organelles Including Mitochondria and the Endoplasmic Reticulum. Front Cell Dev Biol 2016;3. https://doi.org/10.3389/fcell.2015.00083.

Wellen KE, Hatzivassiliou G, Sachdeva UM, Bui T V., Cross JR, Thompson CB. ATP-Citrate Lyase Links Cellular Metabolism to Histone Acetylation. Science (80-) 2009;324:1076–80. https://doi.org/10.1126/science.1164097.

Wellen KE, Thompson CB. A two-way street: reciprocal regulation of metabolism and signalling. Nat Rev Mol Cell Biol 2012;13:270–6. https://doi.org/10.1038/nrm3305.

Wilkins BJ, Hahn LE, Heitmüller S, Frauendorf H, Valerius O, Braus GH, et al. Genetically Encoding Lysine Modifications on Histone H4. ACS Chem Biol 2015;10:939–44. https://doi.org/10.1021/cb501011v.

Wongkittichote P, Ah Mew N, Chapman KA. Propionyl-CoA carboxylase – A review. Mol Genet Metab 2017;122:145–52. https://doi.org/10.1016/j.ymgme.2017.10.002.

Wu C -t., Morris JR. Genes, Genetics, and Epigenetics: A Correspondence. Science (80-) 2001;293:1103–5. https://doi.org/10.1126/science.293.5532.1103.

Xie Z, Dai J, Dai L, Tan M, Cheng Z, Wu Y, et al. Lysine Succinylation and Lysine Malonylation in Histones. Mol Cell Proteomics 2012;11:100–7. https://doi.org/10.1074/mcp.M111.015875.

Xie Z, Zhang D, Chung D, Tang Z, Huang H, Dai L, et al. Metabolic Regulation of Gene Expression by Histone Lysine β-Hydroxybutyrylation. Mol Cell 2016;62:194–206. https://doi.org/10.1016/j.molcel.2016.03.036.

Xiong X, Panchenko T, Yang S, Zhao S, Yan P, Zhang W, et al. Selective recognition of histone crotonylation by double PHD fingers of MOZ and DPF2. Nat Chem Biol 2016;12:1111–8. https://doi.org/10.1038/nchembio.2218.

Xu P, Mahamid J, Dombrowski M, Baumeister W, Olins AL, Olins DE. Interphase epichromatin: last refuge for the 30-nm chromatin fiber? Chromosoma 2021. https://doi.org/10.1007/s00412-021-00759-8.

Yang Z, He M, Austin J, Pfleger J, Abdellatif M. Histone H3K9 butyrylation is regulated by dietary fat and stress via an Acyl-CoA dehydrogenase short chain-dependent mechanism. Mol Metab 2021;53:101249. https://doi.org/10.1016/j.molmet.2021.101249.

Yoshimura Y, Araki A, Maruta H, Takahashi Y, Yamashita H. Molecular cloning of rat acss3 and characterization of mammalian propionyl-CoA synthetase in the liver mitochondrial matrix. J Biochem 2016:mvw067. https://doi.org/10.1093/jb/mvw067.

Yun M, Wu J, Workman JL, Li B. Readers of histone modifications. Cell Res 2011;21:564–78. https://doi.org/10.1038/cr.2011.42.

Yung PYK, Elsässer SJ. Evolution of epigenetic chromatin states. Curr Opin Chem Biol 2017;41:36–42. https://doi.org/10.1016/j.cbpa.2017.10.001.

Zhang D, Tang Z, Huang H, Zhou G, Cui C, Weng Y, et al. Metabolic regulation of gene expression by histone lactylation. Nature 2019;574:575–80. https://doi.org/10.1038/s41586-019-1678-1.

Zhang L, Liu C, Jiang Q, Yin Y. Butyrate in Energy Metabolism: There Is Still More to Learn. Trends Endocrinol Metab 2021;32:159–69. https://doi.org/10.1016/j.tem.2020.12.003.

Zhang X, Cao R, Niu J, Yang S, Ma H, Zhao S, et al. Molecular basis for hierarchical histone de-β-hydroxybutyrylation by SIRT3. Cell Discov 2019;5:35. https://doi.org/10.1038/s41421-019-0103-0.

Zhang Y. Transcriptional regulation by histone ubiquitination and deubiquitination. Genes Dev 2003;17:2733–40. https://doi.org/10.1101/gad.1156403.

Zhao D, Li Y, Xiong X, Chen Z, Li H. YEATS Domain—A Histone Acylation Reader in Health and Disease. J Mol Biol 2017;429:1994–2002. https://doi.org/10.1016/j.jmb.2017.03.010.

Zhong Q, Kowluru RA. Role of histone acetylation in the development of diabetic retinopathy and the metabolic memory phenomenon. J Cell Biochem 2010;110:1306–13. https://doi.org/10.1002/jcb.22644.

Zhou Y, Grummt I. The PHD Finger/Bromodomain of NoRC Interacts with Acetylated Histone H4K16 and Is Sufficient for rDNA Silencing. Curr Biol 2005;15:1434–8. https://doi.org/10.1016/j.cub.2005.06.057.

Zippo A, Serafini R, Rocchigiani M, Pennacchini S, Krepelova A, Oliviero S. Histone Crosstalk between H3S10ph and H4K16ac Generates a Histone Code that Mediates Transcription Elongation. Cell 2009;138:1122–36. https://doi.org/10.1016/j.cell.2009.07.031.

Zorro Shahidian L, Haas M, Le Gras S, Nitsch S, Mourão A, Geerlof A, et al. Succinylation of H3K122 destabilizes nucleosomes and enhances transcription. EMBO Rep 2021;22. https://doi.org/10.15252/embr.202051009.

10. Appendix

LIST OF FIGURES

Figure 1.1: Hierarchical chromatin structures. 3
Figure 1.2: Nucleosome structure. 5
Figure 1.3: Histone acetylation regulates gene expression via chromatin compaction. 7
Figure 1.4: Lysine acylations on core histones. 9
Figure 1.5: Hydrophobic lysine acylations. 10
Figure 1.6: The unique role of H4K16ac in chromatin dynamics. 12
Figure 1.7: Compartmentalised acetyl-CoA metabolism. 15
Figure 1.8: Metabolic pathways affected in metabolic disorders. 17
Figure 2.1: Interplay between metabolism and epigenetics. 19
Figure 3.1: Site-specifically acylated “designer” chromatin. 20
Figure 3.2: Purification of truncated H4. 21
Figure 3.3: Native chemical ligation of acylated H4K16. 21
Figure 3.4: Purification of refolded histone octamers. 22
Figure 3.5: Preparations for DNA origami-based force spectrometer measurements. 23
Figure 3.6: Nucleosome-nucleosome interaction analysis. 24
Figure 3.7: Preparations for nucleosomal stacking assays. 25
Figure 3.8: Nucleosomal stacking of unmodified 12-mer nucleosomal arrays. 26
Figure 3.9: Nucleosomal stacking of acylated arrays. 26
Figure 3.10: MOF acts as a histone acyltransferase *in cellulo*. 27
Figure 3.11: Peptide-based affinity purification. 28
Figure 3.12: H4K16 acylation interactors. 29
Figure 3.13: Acylation-specific binding of SIRT3. 30
Figure 3.14: Set-up for the IVT approach. 31
Figure 3.15: H4K16 acylations stimulate transcription *in vitro*. 32
Figure 3.16: H4K16 acylation-specific antibody. 34
Figure 3.17: Nuclear distribution of H4K16 acylations. 35
Figure 3.18: H4K16 acylation-specific polarity in HSCs. 36
Figure 3.19: Overview of different ChIP approaches. 37
Figure 3.20: ChIP approach establishment. 38
Figure 3.21: CUT&RUN nucleosomal ladder. 39
Figure 3.22: CUT&RUN sequencing results. 39
Figure 3.23: Native ChIP was performed on mESCs. 40
Figure 3.24: Overview of genomic distribution of histone acylations in mESCs. 40
Figure 3.25: Representative active genomic regions in mESCs. 41
Figure 3.26: Representative inactive genomic regions in mESCs. 41
Figure 3.27: H4K16 acylation distribution in mESCs. 42
Figure 3.28: H4K16 acylation correlates to gene expression in mESCs. 42
Figure 3.29: Acyl-CoA quantification from cell and tissue samples. 43
Figure 3.30: N-ChIP-qPCR on WT mouse livers. 44

Figure 3.31: Genomic distribution of histone acylations in livers from HFD mice. 45
Figure 3.32: Representative gene regions in which Kac changes upon HFD. 45
Figure 3.33: Representative gene regions in which Kbu changes upon HFD. 46
Figure 3.35: Histone acylation changes in metabolic disorders. 48
Figure 3.36: Quantification of histone acylation changes upon PA. 49
Figure 3.37: H4K16pr enrichment in promoter regions upon PA. 50
Figure 3.38: Gene expression changes upon PA. 50
Figure 3.39: Genomic distribution of histone acylations in livers from *Pcca-/-* & WT mice. . 51
Figure 3.40: Increased H4K16pr enrichment upon PA. 52
Figure 3.41: Decreased H4K16pr enrichment upon PA. 52
Figure 3.42: General increased H4K16pr enrichment upon PA. 53
Figure 3.43: Histone acylations correlate with gene expression. 54
Figure 3.44: Histone propionylation correlates with gene expression. 55
Figure 3.45: Peak intensities at genomic features for WT and *Pcca*$^{-/-}$ samples. 56
Figure 3.46: Altered H4K16pr peak intensities at genomic features upon PA. 57